MIXED LAYER DYNAMICS: EXPLORING THE IMPACT OF STORMS IN THE MID ATLANTIC BIGHT

By

CLIFFORD EVAN WATKINS

A dissertation submitted to the

School of Graduate Studies

Rutgers, The State University of New Jersey

in partial fulfillment of the requirements

for the degree of

Doctor of Philosophy

Graduate Program in Oceanography

written under the direction of

Scott Glenn

and approved by

_____

_____

_____

_____

New Brunswick, New Jersey

January, 2021

ABSTRACT OF THE DISSERTATION

Mixed Layer Dynamics: Exploring the Impact of Storms in the Mid Atlantic Bight

By CLIFFORD EVAN WATKINS

Dissertation Director:

Scott Glenn

This dissertation uses a combination of modeling with observations and new analysis techniques to better understand and predict how the ocean surface boundary layer and stratified coastal ocean interact with the winds at the scale of individual tropical cyclones to seasonal behavior. Understanding and predicting the dynamics of the shallow, coastal ocean response to tropical cyclones as well as its feedback on the storm, especially in the mid-latitudes, remains a gap in the field. First by using large eddy simulations, the physical processes of mixing and entrainment for are shown for Hurricane Irene (2011, where surface cooling due to entrainment ahead of the storm's eye center led to the rapid weakening of the storm. We show how momentum is transferred from wind-induced shear to the pycnocline via large aspect-ratio coherent structures, and how the ocean surface boundary layer responds to the rapid rotation of winds during eye passage. This study showed the novel transition between distinct

regimes of mixing from surface-enhanced coherent structures due to the coherent structures to shear across the pycnocline at eye passage. Secondly, we develop a novel model for determining the mixed-layer depth using a combination of high-frequency (HF) radar and model-derived 10-m winds. We show the shelf-wide behavior of the surface mixed layer depth (MLD) in response to both a tropical cyclone and seasonal forcing in the Mid-Atlantic Bight (MAB). By comparing the modeled MLDs to *in situ* observations through the life cycle of Irene, we show that the storm-driven deepening can be quantified using a novel cost function to solve an inverse solution to Pollard and Millard's (1970) slab model of inertial motion. Using this, we map the rapid ahead-of-eye deepening of the mixed layer moving from Southern MAB northward toward New York City ahead of Irene at the leading edge of the wind field that entrained the cooler waters under the seasonal thermocline and consistent with the northward storm track. This method allows for analysis of the spatial structure of the seasonal cycle in MLD, where the transition from highly stratified to a cooler single-layer system moves from north to south in response to the storm-forcing and diminishing solar intensity of Autumn. And thirdly, we use 13 years of an integrated ocean observing system that consists of Teledyne Webb Slocum gliders, a regional-scale HF Radar network, buoys, and NOAA satellites to investigate the evolution of the MAB under the influence of 11 tropical cyclones. By separating the tracks into onshore, coastal, and offshore, we show that ahead-of-eye cooling, which can affect tropical cyclone intensity, is linked with the advection of Cold Pool waters to the surface via upwelling for onshore storms and wind-driven vertical mixing for along shore storms. The results of this study highlight the need for continued combined ocean observing systems and further work on understanding the ocean-atmosphere coupled system for near-coast regions potential feedbacks on storm intensity.

Acknowledgments

Especially in a time when we are separated by the necessity of a global pandemic, it is worth noting how much of a team effort has gone into making this dissertation possible. I would like to thank my advisor Scott Glenn, who has spent innumerable hours on Webex, Zoom, and phone calls to guide me through the science of this thesis and the realities of turning it into a career. I would also like to thank Dan Whitt, my external committee member, who happened to listen to an excited grad student talk about the Pollard-Rhines-Thompson depth during a job interview and ended up helping me find a place in oceanography incorporating both my desires to pursue modeling and mathematics. And even if our project kept turning in ways that we did not expect, he supported me. I'm grateful for the valuable feedback from Travis Miles, who, as thesis committee member, always kept the end goal in sight and made time for me. A thank you also goes to John Wilkin, another thesis committee member, always kept the science on track, clear, and in context with past studies.

I would like to thank past and present members of the Rutgers University Center for Ocean Observing Leadership, formerly the Coastal Ocean Observation Lab. Without the help of many of you, I would not have been able to press on in my thesis: Mike Crowley, Hugh Roarty, Janice McDonnell, Carrie Ferraro, and especially Patty Gillen and Steve Levenson, who kept me company in our little, loud nook in the DMCS building. I would like to give a special thanks to my family, who I got to live near to for the first time in a long time, for always being there for moral support when I needed it the most. And most importantly Nichole for putting up with me.

I also feel grateful to acknowledge support from Rutgers University through the

School of Environmental and Biological Sciences Excellence Fellowship and the Teledyne Webb Research Graduate Fellowship.

Acknowledging of previous publication in this thesis, chapter 2 presents work done with Daniel Whitt and published in the *Journal of Physical Oceanography* by the American Meteorological Society as "Large-Aspect-Ratio Structures in Simulated Ocean Surface Boundary Layer Turbulence under a Hurricane" in the December 2020 issue.

Dedication

For Nichole, Ramona, and Azíz

Table of Contents

List of Tables

List of Figures

Chapter 1
Introduction

The focus of this thesis is the behavior of the surface layer of the ocean in the mid-latitude ocean, specifically the Mid-Atlantic Bight (MAB), a shallow sea on the large continental shelf in the geographic region between Cape Hatteras in the South and the Gulf of Maine or the Nantucket Shoals in the North (Houghton et al. 1982). This region of the ocean, like much of the mid-latitudes, has large variance in temperature due to seasonal changes in incoming solar radiation and the responding weather patterns. Within the MAB, sea surface temperature (SST) cools by an order of 20 °C from a peak in the late Summer to a minimum in late Winter (Mountain 2003a). The defining feature of the seasonal variability is the strong stratification in the Summer, where the warm and relatively fresh mixed layer is separated by a strong pycnocline from cooler remnant, known colloquially as the Cold Pool (Houghton et al. 1982). Along the shallow continental shelf, the mixed layer can deepen to become a well-mixed, single layer interacting with the bottom due to many different physical processes such as Ekman advection interacting with the coastal wall (Austin, Lentz 2002) and direct mixing from wind-shear Dohan, Davis (2011); Shroyer et al. (2014). The coastal ocean can then reform a two-layer system through surface or horizontal fluxes, evolving on timescales ranging from synoptic to seasonal, rendering the observational techniques of the open ocean insufficient to describe the time-dependent behavior (Mountain 2003b).

Mixing and transport, primarily wind-driven, of the mixed layer in the two-layer, Summer MAB mediates the interaction between the ocean and atmosphere during storms (Miles et al. 2013; Seroka et al. 2016). Depending on the direction and strength

of the wind stress, upwelling currents, downwelling currents, and direct entrainment of Cold Pool waters from wind-induced shear can result. These processes can have a large influence on the coastal sea surface temperature (SST) distribution and evolution, and resultant air-sea fluxes, impacting the evolution of atmospheric circulation.

Using large eddy simulations (LES), we analyzed the physical processes of mixing and entrainment under Hurricane Irene (2011), where surface cooling due to entrainment ahead of the storm's eye center led to the rapid weakening of the storm (Glenn et al. 2016). Momentum is transferred from wind shear to the pycnocline via large aspect-ratio coherent structures that have been previously that have been previously studied in the atmospheric boundary layer (Brown 1972; Lemone 1973; Etling, Brown 1993) but have only recently been applied to the oceanic boundary layer in the open ocean (Duncombe 2017; Skyllingstad et al. 2017b). By using a large horizontal domain, we were able to simulate the evolution of large-aspect-ratio structures and their role in OSBL turbulence under a hurricane in a large-aspect-ratio oceanic domain in which the OSBL depth ranges from 1/200 to 1/55 the horizontal domain length. The large structures modulate the turbulent processes at the heart of mixing the OSBL and entraining the cooler, denser waters underneath the pycnocline. As the eye passes in the LES, the large aspect-ratio structures respond to the rapid rotation of winds during eye passage by decaying and altering the physical mechanisms of momentum transfer. The change in behavior of the OSBL with eye passage developed into a transition between distinct regimes of mixing from a regime dominated by wind-induced shearing at the surface to shear across the pycnocline at eye passage. Chapter 2 was published in the Journal of Physical Oceanography as (Watkins, Whitt 2020b)

Using high-frequency (HF) radar currents and reanalysis winds, we developed an algorithm, Slab Lagged Inertial Model (SLIM), to predict the mixed layer depth using a reworking of the slab model of inertial response to atmospheric forcing as decribed in Pollard, Millard (1970a) and Pollard (1970). By using the HF radar

network operated by the Mid-Atlantic Regional Association Coastal Ocean Observing System (MARACOOS) since 2007 (Roarty et al. 2020), SLIM predicts the behavior of the MLD across a region of broad spatial and temporal extent from remote sensing observations, which offer opportunities for examining the role of MLD variability across the entire MAB and time-scales from synoptic to seasonal.

In chapter 4, we use 13 years of an integrated ocean observing system that consists of Teledyne Webb Slocum gliders, regional-scale HF Radar network, buoys, and NOAA satellites to investigate the evolution of the Mid-Atlantic Bight under the influence of 11 tropical cyclones. By narrowing down the response of the MAB to essential ocean processes, we detail the relation between tropical storm forcing and ocean processes. Wind-induced vertical mixing (Jaimes, Shay 2009) and shear due to near-inertial currents (Shearman 2005a) are the dominant processes for storms that travel along shore and cross the MAB. Additionally, three-dimensional upwelling and downwelling currents, responding to along-shore wind stress, control the SST response for storm both inshore and offshore of the MAB due to the interaction of the coast with Ekman dynamics (Austin, Lentz 2002). Thus, this heuristic approach to the co-evolution of the three-dimensional ocean mixed layer, which influences the air-sea interface and intensity of tropical cyclones, allows for future work at simplifying the predictive framework for a complex, rapidly changing system.

Chapter 2

Large Eddy Simulations under Hurricane Irene (2011)

2.1 Introduction

Observations (e.g., Savelyev et al. 2018b) and simulations (e.g., Hamlington et al. 2014) show that ocean surface boundary layer (OSBL) turbulence sometimes includes a continuum of horizontal length scales characterized by a negative power spectral slope without a peak in variance near the length scale of the OSBL depth. In particular, prominent large-aspect-ratio [1] structures with horizontal scales larger than the OSBL depth coexist with more isotropic structures with scales similar to and smaller than the OSBL depth. Prior work has loosely classified observed large-aspect-ratio structures into a few groups: 1) wind/wave/buoyancy-driven Langmuir circulations that are characterized by horizontally-anisotropic rolls and streaks approximately aligned with the wind vector and perpendicular to surface wave crests (Langmuir 1938; Leibovich 1983; Smith 1992; Thorpe 2004; Kukulka et al. 2009; Sullivan, McWilliams 2010), mostly with cross-roll length scales less than 4 times the OSBL depth but with some notable larger exceptions (Marmorino et al. 2005; Gargett et al. 2004; Gargett, Wells 2007; Qiao et al. 2009; Sundermeyer et al. 2014), 2) internal waves (Elachi, Apel 1976; Wijesekera, Dillon 1991; Shaun-Johnston, Rudnick 2009; Callies, Ferrari 2013), 3) stratified shear instabilities such as the Kelvin-Helmholtz

[1] Unless otherwise specified, we define large-aspect ratio to mean that the characteristic horizontal length scale is larger than the characteristic vertical length scale. Confusingly, many features of interest are also elongated and anisotropic in the horizontal plane. Hence, unless otherwise specified, the characteristic horizontal length scale of a structure refers to the shortest possible characteristic scale that can be derived.

mode (Seim, Gregg 1994; Chang et al. 2016), and 4) submesoscale vortex and frontal dynamics (Munk et al. 2000; McWilliams 2016; Savelyev et al. 2018a; D'Asaro et al. 2018; Marmorino, Chen 2019).

Other boundary layers also contain prominent large-aspect-ratio structures, which exhibit some similarities to their OSBL cousins. For example, numerous observations reveal roll vortices and associated streaks characteristic of shear instabilities in the atmospheric boundary layer (ABL) (Lemone 1973, 1976; Etling, Brown 1993; Young et al. 2002). In addition, laboratory measurements and direct numerical simulations reveal long streaks extending up to 10 times the BL height approximately aligned with the shear in high-Reynolds number wall-bounded flows with and without rotation and/or stratification (Tatro, Mollo-Christensen 1967; Marusic et al. 2010; Smits et al. 2011; Hutchins et al. 2012; Sous et al. 2013; Deusebio et al. 2014).

However, the role of large-aspect-ratio structures in OSBL turbulence and their implications for larger-scale ocean dynamics remains to be fully understood. Here, we build understanding by reporting on a large eddy simulation (LES) that models the rapid turbulent entrainment and sea-surface temperature (SST) cooling observed on the New Jersey shelf during the passage of Hurricane Irene in 2011 (Glenn et al. 2016; Seroka et al. 2016) and contains vigorous large-aspect-ratio structures, which participate with smaller-scale turbulence in driving the entrainment and surface cooling.

Many previous studies have used LES to investigate transient and unsteady OSBL dynamics. LES provides a local perspective on OSBL turbulence that is generated by the surface forcing, dynamical instabilities and non-linear transfers across the resolved scales, without the convoluting effects of lateral advection or propagation from remote locations or local transfers of energy from scales that are unresolved on the grid. However, only a few studies have used LES to study OSBL turbulence including horizontal wavelengths greater than ten times the OSBL depth. Most of these studies have used large-aspect-ratio domains to study the interactions between submesoscale

vortex and frontal dynamics and smaller-scale turbulence (e.g., Skyllingstad, Samelson 2012; Hamlington et al. 2014; Sundermeyer et al. 2014; Taylor 2016; Smith et al. 2016; Whitt, Taylor 2017; Skyllingstad et al. 2017b; Callies, Ferrari 2018; Sullivan, McWilliams 2018, 2019). Comparatively little work has been devoted to investigating the role of such large-aspect-ratio structures in OSBLs forced simply by wind, before considering buoyancy and/or surface gravity wave effects. However, previous LES studies have noted interactions between surface boundary layer turbulence and short internal waves (Polton et al. 2008; Czeschel, Eden 2019). Sullivan et al. (2012) noted that it was necessary to use a 1500 m wide domain (12.5 times the maximum OSBL depth) in order to resolve some spontaneously-generated internal waves under hurricane forcing. Others (Sundermeyer et al. 2014; Skyllingstad et al. 2017b) found large-aspect-ratio Ekman-layer rolls with horizontal scales 5-10 times the OSBL depth in both observations and LES, regardless of whether surface wave effects were included in the LES. Although ABL LES is limited by the similar computational challenges, previous studies have repeatedly simulated large structures approximately aligned with the geostrophic flow in the Ekman ABL (e.g., Moeng, Sullivan 1994; Khanna, Brasseur 1998; Fang, Porté-Agel 2015). Notably, Fang, Porté-Agel (2015) report on LES of the ABL in a horizontal domain that is 100 by 14 times the ABL height, in which they find that streaks with cross-stream length scales comparable to the ABL height but streamwise wavelengths greater than 10 times the BL height contribute about 1/3 of the total turbulent vertical transport. However, it is still not well known how large-aspect-ratio structures contribute to the net fluxes and mean evolution of the OSBL under time-variable wind. But, it seems likely that large structures are important in some circumstances.

The purpose of this chapter is to describe the simulated large-aspect-ratio structures and their role in OSBL turbulence under a hurricane in a large-aspect-ratio oceanic domain in which the OSBL depth ranges from 1/200 to 1/55 the horizontal domain length. The simulation is realistic in that it is initialized with observed

temperature and salinity vertical profiles just before the storm and forced by a time-dependent 3-hourly surface wind stress, heat flux, and penetrative radiative heating derived from atmospheric reanalysis. On the other hand, the simulation is idealized in that all other processes are omitted, including the effects of ocean surface gravity waves and the larger-scale ocean circulation. The expectation is not that these other processes or their interactions with wind- and buoyancy-forced OSBL turbulence are not important. Rather, the expectation is that it is necessary to study these different processes both in isolation and in combination to obtain a full understanding of OSBL dynamics. This paper is a step toward that broader goal. After a description of the model, the results include two parts: the first is a descriptive analysis of the life cycle and characteristics of the simulated large-aspect-ratio structures. The second demonstrates how the evolution of the large-scale structures relates to and impacts the evolution of the mean profiles of momentum and buoyancy via the turbulent vertical fluxes that drive the evolution of the mean profiles.

2.2 Model configuration

2.2.1 Model description and initial conditions

The numerical model is similar to that used in Whitt, Taylor (2017) (and described in more detail by Taylor 2008). Briefly, the evolution of the resolved flow is obtained by time-stepping the rotating Boussinesq equations on a traditional f-plane with Coriolis frequency $f = 9.3 \times 10^{-5}$ s^{-1} using a mixed method, in which the Crank-Nicholson scheme advances the vertical viscous/diffusive terms, a third order Runge-Kutta scheme advances all other terms, and the projection method is used to enforce incompressibility and update the pressure. Spatial derivatives are discretized using a pseudo-spectral approach in the horizontal and second-order central differences in the vertical. The fluid density ρ and buoyancy $b = -g\rho/\rho_0$ depend on both temperature and salinity via a linear equation of state $\rho = \rho_0(1+\alpha(T-T_0)+\beta(S-S_0))$, where $\rho_0 =$

1022.8 kg/m^3, $T_0 = 17.0\ ^oC$, $S_0 = 31.5$ psu, $\alpha = -0.000281\ 1/^oC$, and $\beta = 0.000766$ 1/psu, and $g = 9.81$ m/s^2. Subgrid-scale (SGS) momentum fluxes are obtained using a modified Smagorinski approach (Kaltenbach et al. 1994). The subgrid-scale fluxes of salt and temperature are represented by a down-gradient diffusion, where the diffusivities of heat and salt are equal but vary spatially and temporally with the subgrid-scale viscosity and Prandtl number, that is $\kappa_{SGS} = \nu_{SGS} Pr_{SGS}^{-1}$. As in Whitt, Taylor (2017), $Pr_{SGS}^{-1} = 1/(1 + Ri_{GS}/0.94)^{1.5}$ (Anderson 2009) and the grid-scale gradient Richardson number $Ri_{GS} = \frac{\delta z \delta b}{\delta u^2 + \delta v^2}$, where δ denotes the difference between two vertically-adjacent grid cells.

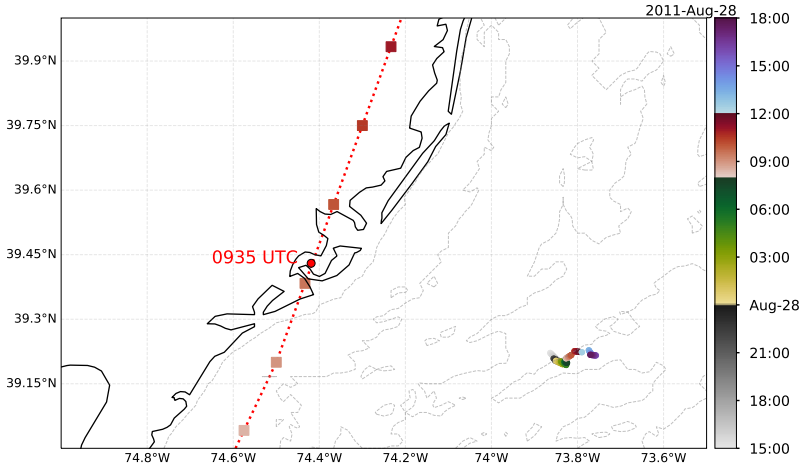

Figure 2.1: The track of a profiling buoyancy glider (small dots) and bathymetry contours (dotted lines). Color indicates the time (UTC), which is separated into four phases: I (black), II (green), III (red), IV (blue) (see Fig. 2.3). The approximate location of the hurricane's eye is indicated by squares, which are spaced every 30 min and are colored to indicate the time, similar to the glider track. The red dot on the hurricane track indicates the time and location of landfall (Glenn et al. 2016).

The numerical solution is obtained in a domain that is a horizontally-periodic box that is 1958 m by 1958 m by 35 m and spanned by a mesh with 2304 by 2304 by 85 grid points that are evenly spaced 0.85 by 0.85 by 0.42 m apart. A study of the sensitivity of the LES solutions to the domain size is not pursued here. However, we note that horizontal domains of 245, 122, and 41 m with the same horizontal and vertical grid spacings were also attempted. In the larger two of three domains, the simulations

revealed dominant domain-scale structures and intermittency in the statistics, both of which were deemed undesirable. These issues were somewhat mitigated in the smallest domain, but the statistics in that case are not very robust with so few points.

The time step is varied dynamically so that the Courant number remains sufficiently small and the time stepping scheme remains stable. Due to the strong currents during the storm, the time step drops below 0.15s late in the storm. Hence, the simulation requires about 370,000 time steps to reach the end of phase IV in Fig. 2.3 (a). The depth of the domain is chosen to be approximately the same as the ocean bottom depth roughly 100 km east of Cape May, NJ (about half way from the coast to the shelf break), where glider observations of temperature and salinity profiles were available before and during the storm, where the glider maintained station-keeping operations near 40 m isobath as shown in Fig. 2.1 with surfacing for upload of data every three hours.

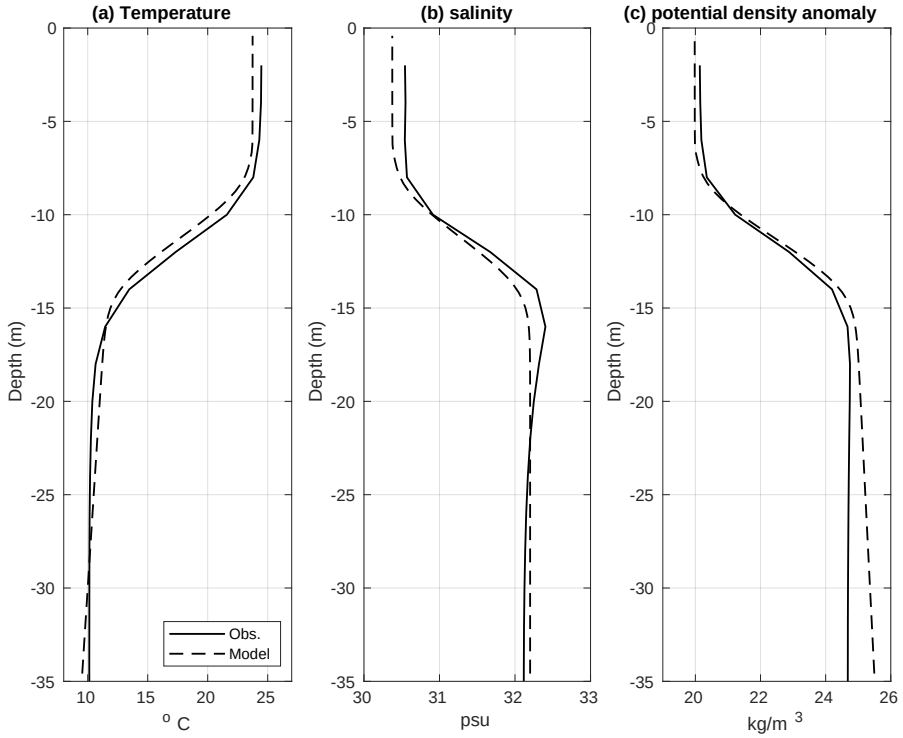

Figure 2.2: A comparison between the modeled and observed temperature, salinity and potential density profiles just before the storm on August 27, 2011 12:00, when the glider was at 39.24 N, 73.88 W.

The velocity field is initialized with a small-amplitude random kick in each grid cell with root-mean-square of order 10^{-4} m/s, and the temperature and salinity are initialized with horizontally-uniform profiles that are defined by analytic functions designed to approximately match observed temperature and salinity profiles obtained by a glider on the New Jersey shelf just before the storm (Fig. 2.2) (for details about the observations, see Glenn et al. 2016). The simulation begins on August 27, 2011 at 00:00 (all times are UTC) and runs through August 29 at 18:00, but the atmospheric forcing is modest until 15:00 on August 27, when our analysis begins (Fig. 2.3).

2.2.2 Atmospheric forcing and boundary conditions

The surface and bottom boundary conditions for vertical velocity are $w = 0$; temperature, salinity and horizontal velocity are horizontally-uniform but time-dependent vertical gradients. At the top, the vertical gradients of horizontal velocity, e.g. $\nu_{SGS}\partial\mathbf{u}/\partial z = \boldsymbol{\tau}/\rho_0$ where $\nu_{SGS} = 10^{-6}$ m^2/s, and temperature are defined by 3-hourly surface wind stress and heat fluxes (excluding penetrating shortwave) derived from a regional ocean model published by Glenn et al. (2016) (Fig. 2.3). That regional ocean model in Glenn et al. (2016) is initialized from a state obtained via data assimilation and forced by the 3-hourly/12-km resolution reanalysis from the North American Mesoscale forecast model, and the surface fluxes are calculated using the COARE algorithm (Fairall et al. 2003). As in the regional ocean model of Glenn et al. (2016), shortwave radiation penetrates and acts as an interior heat source in the LES that follows a modified Jerlov type II two-component exponential profile (Paulson, Simpson 1977) with the first e-folding depth scale $\zeta_1 = 5$ m instead of 1.5 m to avoid a collapse of turbulence near the surface under stabilizing buoyancy forcing and weak wind before the storm. This approach is ad hoc and may need to be reconsidered in future work, but it is plausibly justified based on observations that the top few meters are sometimes more turbulent than expected from the wind stress and buoyancy flux alone due to surface wave effects (e.g., Anis, Moum 1995).

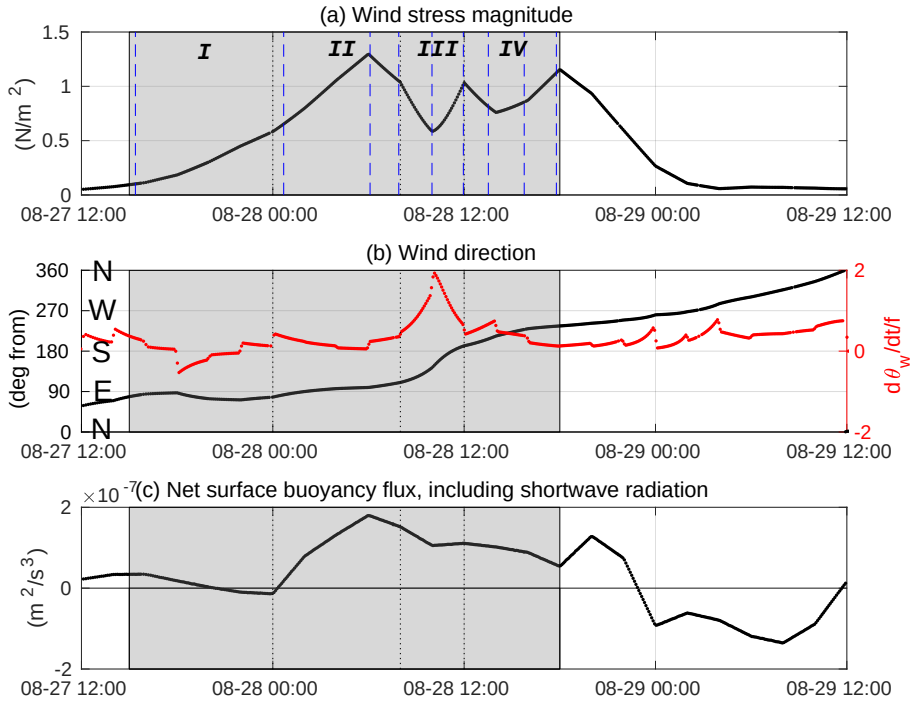

Figure 2.3: Ocean surface fluxes during the storm. The surface stress has magnitude $|\boldsymbol{\tau}|$ (a), direction θ_w (b; left axis), and rate of rotation normalized by the Coriolis frequency $d\theta_w/dt/f$ (b; right axis). The net surface buoyancy flux (c), which is (atypically) injecting buoyancy into the ocean during most of the storm, includes the penetrating shortwave, net longwave, latent and sensible heat fluxes. Surface freshwater/salinity fluxes are set to zero for simplicity. This paper focuses on the grey shaded time period and separates that period into four phases, as described in the text.

To aid in the latter description, we separate the forcing into four phases of interest as shown in Fig. 2.3 (a). In phase I, there is a period of rising but modest ($|\boldsymbol{\tau}| < 0.5$ N/m^2) and consistently easterly wind as the storm approaches from the south along the US east coast. Then, in phase II there is a period of stronger winds from the east ($|\boldsymbol{\tau}| > 0.5$ N/m^2), which is punctuated by the maximum wind stress (1.2 N/m^2) at 06:00 on August 28. Phase III includes the eye passage, when winds are strong but weaker than the maximum ($1 > |\boldsymbol{\tau}| > 0.5$ N/m^2) and the stress vector rotates rapidly. Since the LES domain is situated to the right of the eye track, the wind stress vector rotates clockwise from a westward stress (easterly winds) to a northeastward stress (southwesterly winds) as the eye passes (Fig. 2.3 (b)). Finally, phase IV represents

the period of strong and persistently southwesterly wind after the eye passes. The subsequent periods of decaying winds and low post-storm winds are not considered in this paper.

Atypically, the net heat flux is into the ocean during most of the storm and during almost all of August 28 (Fig. 2.3 (c)). During phases II and III, as the wind ramps up and eventually the eye passes at about 09:00 on August 28, the turbulent heat and buoyancy fluxes and the corresponding vertical temperature gradient at the surface boundary of the LES are positive (injecting heat into the ocean) during nighttime (Fig. 2.3 (b) and (c)). During phase IV and the remainder of August 28 after the eye passage, there are weak turbulent heat losses from the ocean and a negative surface temperature gradient at the top boundary of the LES, but solar radiation makes the net heat flux positive until nearly nightfall at roughly 00:00 on 08-29. This unusual situation, in which the turbulent surface latent and sensible heat fluxes are into the ocean, is thought to have been caused by the rapid entrainment-driven ahead-of-eye cooling of the SST, which contributed to the observed rapid decay of the hurricane during this period (Glenn et al. 2016; Seroka et al. 2016).

Before proceeding, consider the relative importance of the surface buoyancy flux $F_b(0)$ (Fig. 2.3 (c)) and momentum flux $\mathbf{F}_m(0) = \boldsymbol{\tau}/\rho_0$ for the OSBL turbulence using Monin-Obukhov similarity theory (e.g., Monin, Obukhov 1954; Businger et al. 1971; Lombardo, Gregg 1989). First, the Monin-Obukhov length $L_{MO} = |\mathbf{F}_m(0)|^{3/2}/k|F_b(0)| >$ 300 m, where $k = 0.4$ is the von Karman constant. And, the boundary layer is only 10-30 m deep. So, the conditions are generally near neutral, that is $|z/L_{MO}| < 0.1$ and the wind-driven turbulence is expected to be only modestly impacted by the stable surface buoyancy flux at all depths and throughout the duration of the analysis (i.e., the shaded gray area in Fig. 2.3).

During the analysis period reported here (the gray shaded area in Fig. 2.3), the bottom layer remains nearly motionless and stratified on average, and the magnitude of the bottom stress never exceeds 10^{-4} N/m^2, so the details of the bottom gradient

conditions and the associated wall model are thought to be unimportant and omitted for brevity although the bottom may still be significant, e.g. due to the trapping of internal wave energy that might otherwise radiate downward in the open ocean.

2.3 Visualization and description

We begin by reporting the results of flow visualizations and describe the dominant large turbulent structures in the OSBL, which we separate from more quiescent water below by the depth of maximum stratification $z = -D_{N^2}$, where the stratification is defined by $\langle N^2 \rangle_{x,y} = \langle \partial b / \partial z \rangle_{x,y}$ (here, $\langle \rangle_{x,y}$ denotes an average over the horizontal dimensions x and y). This section is separated into two parts to facilitate a description of the two types of large structure that are, conveniently, dominant at two distinct depth levels: the first is a discussion of the near-surface layer, and the latter is focused on the base of the OSBL (i.e., just above D_{N^2}).

2.3.1 Near-surface

Plan views of the simulated currents at 5 m depth early on August 28 (the beginning of phase II) reveal striking anisotropic streaks that are elongated in the wind direction (Fig. 2.4). We begin with a chronological description of the life cycle of these structures. Then we describe the spatial structure in more detail using vertical sections of several key variables in a streak-roll coordinate system.

It may be noted that the features are reminiscent of Ekman layer rolls (for stratified linear stability analysis, see Kaylor, Faller (1972); Brown (1972); Asai, Nakasuji (1973); for atmospheric observations, see Lemone (1973, 1976); for recent oceanic perspective, see Sundermeyer et al. (2014); Duncombe (2017); Skyllingstad et al. (2017b)), but comparisons between the associated theory, prior observations, and the structures reported here are deferred to the discussion section.

Chronology

To begin with, it is notable that it takes about 15-24 hours for the streaks shown in Fig. 2.4 to first emerge as dominant features of the turbulence during phase I (which begins 15 hours into the simulation at 15:00 on August 27), either because it takes this long for the wind to reach sufficient strength and/or because the motions take this long to achieve finite amplitude via another dynamic mechanism such as a linear instability. In particular, the power spectrum of kinetic energy as a function of time at 5 m depth and at large-scale wavelengths $\lambda > 3D_{N^2}$ exhibits approximately exponential growth in time $e^{t/\tau}$ with $\tau \sim 10^4$ s. At the same time, the wind stress magnitude and the associated magnitude of the mean wind-driven currents in the OSBL also increase approximately exponentially at about the same rate as the storm approaches. However, the largest of the large scales (~ 1 km) are energized somewhat more slowly than the smaller of the large scales (~ 0.1 km) (not shown; but the netcdf files with the spectra are published in Watkins, Whitt 2020a). As a result, the fraction of the horizontal kinetic energy associated with wavelengths longer than three times $D_{N^2} \approx 10$ m is less than 25% of the total variance before 20:00 on August 27 (Fig. 2.5 (a)). In addition, the maxima in the radially-integrated horizontal wavenumber spectra of both horizontal and vertical kinetic energy are both at about 0.1 cycles per meter at 5 m depth before 15:00 on August 27. Hence, the dominant large turbulent eddies are nearly isotropic with a characteristic scale similar to the OSBL depth during most of August 27.

As the wind strengthens during the first half of August 28 (phase II), variance in both the horizontal currents and buoyancy increases at horizontal wavelengths $\lambda > 3D_{N^2}$ associated with large aspect ratios. In particular, horizontal kinetic energy at wavelengths $\lambda > 3D_{N^2}$ increases to more than half of the total horizontal kinetic energy at 5 m depth (Fig. 2.5 (a)). And, the anomalous current speed in the streaks reaches a maximum characteristic magnitude of about 10 cm/s, which is roughly 10% of the mean speed, which grows from about 0.5 m/s to 1.3 m/s during phase II. At

the same time, the buoyancy variance at wavelengths $\lambda > 3D_{N^2}$ comes to represent more than 75% of the total variance shallower than 5 m depth (Fig. 2.5 (c)). Hence, qualitatively similar streaks are visible in the plan views of temperature at 5 m, like the currents (c.f. Figs. 2.4 (d) and 2.6 (a)), and the characteristic temperature anomalies in the streaks are a few tenths of a degree C. The vertical kinetic energy also increases at wavelengths $\lambda > 3D_{N^2}$ during phase II. However, this large-scale vertical kinetic energy remains about 2-3 orders of magnitude weaker than the corresponding large-scale horizontal kinetic energy, as expected based on the aspect ratio of the flow structures. In addition, this large-scale vertical kinetic energy remains a small fraction of the total vertical kinetic energy, which remains dominated by wavelengths $\lambda < 3D_{N^2}$ typical of more isotropic OSBL turbulence (Fig. 2.5 (b)).

Although the large-aspect-ratio streaks are prominent throughout phase II, when the wind is strong and persistently easterly, the streaks are not static. First, the streaks propagate at speeds comparable to the mean flow $\sim$ 1 m/s, such that their characteristic timescale measured at a fixed position is of order 100 seconds. For example, at the beginning of phase III, the streaks propagate to the northwest in about the same direction as mean surface current, which points at an angle about 45° to the right of the wind (the mean flow will be discussed in later sections). However, in a reference frame following the mean flow in the upper 10 m, the streaks are nearly stationary and evolve with a much longer characteristic timescale more appropriately measured in hours than seconds, consistent with the timescale over which they initially emerge (see Supplemental Videos). Second, the dominant cross-streak wavelength λ_r increases with time during phase II, from approximately 100 to 300 m (Fig. 2.4). Perhaps not coincidentally, the depth D_{N^2} deepens from about 12 m to 20 m at the same time (Fig. 2.5), such that the ratio λ_r/D_{N^2} remains in a narrower range of about $8 - 15$. However, the orientation of the along-streak axis remains fairly consistent during phase II: it is rotated slightly clockwise $\sim 10°$ from the wind vector (Fig. 2.4), which rotates slowly clockwise during phase II. As the wind rotates more

quickly during phase III, the streaks also rotate more quickly clockwise with the wind. However, the amplitude of the current and temperature anomalies associated with the large-aspect-ratio streaks decays in both absolute terms and as a percentage of the total variance. The most obvious factor associated with the washing out of the streaks/rolls is the rate of rotation of the surface wind stress, which exceeds the local Coriolis frequency during eye passage in phase III. Thereafter, the streaks are not dominant features of the flow (Fig. 2.4), although the large-scale variance does increase toward the end of phase IV as the wind rotation slows and the direction stabilizes becoming consistently south-westerly to westerly (Fig. 2.5 a.2), and the spin-up timescale of the streaks in phase IV seems similar to their initial spin-up timescale before the eye passes.

Vertical sections of rolls/streaks in roll coordinates

Vertical sections oriented perpendicular to the streak axis at the end of phase II highlight several key characteristics of the streaks/rolls and their impact on smaller-scale OSBL turbulence. We find that the cross-streak v_r and vertical w_r velocities form tilted rolls (Fig. 2.7) that are associated with the streaks u_r shown at 5 m depth in Fig. 2.4. The amplitude of the streaks/rolls decays rapidly with depth below 10 m, but their orientation in the horizontal plane does not rotate with depth despite substantial rotation of the mean shear vector (see Figs. 2.6 and 2.7). The simulated roll vertical velocity anomalies w_r have a characteristic scale of a few mm/s, and the corresponding cross-streak roll velocities v_r are a few cm/s, that is $v_r \sim 10 w_r$ consistent with the aspect ratio of about 10. The simulated horizontal cross-streak roll velocity v_r is about three times weaker than the streak velocity u_r. Thus, v_r stands out less prominently from other variability and appears less organized than u_r.

In addition, we find systematic correlations between the roll/streak variables, and thus an indication of net vertical transport by the streaks/rolls. In particular,

the simulated streak velocity u_r is negatively correlated with w_r, although they are not perfectly aligned. The phase shift ϕ_r that minimizes the lagged correlation (to about -0.8) between $u_r(y_r)$ and $w_r(y_r + \phi_r)$ occurs at $\phi_r \approx -20$ to -40 m or about $-0.1\lambda_r$. Conversely, temperature anomalies T_r are positively correlated with w_r, but the correlation coefficient is maximum (about $+0.6$) for a phase shift applied to w_r of $\phi_r \approx +10$ to $+40$ m or about $+0.1\lambda_r$. Thus, the results suggest that the roll-streak system may be associated with a down-gradient momentum flux and positive shear production and up-gradient buoyancy flux and positive buoyancy production. In a later section, we will separate by length scale and compare the turbulent vertical transport of momentum and buoyancy by these and all other structures and thereby explicitly quantify the impact of these structures on the evolution of the mean current and buoyancy profiles during the storm.

Modulation of smaller turbulence

The vertical section plots in Fig. 2.8 show that the streaks modulate smaller-scale turbulence as well as the shear and stratification that influence the energetics of smaller scales. In particular, the region of strongest $\partial u_r/\partial z$, which is to the left (lower y_r in roll coordinates) of positive streak anomalies ($u_r > 0$), is associated with a tongue of enhanced vertical velocity w variance, squared shear $S^2 = (\partial u/\partial z)^2 + (\partial v/\partial z)^2$ variance and stratification N^2 variance that extends downward and under the positive u_r anomaly, from the surface to the thermocline. In addition, the enhanced turbulence coincides with roll-scale downdrafts $w_r < 0$, which occur 20-40 m to the left of the streaks (toward lower y_r) and are correlated with cold temperature anomalies. This enhanced turbulence coincides with and is plausibly explained by strongly positive reduced shear, $S^2 - 4N^2 > 0$, in these regions (Fig. 2.8 (i)), which is indicative of both a gradient Richardson number $Ri_g = N^2/S^2 < 1/4$, hence the necessary conditions for instability are met (Miles 1961; Howard 1961; Hazel 1972), and substantial energy available to the turbulence via shear production (Turner 1979; Rohr et al. 1988;

Holt et al. 1992). Conversely, below the low-speed negative streak velocity anomalies ($u_r < 0$) turbulence is particularly weak and generally the reduced shear is negative and $Ri_g \geq 1/4$. For comparison, a similar set of sections is shown after the eye passage in Fig. 2.8 in order to highlight the remarkable degree of periodicity imposed upon the turbulence by the streaks/rolls before the eye, under strong surface forcing.

2.3.2 Thermocline

Do the streaks and rolls discussed in the previous section, or large-aspect-ratio structures more generally, influence the entrainment of cold water from the thermocline and thereby the SST in the LES?

To begin addressing this question, we describe the characteristics of the dominant large structures in the turbulence near the thermocline, where the cold water enters the surface boundary layer. There, large scales $\lambda > 3D_{N^2}$ represent a majority of the horizontal kinetic energy and buoyancy variance between phases II-III (Fig. 2.5). In addition, plan views of temperature at different depths in Fig. 2.6 show that the characteristics of the large structures are qualitatively different at the thermocline compared to the surface-layer streaks/rolls. At the thermocline, the large-scale variance is dominated by smaller $\sim$ 100-m-scale wave-like structures with crests and troughs perpendicular to the local shear vector $\partial\langle\mathbf{u}\rangle_{x,y}/\partial z$, which is rotated about 90° to the right of the wind stress. These wave-like features are reminiscent of organized Kelvin-Helmholtz (K-H) billows (Fig. 2.9), so we refer to them as such before explicitly comparing to theory and prior observations in the discussion section below.

The significant spatial modulation of the K-H billows is a feature of particular interest in such a large-aspect-ratio model domain. At the beginning of phase III, these features are organized into bands that are approximately parallel to the local shear vector, a few hundred meters wide, and spaced 1 km apart (Fig. 2.6 (g)). Each band is associated with an undulation in the thermocline and horizontal velocity (e.g., it is warmer on the bottom right and cooler on the top left side of each band in Fig.

2.6 (g)). These larger thermocline undulations are plausibly due to internal waves, but since these 1 km structures are not always this organized, we don't pursue a simple explanation for this kilometer-scale modulation. Nevertheless, the simulated axial coherence of the rolls (along lines of constant phase) is often at least several wavelengths, which is qualitatively consistent with existing albeit limited knowledge of axial coherence of K-H like billows observed in the atmosphere and laboratory (Thorpe 2002).

Although we do not explicitly plot the time evolution of the billows, we note that similar structures are prominent with different degrees of organization at most times in phases II-IV (c.f. Figs. 2.9 (a) and (c) with (b) and (d); see also Fig. 2.6). In addition, the temporal evolution of the radially-integrated horizontal wavenumber spectra of buoyancy variance and vertical kinetic energy at the time-dependent depth $z = -D_{N^2}$ both contain distinct local maxima at a wavelength λ that increases slowly from about 10-20 m at 15:00 on Aug 27 to about 100 m at 07:54 on August 28 (the beginning of phase III), during which time the depth D_{N^2} increases from about 10 m to 20 m. Hence, unlike the surface streaks/rolls, which are more ephemeral and sensitive to the time-variability of the mean flow/forcing, the presence of organized wave-like or billow structures at the top of the thermocline is relatively robust to variations in the large scale conditions, although their precise spatial orientation and organization, characteristic scale, and magnitude varies.

2.4 Evolution of the mean profiles

The temporal evolution of the large-aspect-ratio structures is both dependent on and impacts the evolution of the mean profiles of momentum, temperature, salinity, and hence buoyancy. This section describes the temporal evolution of the horizontally-averaged profiles of temperature, buoyancy, and momentum and then quantifies the

net effects of the turbulence, including at large scales, on the mean profiles of momentum and buoyancy via vertical fluxes.

2.4.1 Mean profiles and comparisons to observations

In addition to generating the turbulence, the hurricane forcing also drives the evolution of the mean profiles, including the acceleration, deepening, and cooling of the OSBL (Figs. 2.10 (a),(c) and (e)). The hurricane causes these rapid changes primarily by injecting momentum and kinetic energy into the OSBL, since the buoyancy fluxes are comparably modest.

For example, the forcing accelerates a sheared and surface-intensified mean current with speeds in excess of 1 m/s and shears in excess of 10^{-1} s^{-1} (Figs. 2.10 (c)-(d)). Even though the wind and currents are unsteady, the mean surface current vector points about $45° \pm 20°$ to the right of the wind vector until late in phase IV (Fig. 2.10 (e)), and the current vector rotates clockwise with increasing depth throughout phases I-IV, as in an idealized steady Ekman layer (Ekman 1905). In phase III, the wind rotates rapidly clockwise at an angular frequency of about $2f$ while fluctuating in speed as the eye passes (Fig. 2.3). As a result, the simulated angle between the ocean surface current vector and the wind vector is briefly reduced (Fig. 2.10 (e)), as the wind rotates clockwise faster than the ocean surface current. In phase IV, the current angle decreases throughout the OSBL at a rate of about $15-20°$ per hr as the wind direction stabilizes, as in an idealized inertial oscillation (Ekman 1905; Pollard, Millard 1970b).

The simulated OSBL depth begins deepening at the beginning of phase II and continues to deepen from about 10 to 30 m through the end of phase IV (Fig. 2.10 (a)-(b)). In addition, the overall extent of the deepening as well as the time of most rapid deepening, which occurs just ahead of the eye passage at the beginning of phase III, are reasonably similar to the observations (Fig. 2.11). In addition, the deepening is reasonably consistent with the theoretical model of wind-driven mixed

layer deepening without a bottom by Pollard et al. (1972), who's eq. 6.1 suggests a post-storm mixed layer depth of 34 m based on just the initial stratification profile and the maximum wind stress.

As the OSBL deepens, the simulated SST cools by more than 4°C ahead of the eye during phase II and by more than 6°C by the end of phase IV, similar to observations (see Fig. 2 of Glenn et al. 2016). In addition, the most rapid SST cooling occurs before the eye passage and earlier than the most rapid OSBL deepening, as observed (Glenn et al. 2016).

Interestingly, the mean OSBL profiles remain stratified ($\langle N^2 \rangle_{x,y} \sim 10^{-5}$ to 10^{-4} s^{-2}) as well as sheared ($\langle S \rangle^2_{x,y} \sim 10^{-4}$ to 10^{-3} s^{-2}) throughout the storm (Figs. 2.10 (b) and (d) and 2.11). In addition, the mean shear and stratification within the OSBL evolve similarly so that the mean profiles contain a region of approximately marginal stability within the OSBL (e.g., Thorpe, Liu 2009; Smyth et al. 2019), where $Ri_g = \langle N^2 \rangle_{x,y} / \langle S \rangle^2_{x,y} \approx \frac{1}{4}$ from about 5 m depth to about D_N^2 (Fig. 2.12). Above 5 m, Ri_g remains positive, but it is much less than $\frac{1}{4}$ due to the strong surface layer shear near the air-sea interface. During the eye passage, the mean shear and stratification in the OSBL weaken, and Ri_g decreases suddenly from just above 1/4 to just below 1/4 (Fig. 2.12 (a)). Thereafter, the Ri_g profile remains relatively consistent through the end of phase IV. A statistical measure of the spatial variability in Ri_g (Fig. 2.12) connects back to Fig. 2.8; the modulation of the reduced shear by the rolls occurs in conjunction with a reduced percentage ($50 - 75\%$) of the area from 5 m to the pycnocline that is locally unstable ($Ri_g < 1/4$). In contrast, without the rolls and after the eye, more than 75% of the area is locally unstable through most of the OSBL.

The reasonably good comparison between the simulated and observed OSBL depth and SST response suggests that the simulated turbulent transport processes that drive these changes in the LES may be relevant to and important in the real ocean. However, although the evolution of the simulated surface current direction is similar to

observations (in Fig. 2 of Glenn et al. 2016), and observed and simulated differences between top and bottom velocities are within about a factor of two, the magnitude of the simulated surface current is sometimes stronger than observed by more than a factor of 2. We attribute the stronger surface currents and weaker bottom currents in the LES to the absence of a pressure-gradient-driven flow opposed to the wind-driven surface current, which Glenn et al. (2016) found was significant via numerical simulations. We will return to a discussion of this missing process below.

2.4.2 Momentum flux

In this idealized simulation, the horizontally averaged velocity vector $\langle \mathbf{u}_h \rangle_{x,y}$ only evolves due to the Coriolis force and the convergence of turbulent vertical fluxes of momentum, that is

$$\frac{\partial \langle \mathbf{u}_h \rangle_{x,y}}{\partial t} + \mathbf{f} \times \langle \mathbf{u}_h \rangle_{x,y} = \frac{\partial \mathbf{F_m}}{\partial z},$$

where $\mathbf{f} = (0, 0, f)$ is the traditional Coriolis frequency in vector form. This section complements the previous description of the evolution of $\langle \mathbf{u}_h \rangle_{x,y}$ with a description of the turbulent momentum flux, $\mathbf{F}_m = \langle \nu_{SGS} \partial \mathbf{u}_h / \partial z - w \mathbf{u}_h \rangle_{x,y}$, which is dominated by the resolved flux $-\langle w \mathbf{u}_h \rangle_{x,y}$ throughout most of the OSBL.[2] We characterize this flux in terms of its magnitude and direction, and we decompose it into two scales: smaller and larger than $3D_{N^2}$ (with subgrid-scale fluxes lumped with small scales). In addition, we quantify the effective turbulent viscosity profile, which we define by

$$\nu_t = \frac{\mathbf{F}_m \cdot \partial \langle \mathbf{u}_h \rangle_{x,y} / \partial z}{|\partial \langle \mathbf{u}_h \rangle_{x,y} / \partial z|^2}. \tag{2.1}$$

This definition of the scalar turbulent viscosity ν_t does not account for the non-local component of $\mathbf{F}_m$, i.e. the component of $\mathbf{F}_m$ that is perpendicular to $\partial \langle \mathbf{u}_h \rangle_{x,y} / \partial z$ (e.g., Large et al. 2019), which modifies ν_t by 3% or less in this scenario. Nevertheless,

[2]The SGS terms are only significant within a few meters of the surface and in the thermocline, hence the mean response and large-scale structures are expected to be fairly insensitive to refining the grid resolution (see e.g., Whitt et al. 2019). Although it is prohibitively costly to significantly increase the resolution and test this in the large domain considered here, we confirmed this expectation by refining the grid resolution by a factor of 2 in all dimensions in a smaller domain.

we still quantify the non-local component of $\mathbf{F}_m$ via the angle Ω between $\mathbf{F}_m$ and $\partial\langle\mathbf{u}_h\rangle_{x,y}/\partial z$ (e.g., Large et al. 2019), since the magnitude of the non-local flux is as large as 25% of $|\mathbf{F}_m|$ and thus may significantly influence the evolution of $\langle\mathbf{u}\rangle_{x,y}$ but is not accounted for in some OSBL mixing parameterizations (e.g., Large et al. 1994b).

In this strongly-forced regime, the magnitude of the shear is always positive, and the evolution of the momentum flux is controlled by the surface stress (see Fig. 2.3), which sets the surface value of $\mathbf{F_m}$. We also find that $|\mathbf{F_m}|$ decays approximately linearly with depth from the surface to about $z = -D_{N^2}$ while entrainment is occurring during phases II-IV (Figs. 2.13-2.14). Deviations from a linear $\mathbf{F}_m(z)$ profile do occur, but they have a magnitude of only about $0.2u_*^2$ where the friction velocity $u_* = \sqrt{|\boldsymbol{\tau}|/\rho_0}$. In addition, the turbulent viscosity collapses to a virtually time-independent vertical profile when ν_t is made dimensionless by dividing by $ku_*D_{N^2}$ and the depth z is divided by D_{N^2} (e.g., Large et al. 1994b).

The decomposition of $\mathbf{F}_m$ into large and small scales (Fig. 2.14) shows that the flux is dominated by small wavelengths $\lambda < 3D_{N^2}$ at all depths and times. However, larger scales are non-negligible, particularly during phase II and the beginning of phase III in the top 10 m, where the streaks and rolls are prominent and large scales account for about 10-20% of the total flux. Just above the thermocline ($z = -D_{N^2}$), the large scale contribution to the flux is more intermittent and relatively weaker; it only just reaches 10% of the total flux at the beginning of phase III.

After the eye passage during phases III-IV, the acceleration of the OSBL continues, but the large-scale contribution to the flux is substantially smaller in percentage terms than before the eye. In addition, $|\mathbf{F_m}|$ briefly exhibits a relatively large ($\sim 0.2u_*^2$) positive deviation from the linear profile in the middle of the OSBL (at about 12:00 on Aug 28, perhaps because the wind is particularly strong and well-aligned with the shear, as shown in Fig. 2.10 (f)) but thereafter returns to a nearly linear profile that persists through the end of phase IV.

The angle Ω between the momentum flux and the mean shear vector is also plotted

as a function of time and scale in Fig. 2.14. In both the total and small-scale part, Ω is small but non-negligible, reaching maxima of about 15° and 10°, respectively, between about 5-10 m at the end of phase II (for reference, this implies that the non-local component is 17-26% of the total magnitude) With respect to the total and small-scale fluxes, Ω is very slightly negative at the surface, but positive throughout most of the OSBL during phase II. That is, the corresponding $\mathbf{F}_m$ vector is rotated counter-clockwise relative to the local shear $\partial\langle\mathbf{u}_h\rangle_{x,y}/\partial z$ and toward the wind stress vector $\boldsymbol{\tau}$ in most of the OSBL.

It may be noted that the total and small-scale non-local fluxes are correlated in time with large-scale non-local fluxes, which are associated with much greater Ω, particularly in the middle of the OSBL. Hence, we consider the hypothesis that the non-local momentum flux, i.e. the occurrence of $\Omega \neq 0°$ in Figs. 2.14 (d), (e) and (f), is due to the presence and modulating effects of the large-scale rolls/streaks. The evidence in support of this hypothesis is as follows: First, the magnitude ($w_r u_r \sim 10^{-4}$ m^2/s^2), depth range (top 10 m), and angle Ω of the large-scale fluxes (Fig. 2.14 (c)) are consistent with the roll structures described in section 3 (Fig. 2.7). In particular, Ω (Fig. 2.14 (f)) is slightly negative near the surface, where the streaks are rotated to the right of the wind stress and local shear, but Ω increases with depth as the mean shear vector rotates clockwise but the rolls and streaks remain at a fixed angle (see Figs. 2.6 and 2.7). Second, the temporal evolution of the non-local fluxes at small scales (Fig. 2.14 (e)) is similar to the temporal evolution of the streaks as well as the associated large-scale fluxes (compare to Figs. 2.5 (h) and 2.14 (c)). In particular, both the magnitude of the large-scale streaks/rolls and the small-scale non-local fluxes are largest during phase II and abruptly transition to much smaller values as the eye passes. Further, the small-scale turbulence is modulated by and more intense below the streaks ($u_r > 0$) (Fig. 2.8 (i)), where the large-scale shear vector is rotated counter-clockwise relative to the mean shear vector. To the extent this relationship is significant and strong, a positive Ω at small scales (Fig. 2.14 (e))

is expected at the base of the streaks while they are present. Together, all of this evidence suggests that the non-local momentum flux, at large and small scales, is directly or indirectly due to the presence of the large-aspect-ratio streaks and rolls. In addition, explicit models of these large-aspect-ratio structures may be necessary to model non-local fluxes in OSBL mixing parameterizations.

Thus, we conclude that the large-aspect-ratio structures fundamentally alter the evolution of the mean momentum profile in this scenario, but the magnitude of these modifications are relatively small ($\sim$10%) compared to the fraction of turbulent kinetic energy in these large scales, particularly during phase II and the beginning of phase III of the storm.

2.4.3 Entrainment and buoyancy flux

The rapid SST cooling and the associated impacts on the hurricane are driven by entrainment and the downward turbulent buoyancy flux as the OSBL penetrates into the cold thermocline. In particular, since the OSBL is approximately mixed and the mean buoyancy profile is highly correlated with the mean temperature profile (Fig. 2.2), the evolution of the SST is governed by the evolution of the buoyancy averaged over $z > -D_{N^2}$ (Stevenson, Niiler 1983), which evolves according to

$$\frac{\partial}{\partial t}\left(\langle b\rangle_{x,y,D_{N^2}}\right) = \frac{F_b(z=0) - F_b(z=-D_{N^2})}{D_{N^2}} - \frac{\Delta b}{D_{N^2}}\frac{\partial D_{N^2}}{\partial t}, \tag{2.2}$$

where $\Delta b = \langle b\rangle_{x,y,z>-D_{N^2}} - \langle b\rangle_{x,y}(z=-D_{N^2})$ and

$$F_b = \langle \kappa_{SGS}\partial b/\partial z - wb\rangle_{x,y}.$$

In addition, the evolution of the mean buoyancy profile is governed by:

$$\frac{\partial \langle b\rangle_{x,y}}{\partial t} = \frac{\partial F_b}{\partial z}.$$

Therefore, this section quantifies F_b and the related entrainment flux $F_e = -\Delta b \partial D_{N^2}/\partial t$ in order to evaluate the impact of the storm-driven OSBL turbulence, and the large-aspect-ratio structures in particular, on the evolution of the mean buoyancy and stratification profiles, entrainment, and SST cooling.

First, it is notable that the buoyancy flux profile F_b collapses when divided by F_e (Fig. 2.15 (c)). The maximum of F_b is found at $z \approx -3D_{N^2}/4$ throughout the storm, and the magnitude of this maximum is approximately equal to $3F_e/4$ on average (Figs. 2.15 (a) and (c)). About 80% of the temporal variance in the maximum of F_b (Fig. 2.15a) can be explained by variations in the rate of entrainment F_e. In addition, a similarly large fraction of the temporal variance in F_e (and F_b) can be explained by the rate of working on the surface current by the wind stress $\boldsymbol{\tau} \cdot \mathbf{u}(z = 0)$ divided by D_{N^2} (Fig. 2.16)[3]. During the end of phase III and the beginning of phase IV, when the angle between the wind and the current is relatively small (Fig. 2.10 (e)), the dot product in $\boldsymbol{\tau} \cdot \mathbf{u}(z = 0)$ is particularly crucial; it is only at this time that the conventional friction velocity scaling u_*^3/D_{N^2}, which works reasonably well in phases I-III and late in phase IV, is too weak. Hence, the rapid ahead-of-eye SST cooling in the LES is due to two factors: 1) the relatively large injection of kinetic energy from the wind to the OSBL ahead of the eye passage in phase II (due to the large friction velocity), and 2) the relatively small D_{N^2} at that time. The latter effect is quadratically important, since $\partial\langle b\rangle_{x,y,D_{N^2}}/\partial t \sim F_e/D_{N^2} \sim \boldsymbol{\tau} \cdot \mathbf{u}(z = 0)/D_{N^2}^2$ [see Eq. (2.2)].

Second, it is notable that F_b has a relatively large magnitude in the OSBL throughout the storm. Specifically, the flux Richardson number (Osborn 1980),

$$Ri_f = \frac{F_b}{\mathbf{F_m} \cdot \partial\langle \mathbf{u}\rangle_{x,y}/\partial z} \sim 0.1$$

throughout most of the OSBL. In particular, $Ri_f \sim Ri_g$ (Fig. 2.17), and hence the buoyancy flux is 10% or more of the shear production where $Ri_g \gtrsim 0.1$. That is, the strong wind makes buoyancy relevant to the turbulence energetics via entrainment, even though the Monin-Obukhov length is at least an order of magnitude greater than D_{N^2}, and the surface buoyancy flux $F_b(z = 0) << \max_z(F_b)$ is relatively small

[3]As Bill Large suggested to us, the shear production averaged above D_{N^2} explains F_e about as well as the wind work. Motivated by that suggestion, we also find that the surface stress dotted into the average shear above D_{N^2}, i.e. $\boldsymbol{\tau} \cdot \langle \partial \mathbf{u}_h/\partial z\rangle_{x,y,z>-D_{N^2}}$ explains the entrainment about equally well too.

(c.f. Figs. 2.3 (c) and 2.15 (a)).

Third, F_b is composed mostly of small scales $\lambda < 3D_{N^2}$, but large scales $\lambda > 3D_{N^2}$ make a non-negligible contribution to the total F_b (similar to $\mathbf{F_m}$) (c.f. Figs. 2.15 (a) and 2.14). Specifically, the large scales are responsible for a counter-gradient flux $F_b < 0$, which is equal in magnitude to 10-30% of the total $|F_b|$ in the upper 5-10 m during phases II-III. And, large scales are responsible for a down-gradient flux equal to 10-20% of the total F_b just above the thermocline during phases II-IV (Fig. 2.15 (a)). Plots of F_b as a function of horizontal wavelength and depth at the beginning and end of phase III in Fig. 2.18 highlight the spatial and spectral localization of the large-scale fluxes as well as the abrupt decay of the near-surface streaks/rolls and the associated large-scale fluxes during phase III. These spectra also provide explicit quantitative support for the hypothesis implicitly espoused in section 3: that there are a small number of distinct structures that dominate the large-scale dynamics, rather than a turbulent continuum at large scales. That is, although a scale separation is an imperfect way of separating the large-aspect-ratio rolls and billows from the turbulent continuum, the scale separation effectively achieves that end in this case. Most of the large-scale contribution to F_b can essentially be attributed to either the near-surface rolls/streaks in the top 10 m or the K-H like billows just above D_{N^2}, as described in Section 3. Nevertheless, caution is still warranted: some of the flux associated with these particular structures is apparently categorized as small scale (to the right of the red line in Fig. 2.18), and some of the large-scale flux is evidently not associated with the dominant large structures described in Section 3. With respect to the net flux, the near-surface streaks/rolls with wavelengths of a few hundred meters and a vertical extent of about 10 m convey both a down-gradient momentum flux and an up-gradient buoyancy flux before the eye passage. In addition, the K-H-like billows with a vertical extent of about 5 m and horizontal wavelengths of about 100 m convey both down-gradient momentum and buoyancy fluxes just above D_{N^2} both before and

after the eye passage, consistent with the respective descriptions of these two large-aspect-ratio structures in Section 3. That is, including the rolls/streaks increases the Prandtl number both by reducing the diffusivity and increasing the viscosity, whereas including the K-H structures just above the thermocline reduces the Prandtl number because viscosity is increased by less than the diffusivity.

Finally, it is notable that although the buoyancy flux varies systematically with the momentum flux such that the turbulent Prandtl number $Pr_t = \nu_t/\kappa_t$ is always near 1 [ν_t and κ_t are defined as in Eq. (2.1)], there are also persistent deviations $Pr_t > 1$ (Figs. 2.15 (b) and 2.17). In addition, these positive deviations in Pr_t coincide with and are partially attributable to: 1) the presence of the Ekman-layer rolls, which increase the overall Pr_t by reducing κ_t and increasing ν_t (see Figs. 2.18 (a),(c),(e); c.f. Figs. 2.17 (a)-(b)), 2) the increased mean-profile Ri_g, which is associated with higher $Pr_t = Ri_g/Ri_f$ and lower Ri_f relative to Ri_g for $Ri_g \approx 0.25$ (see Figs. 2.12 and 2.17), and 3) the non-local momentum flux during phase II, which does not directly modify Pr_t more than a few percent but is thought to be another consequence of the Ekman-layer rolls (Fig. 2.14). Conversely, the K-H-like structures do not directly increase Pr_t. Just above the thermocline, the scale-dependent Prandtl number is generally positive but less than 1/2 over the depth range and wavelengths characteristic of the K-H like billows, which are more effective at transporting buoyancy than momentum and thus directly contribute to lowering Pr_t and increasing Ri_f (ignoring the indirect effects of these structures on Pr_t via smaller wavelengths). Conversely, the scale-dependent turbulent Prandtl number associated with the near-surface streaks/rolls (Fig. 2.18) is negative. Although the Ekman-layer rolls certainly contribute to the elevated Pr_t by increasing the momentum flux and lowering the buoyancy flux (Fig. 2.18), a full analysis of Pr_t is beyond the scope of this paper.

In summary, although entrainment and SST cooling is controlled to a first approximation by the mean dynamics (i.e., it is a response to the wind work on the mean flow, as in Pollard et al. (1972)), the large-aspect-ratio structures contribute $\sim 10\%$

to the vertical buoyancy flux and thus may modify the SST response by $\sim 10\%$ (i.e., a few tenths or possibly even a whole degree C).

2.5 Discussion

Before concluding, we briefly compare our simulation study with a few prior observational studies focused on the instabilities of both the Ekman boundary layer and stratified shear layers, which are thought to be relevant to the near-surface streaks/rolls and the K-H-like billows near the thermocline, respectively. In the second section below, we explicitly discuss the possible significance and implications of two particularly important omitted processes, surface gravity waves and larger-scale ocean dynamics.

2.5.1 Comparisons with prior studies

Ekman layer rolls

Perhaps the most plausible dynamical causes of the simulated near-surface streaks and rolls are the linear instabilities of the Ekman layer (Kaylor, Faller 1972; Brown 1972; Asai, Nakasuji 1973; Lemone 1973; Duncombe 2017; Skyllingstad et al. 2017b). These instabilities produce helical rolls/streaks approximately aligned with the geostrophic wind in the atmosphere and surface stress in the ocean (often tilted at some small angle $\sim 10^{\circ}$ relative to the wind or stress) that are qualitatively similar to the near-surface streaks and rolls described in section 3 (e.g., compare Fig. 2.7 with Fig. 4a of Lemone (1973)). In particular, the roll circulation (v_r, w_r) as shown in Fig. 2.7 is typically surface intensified and inclined in the cross-roll-vertical plane. In addition, cross-roll wavelength $\lambda_r \sim 10 D_{Ek}$, where $D_{Ek} = \sqrt{2\nu_t/f} \approx 15$ to 30 m (where $\nu_t \sim 0.1 k u_* D_{N^2}$, see Fig. 2.13 (b)) (e.g., Lemone 1973; Asai, Nakasuji 1973; Sous et al. 2013).

There are also some notable similarities between the simulated streaks/rolls and observations of such features in the ABL, as reported by Lemone (1973, 1976). In

both this LES and the ABL observations, the roll-streak system is associated with a down-gradient momentum flux and positive shear production and up-gradient buoyancy flux and positive buoyancy production. Further, the simulated roll-scale modulation of small-scale turbulence, which is enhanced in roll downdrafts $w_r < 0$ that correspond with cold temperature anomalies, is qualitatively analogous to the ABL observations, in which turbulence is enhanced in roll updrafts that correspond with warm temperature anomalies.

There are also some notable differences between our simulated rolls/streaks and those observed by Lemone (1973, 1976). For example, the cross-roll velocity v_r was stronger and more organized than the streak velocity u_r in their ABL observations, whereas the streak velocity u_r is stronger and more organized than the cross-roll velocity v_r in these ocean LES. Second, Lemone (1973) only observed the regime where $D_{Ek} << D_{N^2}$ and thus found that $\lambda_r \sim D_{N^2}$, whereas in the LES $\lambda_r \sim 10 D_{N^2}$ and w_r is thus much weaker than v_r, unlike their ABL observations. Further, Lemone (1976) finds that the observed modulation of smaller-scale turbulence in the ABL is explained by roll-scale vertical transport of small-scale turbulence via w_r in the absence of strong coherent streaks u_r. Although vertical transport of turbulence plausibly contributes to the observed roll-scale modulation of turbulence in the LES, the strong simulated streaks and the close relationship between positive reduced shear (below $u_r > 0$) and enhanced turbulence in the LES suggests that the strong streaks also contribute energy to the smaller-scale turbulence via shear production and thereby the overall roll-scale modulation of small-scale turbulence in the LES.

Finally, there are numerous observational indications of helical rolls such as those simulated in the LES in the ocean (going back to e.g. Langmuir (1938); see section 1). However, we only make explicit comparisons to the particularly relevant, intriguing, and recent study of Gargett, Savidge (2020). They report observations of the coastal ocean boundary layer in 31 m of water under a hurricane on the South Atlantic Bight. As in the simulation reported above, they observe the oceanic response to

a hurricane that moved approximately northward and to the west of the observing tower over about a day. The maximum stress in their case is perhaps 50% weaker than in ours, but the temporal evolution is quite similar. The winds come from a fairly consistent direction as the storm approaches, they rotate rapidly and weaken as the eye passes, and then the winds stabilize their direction and intensify after the eye. Most interestingly, Gargett, Savidge (2020) also find coherent large rolls, which they attribute to Langmuir supercells that are strong as the storm approaches, wash away during the eye passage, and then re-emerge after the eye. The observed disappearance of the large rolls during the eye passage is qualitatively similar to the LES results above, although the observed forcing is dominated by waves whereas the LES forcing is dominated by winds, and their water column is essentially unstratified whereas ours is strongly stratified. A key conclusion of theirs, which our results seem to qualitatively endorse, is that steady-state non-dimensional parameters may be insufficient to qualitatively or quantitatively characterize some features of OSBL turbulence under rapidly variable forcing. They also speculate that the disappearance of the large structures during the eye passage may reflect a sharp sensitivity to a ratio of two timescales: a timescale over which the large structures grow, and a timescale over which the mean flow or forcing evolves. This hypothesis is plausibly relevant here as well, although the growth timescale of Ekman layer instabilities is thought to be much longer than Langmuir cells. However, future work is necessary to test this hypothesis. We return to a discussion of the potential implications of missing surface waves in the LES below.

However, direct comparisons to such oceanic observations from the glider, RU16, are not pursued here as the observation of variance in vertical motions at the timescales of a down cast or upcast was limited for RU16 as the glider was lost prior to bringing it back in so we were unable to retrieve the high time resolution or engineering data required for a flight model (e.g. Merckelbach et al. (2019)). Temperature, conductivity, and pressure data were recorded at 5 second frequency sent via the iridium

connections at surfacing spaced approximately three hours apart with between 5 and 7 downcast-upcast motions, without a flight model to unify up and down cast glider velocities and the number of casts through the mixed-layer during phase I-III of the storm, we lacked the temporal resolution to isolate the roll structures. Further, surface waves both invariably explain some of the helical roll structures in the real ocean and the phase offset due to the flattening of the orbital motions in shallow oceans cause the glider pressure sensor to express complicated signals, which complicates the comparison between the observations and this LES.

Kelvin Helmholtz billows

The simulated large-scale structures just above the thermocline are also qualitatively similar to various oceanic observations of billows associated with shear instabilities in that they reveal temperature overturns wrapped by broken braids of strong vorticity that in some (rare) cases form cats-eye patterns consistent with finite-amplitude Kelvin-Helholtz billows in regions with a mean-profile $Ri_g \approx 1/4$ (Seim, Gregg 1994; Chang et al. 2016). The crests and troughs of the simulated billows are oriented perpendicular to the mean shear vector at the depth of the thermocline, and their wavelength (about 125 m at the beginning of phase III) is consistent with the fastest growing linear K-H instability on a canonical $tanh(z/L)$ stratified shear layer with $L \approx 10$ m (Hazel 1972). However, the dominant-scale mode is also plausibly a result of merging or some other dynamical interaction and thereby associated with K-H modes of a similar but different size (e.g., with half the wavelength and $L \approx 5$ m; see e.g. Seim, Gregg (1994) and Smyth, Moum (2000); Smyth (2003)). But, an exact match to theory is neither expected nor pursued since the observed mean shear and stratification are not exactly consistent with the canonical tanh profiles and the K-H billows coexist with finite amplitude variance due to a range of other processes and scales (e.g., ambient turbulence lofted down from higher in the boundary layer; see Kaminski, Smyth 2019). Finally, it is worth reiterating that these billow-like

structures are more the exception than the norm, although they are still directly responsible for $\sim 10\%$ of the covariances.

2.5.2 Missing processes

Surface gravity waves

Even though the SST cooling and rapid entrainment response to Hurricane Irene is qualitatively represented in the LES, one missing process that might significantly impact the OSBL turbulence described above is surface gravity waves. A future study with the Craik-Leibovich (CL) equations (e.g., McWilliams et al. 1997; Tejada-Martinez, Grosch 2007; Sullivan et al. 2012; Van Roekel et al. 2012; Large et al. 2019) might elucidate some effects of the time-dependent and mis-aligned waves and winds. Our omission of the wave effects captured by the CL equations can be cast an assumption that the turbulent Langmuir number, i.e. $La_t = \sqrt{u_*/u_s}$ where u_s is the surface Stokes velocity (Li et al. 2005), is sufficiently large. Although calculating the Stokes velocity for the wave field under Hurricane Irene is beyond the scope of this paper, La_t is likely within the range of 0.1 to 1 most of the time (e.g., as in the scenarios studied by Sullivan et al. 2012; Gargett, Savidge 2020), and thus CL effects are probably non-negligible and likely dominant at some times. However, since the dominant waves (in the WaveWatch III simulation of hurricane Irene; `https://polar.ncep.noaa.gov/waves/hindcasts/prod-multi_1.php` (Chawla et al. 2013)) were often misaligned with the winds, which rotate rapidly, La_t itself may overestimate the CL effects (Van Roekel et al. 2012).

It is certainly plausible that the u_s is as much as 2-3 times that large, particularly when the winds are aligned with the waves (e.g., Sullivan et al. 2012), in which case the turbulence may be substantially modified or even dominated by wave effects. We might speculate that the Stokes production of turbulent kinetic energy near the surface will not dramatically alter the energetics of the OSBL turbulence, if the shear

and momentum flux vectors remain approximately aligned with the strong wind stress near the surface. However, the Eulerian mean shear and the turbulent momentum flux vectors rotate counter-clockwise with depth in a relatively shallow boundary layer, such that there is substantial production of turbulent kinetic energy throughout the boundary layer in the simulations reported here. Hence, we speculate that the Stokes shear might align with the Eulerian mean shear and the momentum flux vectors and thereby enhance turbulent kinetic energy production near the pycnocline (5-20 m) before eye passage but oppose the Eulerian mean shear and reduce turbulent kinetic energy production after eye passage (but note that the Stokes shear decreases rapidly with depth). However, some of the assumptions that lead to these conclusions may not hold in LES of the Craik-Leibovich equations in this scenario, e.g. non-local momentum fluxes are almost certainly non-negligible and plausibly dominant at some times/depths (Van Roekel et al. 2012; Large et al. 2019). Thus, if the upper-ocean shear is indeed aligned with the stress as simulated here, then we might speculate that the wave-driven Stokes shear would contribute relatively little to the turbulent kinetic energy budget in a simulation of the Craik-Leibovich equations, because Stokes production would be associated with non-local momentum fluxes if the mean shear is aligned with the stress in the upper 10 m as it is here. In addition, there are other wave effects not captured by the CL equations that make it difficult to conjecture about the impact of waves in this scenario. For example, one issue is that the peak significant wave height is 8 m (in the Wavewatch III model) in 35 m of water, and the wave dynamics are in the intermediate regime (with peak wave periods ranging from about 14 s to 7 s) where they are substantially modified by the shallow bottom. Further, wave-driven bottom boundary layer dynamics may also impact the evolution of the mean profiles (Grant, Madsen 1979, 1986) in ways not accounted for in either the LES reported here or an analogous simulation of the CL equations.

Pressure-gradient forces and large-scale circulation

A second mechanism that may cause the OSBL turbulence to differ in the real ocean compared to the LES is the large-scale dynamics. In comparison to the surface waves, the effect of this process on the OSBL turbulence is more indirect, although probably more significant for the mean profile evolution and fluxes. In particular, pressure-gradient-driven flows arise due to the interactions of the wind-driven flow with the coastal boundary (e.g., Kundu et al. 1983; Glenn et al. 2016; Kelly 2019). As reported by Glenn et al. (2016), this process is likely responsible for both the observed stronger bottom velocity and weaker surface velocity relative to LES. In addition, the strong bottom flow activates the bottom boundary layer. Hence, mixing of the thermocline will occur both from below and above. Since the pressure-gradient flows can induce a baroclinic response, they can both increase and decrease the vertical shear at the thermocline and could therefore reduce or increase mixing. Future work might evaluate the impact of the lateral pressure-gradient forces on the OSBL turbulence in this scenario by imposing these forces, as simulated in the ocean model of Glenn et al. (2016), on the LES, and thereby build on the surface fluxes imposed in the control integration discussed here. Likewise, future work can consider the impacts of lateral density gradients and the associated submesoscale frontal dynamics on the results presented here.

2.6 Conclusions

Hurricane Irene passed over the New Jersey Shelf on August 28, 2011. Ahead of the eye, wind-driven turbulent mixing led to rapid cooling of the SST by over 4°C, which contributed to energy loss via air-sea heat flux from the hurricane to the ocean and the resulting rapid decay from category 3 to category 1 during August 28 (Glenn et al. 2016; Seroka et al. 2016). Here, we report a large eddy simulation of the ocean turbulence at horizontal scales from 2 km to 1 m in a box of ocean just to the right of

where the eye passed in the middle of the New Jersey shelf. The simulation was forced by our best estimates of the time-evolving air-sea heat and momentum fluxes during the storm and the analysis focuses on the period of time when the winds strengthen and then rapidly rotate as the storm approaches and passes; the post-storm period when the winds decay and the simulated surface boundary layer extends to the bottom is left for future work.

Despite the omission of surface gravity wave effects and large scale ocean circulation dynamics, the simulation captures the observed rapid ahead-of-eye cooling of SST and deepening of the surface mixed layer. The results show that the rapid ahead-of-eye cooling was due to two factors: 1) the shallow and sharp thermocline before the storm, which facilitates both a relatively rapid SST response for a given entrainment rate, as well as a relatively rapid entrainment rate for a given wind forcing. And, 2) the magnitude and direction of the wind stress, which both facilitate the relatively large wind work that supplies the energy for entrainment. However, the most striking feature of the simulation and the focus of the analysis is on ephemeral large coherent structures with aspect ratios $\sim$10 that dominated the turbulent kinetic energy and buoyancy variance at various times and depths within the OSBL.

A descriptive analysis shows that the large-aspect-ratio structures have many similarities and some differences to the classic helical Ekman layer rolls in the top 5-10 m and Kelvin-Helmholtz billows just above the thermocline, both of which have been previously observed in the atmosphere and ocean and have a well-developed basis in linear instability theory. The simulated rolls have a peak characteristic speed of $\sim$10 cm/s and a wavelength of about 300 m just before the eye, only to be washed away by the rapid rotation of the wind as the eye passes. In addition, there is striking kilometer-scale spatial modulation of the K-H billows in the thermocline, which are present to some degree at most times but have a growing dominant horizontal wavelength, are far from spatially ubiquitous, and have varied degrees of organization. However, future studies are needed to fully understand the roll of large structures in

OSBL turbulence: studies with more realistic configurations may reveal the impact of missing processes on the turbulence. Thus, more idealized studies are required to clarify the details of the turbulence dynamics and energetics.

Analysis of the wavenumber spectra and co-spectra allow us to separate and quantify the contribution of the large scales to the turbulent kinetic energy and net vertical fluxes. We find that the large structures directly contribute more than half of the kinetic energy and buoyancy variance, $\sim 10\%$ of the total fluxes of momentum and buoyancy, and they may modify the turbulent Prandtl number by up to 50% (from say 1 to 1.5). Although these impacts on the mean profiles are substantial, the relatively small contribution of large scales to the total fluxes suggests that the large structures probably only modestly alter the mean profile evolution (by $\sim 10\%$). Consistent with this suggestion, profiles of momentum flux, buoyancy flux, and the corresponding turbulent viscosity and diffusivity nearly collapse to time-independent profiles when appropriately nondimensionalized, despite the transient nature of the dynamics. Nevertheless, if the SST evolution in a similar model scenario is desired to within better than perhaps 0.5° (or about 10%), then the large-aspect-ratio structures are probably important to account for explicitly. The simulated large turbulent structures have some qualitative similarities to known linear instability models. Thus, these linear models may be a useful starting point for parameterization development, but future LES in other parts of parameter space are probably necessary to provide guidance and validation.

Finally, since this LES is an idealized process simulation, which omits potentially important surface gravity wave effects and larger-scale ocean circulation dynamics, caution should be exercised in extrapolating from these results to the real ocean. Future simulations exploring the impacts of these and other missing processes as well as observational validation of the results presented here would be necessary to make robust conclusions about the dynamics of the large-aspect-ratio structures such as those simulated here under a hurricane. As mentioned above, such future efforts may

be warranted if models of the SST evolution under a hurricane are desired to within 10% accuracy.

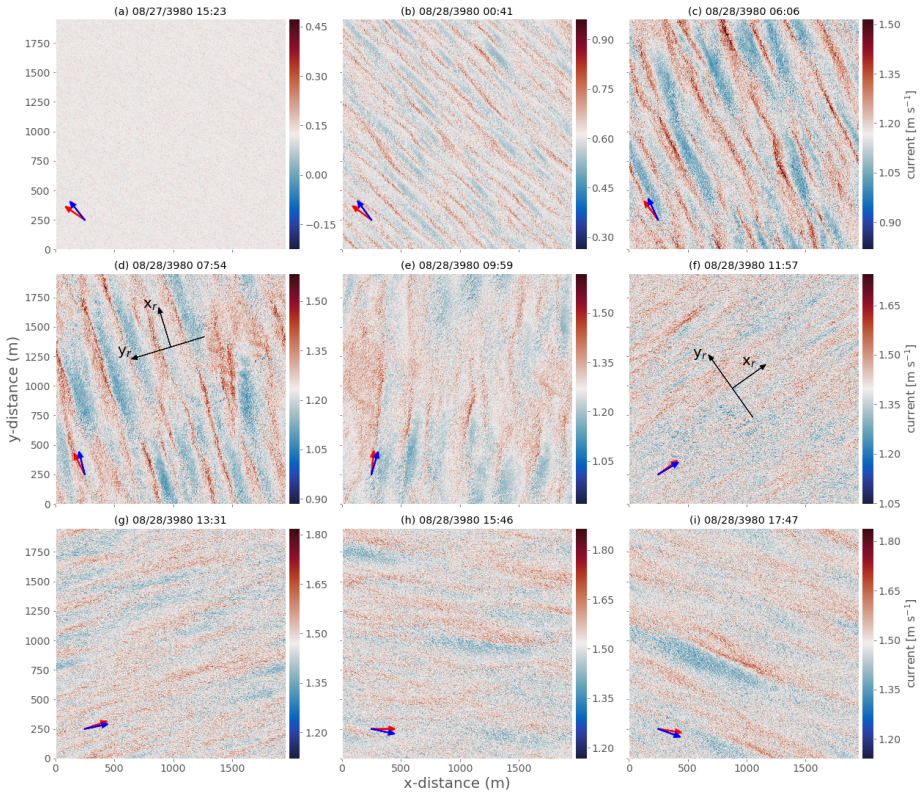

Figure 2.4: Snapshots showing the speed of the horizontal current 5 m below the surface at nine times during phases I (a), II (b)-(d), III (e)-(f), and IV (g)-(i) of the storm; the time points are indicated by blue dashed lines in Fig. 2.3 (a). The diverging colorbar is centered on the horizontal average to highlight the current anomalies. The domain is rotated counterclockwise 45° from the geographic coordinates referenced in Fig. 2.3 (b). Hence, winds initially from the east flow from the bottom right to the top left over the domain. As the eye of the storm passes during phase III (d)-(f), the source direction of the wind quickly rotates clockwise around the bottom of the domain to the left side, i.e. the southwest. The directions of the surface stress $\boldsymbol{\tau}$ and horizontally-averaged shear vector at 5 meters $\partial \mathbf{u}_h / \partial z$ are indicated by the red and blue arrows, respectively, in the bottom left corners. The roll coordinate charts used in Figs. 2.7-2.8 are overlaid in black.

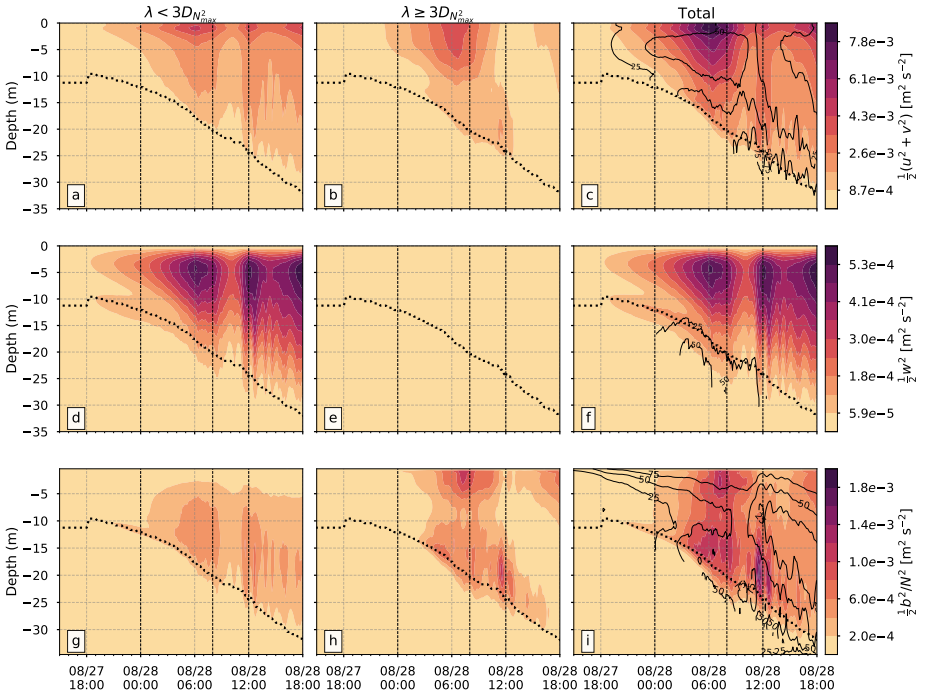

Figure 2.5: Horizontal (a)-(c) and vertical (d)-(f) kinetic energy of the perturbations from the depth-averaged flow, and (g)-(i) the buoyancy variance normalized by twice the mean vertical buoyancy gradient $\langle N^2 \rangle_{x,y}$. All three are decomposed using Fourier methods into wavelengths λ greater (middle column) and smaller (left column) than 3 times D_{N^2}, the depth of maximum $\langle N^2 \rangle_{x,y}$, which is marked by a black dotted line. The black contours (every 25%) in the right column indicate the percentage of the variance accounted for by large scales (shown in the middle column).

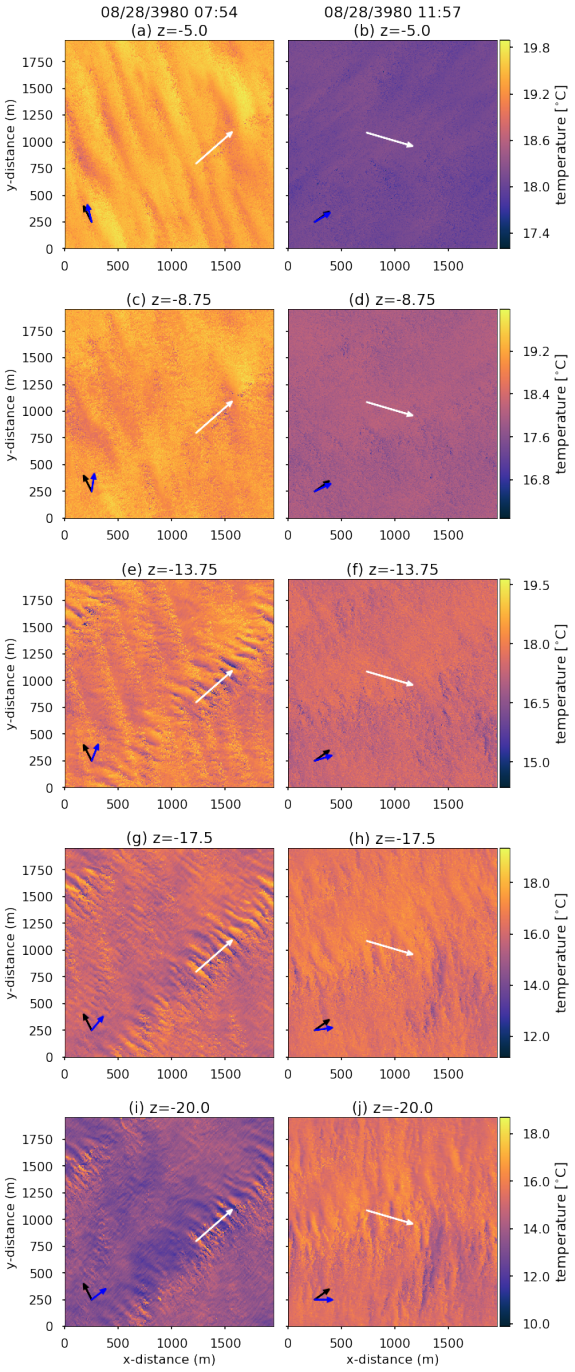

Figure 2.6: Snapshots of temperature at both the beginning (left) and end (right) of phase III and at several depths (top to bottom). The arrows in the bottom left corner indicate the direction of the surface stress $\boldsymbol{\tau}$ (black) and the horizontally-averaged shear vector $\partial \mathbf{u}/\partial z$ at that depth. The white lines indicate the location of the vertical sections in Fig. 2.9.

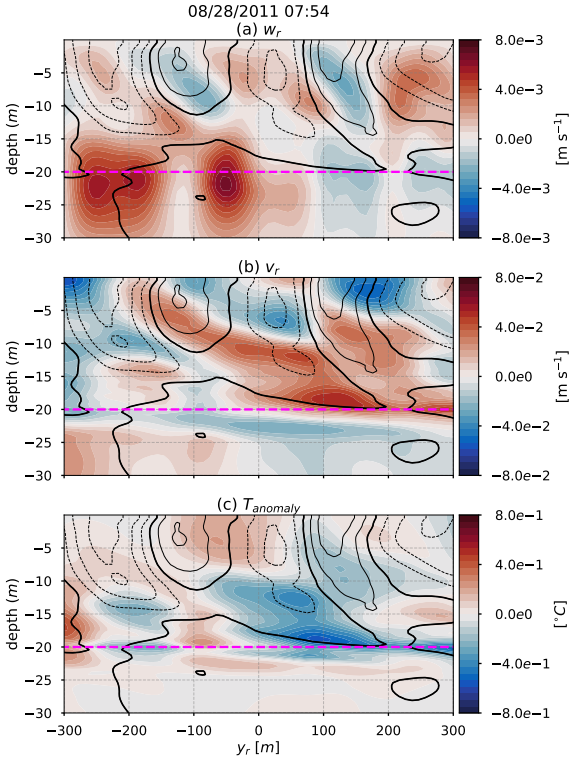

Figure 2.7: Vertical sections of vertical velocity (a), cross-roll horizontal velocity (b), and temperature (c), all of which are anomalies relative to the horizontal domain average. Overlaid is the streak velocity u_r (black contours every 4 cm/s) and D_{N^2} (magenta). The sections are along the cross-roll coordinate y_r shown in Figs. 2.4.4 and 2.4.6, after smoothing with a 25 m Gaussian filter.

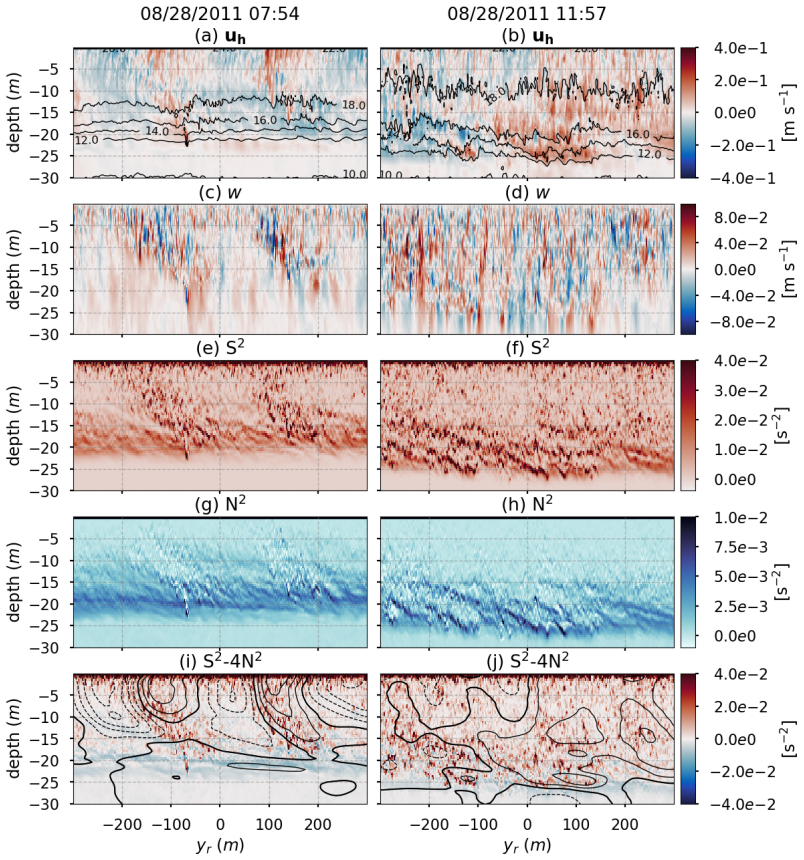

Figure 2.8: As in Fig. 2.7, but without smoothing: (a)-(b) anomaly in the horizontal speed $|\mathbf{u}_h|$, (c)-(d) vertical velocity w, (e)-(f) squared vertical shear of horizontal velocity S^2, (g)-(h) stratification N^2, and (i)-(j) reduced shear $S^2 - 4N^2$, just before (left) and just after (right) the eye. For reference, temperature contours are overlaid in (a)-(b) and smoothed u_r (also shown in Fig. 2.7) is overlaid in (i)-(j). The coordinate systems for before-eye and after-eye are plotted in Figs. 2.4.4 and 2.4.6, respectively.

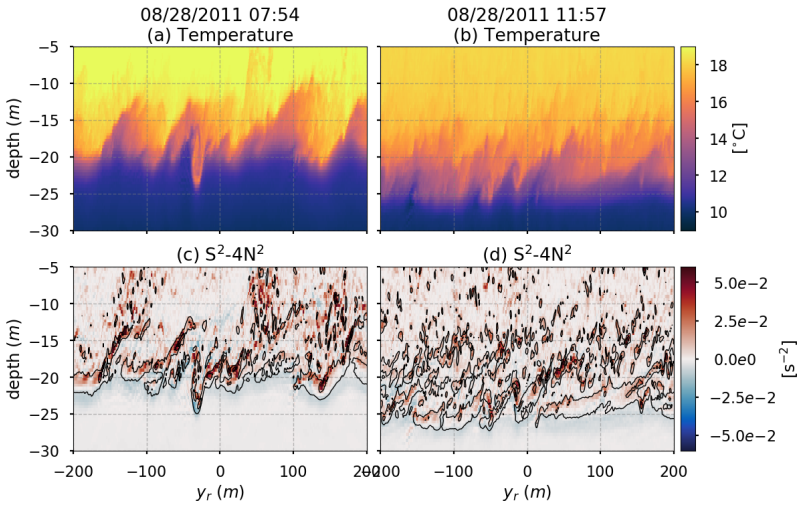

Figure 2.9: (a)-(b) Temperature and (c)-(d) reduced shear (with contours of cross-roll vorticity overlaid in black along the white coordinate lines in Fig. 2.6.

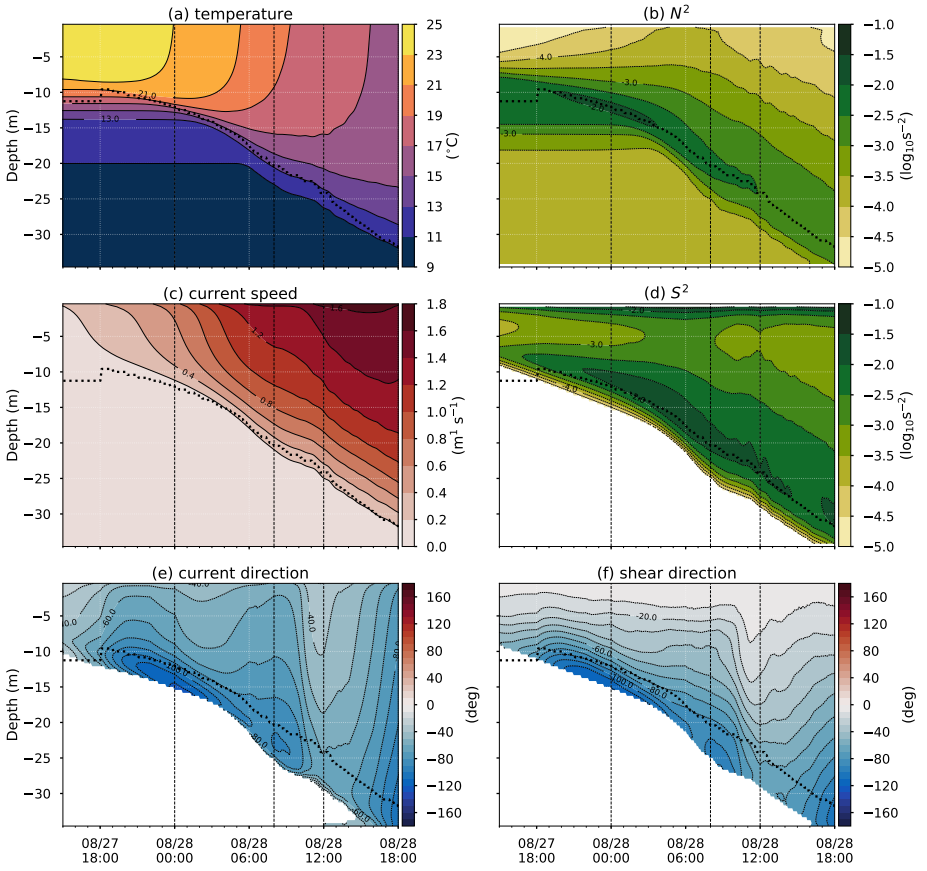

Figure 2.10: Mean vertical profiles of temperature (a), vertical buoyancy gradient N^2 (b), horizontal current speed $\mathbf{u}_h$ (c), vertical shear of horizontal velocity (squared, S^2), horizontal current direction (e), and shear direction (f). Both of the angles (e)-(f) indicate the direction the vector points and are given in degrees counterclockwise relative to the direction that the wind points. The angles are mostly negative and smaller than 90°, which indicates the current and shear vectors are to the right of the wind vector, as expected. Angles are only shown for speeds and shears greater than 10^{-3} m/s and s^{-1}, respectively. The dashed black line indicates the depth of maximum stratification D_{N^2}.

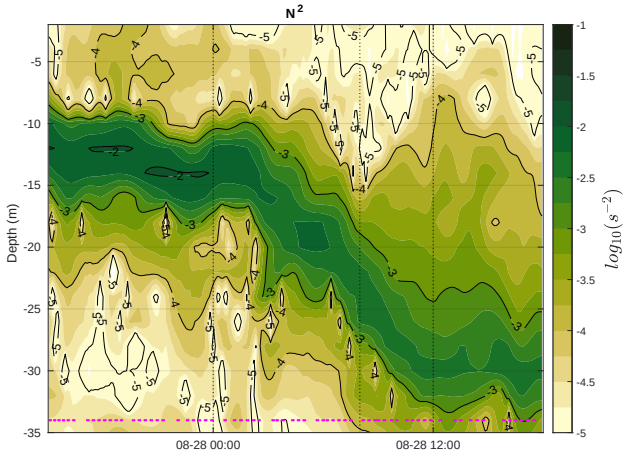

Figure 2.11: Observed buoyancy gradient N^2 in the region and time simulated by LES. Magenta dots at 34 m indicate the times of glider profiles sampled at 5 second resolution. The data have been linearly interpolated to a uniform 6 minute by 2 meter grid and smoothed with a forward-and-backward moving average with a 1 hour (10-point) box-car window and zero phase shift in an attempt to approximately mimic the spatial averaging that is applied in the analysis of the large eddy simulation.

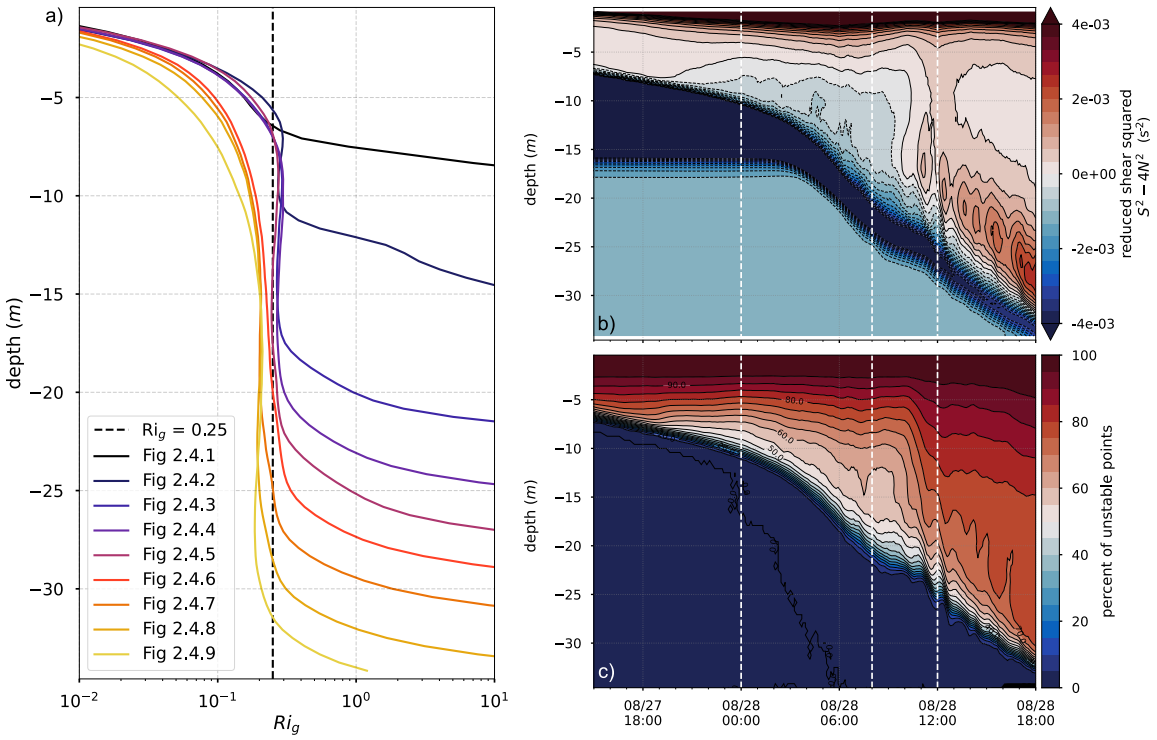

Figure 2.12: Profiles of the gradient Richardson number $Ri_g = N^2/S^2$ (a) and the reduced shear $S^2 - 4N^2$ (b) associated with the mean velocity and buoyancy profiles. The lower right plot (c) shows the percent of all points where the reduced shear is positive at each height. The profiles all cluster into two regimes that separate by time: before and after eye passage, which occurs at about 9:00 August 28 (see Fig. 2.3).

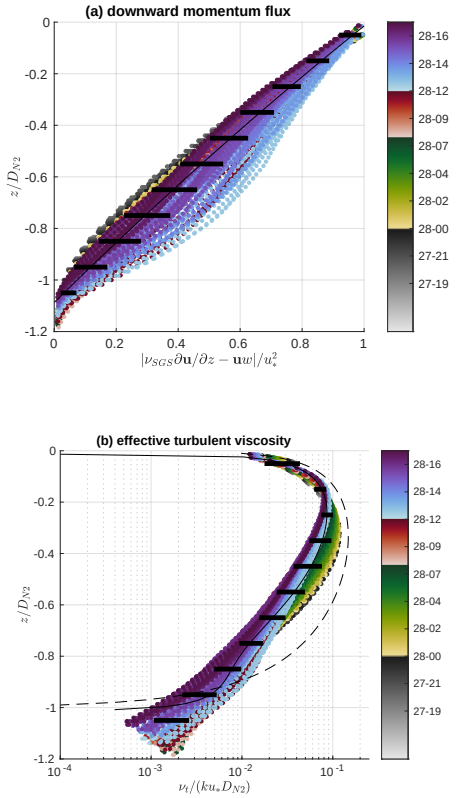

Figure 2.13: The momentum flux scaled by the friction velocity decays nearly linearly with decreasing z/D_{N^2} at all times when entrainment is occurring (colorbar, day-hour) (a). The correlation coefficient between z/D_{N^2} and $|\mathbf{F}_m|$, where $\mathbf{F}_m = \nu_{SGS}\partial\mathbf{u}/\partial z - \mathbf{u}w$, is 0.98. The best fit quadratic (for $z/D_{N^2} > -1.2$) has coefficients: -0.11, 1.18, and 1.09 (beginning with the highest order term). The effective turbulent viscosity, $\nu_t = \mathbf{F}_m \cdot \partial\mathbf{u}_h/\partial z/|\partial\mathbf{u}_h/\partial z|^2$, collapses when scaled by $ku_*D_{N^2}$, where $k = 0.4$ is the von Karman constant (b). The best-fit quartic (for $z/D_{N^2} > -1$) has coefficients: -1.28, 3.41, -3.09, 0.97, and -0.01 and explains 88% of the variance for $z/D_{N^2} > -1$. Standard deviations in eleven bins are indicated by thick black bars. The dashed line in (b) is the empirical function $-z/D_{N^2}(1 + z/D_{N^2})^2$; a similar function is used in the K-profile parameterization scheme of Large et al. (1994b).

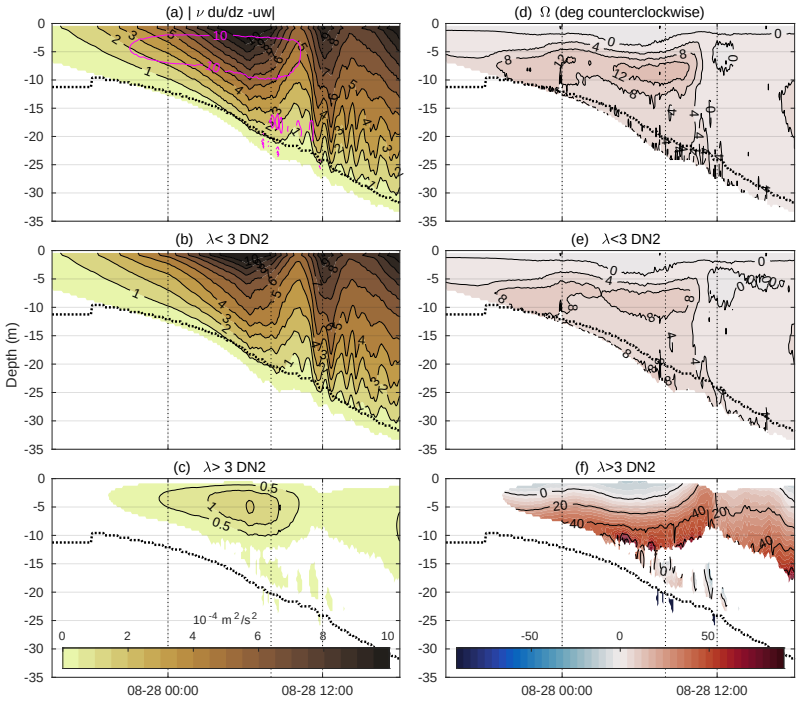

Figure 2.14: The magnitude (left) and direction (right) of the downward vertical momentum flux vector $\mathbf{F}_m = \langle \nu_{SGS} \partial \mathbf{u}_h / \partial z - w \mathbf{u}_h \rangle_{x,y}$. The direction is given relative to the local mean shear vector $\langle \partial \mathbf{u}_h(z,t)/\partial z \rangle_{x,y}$, which is shown in Fig. 2.10 (f). The total flux (a) is also decomposed, via Fourier transforms, into small scales (b), horizontal wavelengths less than $3D_{N^2}$, including subgrid scales), and large scales (c), horizontal wavelengths larger than $3D_{N^2}$). For reference, the black dotted line indicates D_{N^2}. The subgrid-scale flux $\nu_{SGS} \partial \mathbf{u}_h / \partial z$, which is only significant and comparable in magnitude to the resolved flux $|-\mathbf{u}w|$ just below the surface and near the base of the boundary layer, is entirely allocated to the large wavenumbers in (b) and (e). The magenta contours in (a), marked every 10%, indicate the percentage of the total flux that is attributable to large scales.

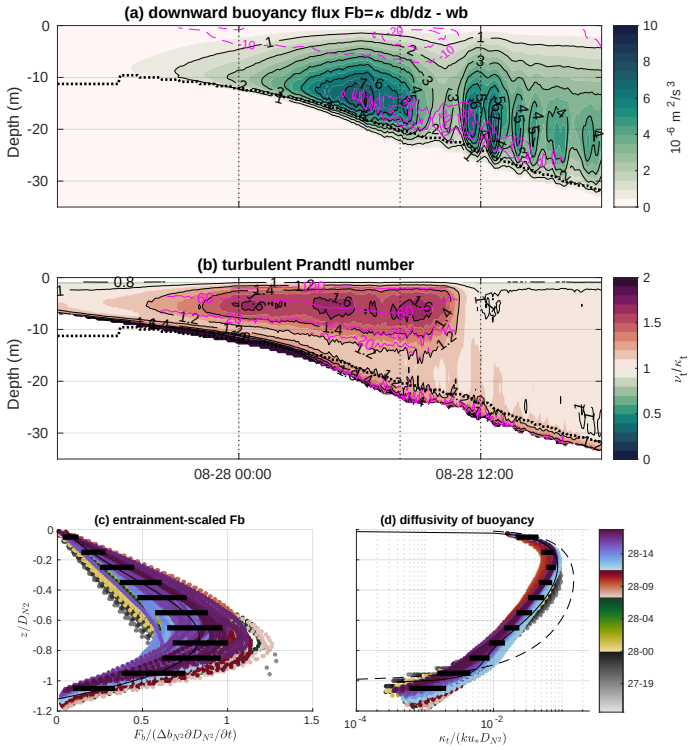

Figure 2.15: (a) The vertical buoyancy flux $F_b = \langle \kappa_{SGS} \partial b/\partial z - bw \rangle_{x,y}$, which is collapsed in (c) by dividing by the entrainment buoyancy flux $F_e = \Delta b \partial D_{N^2}/\partial t$, where Δb is the difference between the depth-averaged buoyancy above D_{N^2} and the buoyancy at D_{N^2}. The colorbar in (c)-(d) indicates the time (day-hour). The best-fit cubic in (c) (solid black line), which explains 86% of the variance of F_b, has coefficients: -3.07, 2.82, 0.65, and 0.05 (from highest to lowest order). The turbulent diffusivity profile $\kappa_t = F_b/N^2$ in (d) is very similar to the turbulent viscosity profile ν_t (plotted in Fig. 2.13 b), but the turbulent Prandtl number $Pr_t = \nu_t/\kappa_t$ systematically differs from 1, as shown in (b). For reference, magenta contours in (a)-(b) quantify the percentage of F_b and $Pr_t - 1 > 0.2$, respectively, that are attributable to fluctuations with wavelengths greater than $3D_{N^2}$. In both (c)-(d), horizontal black bars indicate standard deviations in eleven depth bins. For reference, the depth D_{N^2} (dotted black) is overlaid in (a) and (b), and the solid black and dashed black curves in (d) are the same dimensionless viscosity model profiles as in Fig. 2.13(b).

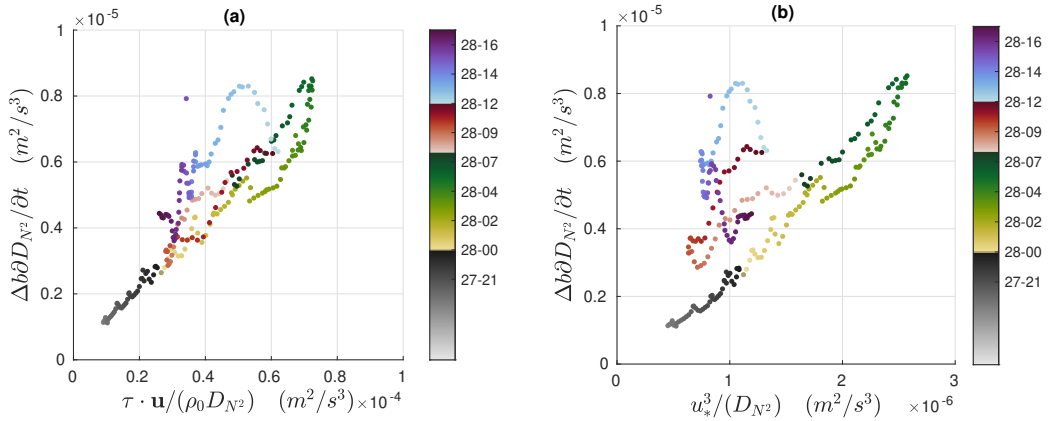

Figure 2.16: The relationship between the entrainment flux F_e and the rate of working on the surface current by the wind stress (a, $r^2 = 0.75$, linear regression slope = 0.1) and the friction velocity u_*^3 (b, $r^2 = 0.37$, linear regression slope = 2.0) during entrainment. The colorbar indicates the time (day-hour).

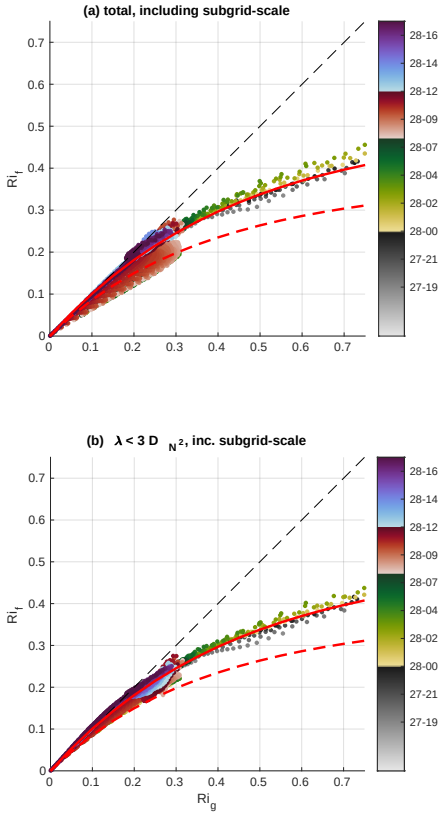

Figure 2.17: The relationship between the gradient Richardson number Ri_g and flux Richardson number Ri_f above the depth of maximum stratification D_{N^2} where Ri_f is either as simulated (dots) or determined from Ri_g via $Ri_f = 0.5(1-e^{-2.25Ri_g})$ (the solid red curve), which explains 93% and 98% of the variance in (a) and (b), respectively (e.g., Venayagamoorthy, Koseff 2016). In (a), the simulated Ri_f is calculated using the total buoyancy and momentum fluxes (including the subgrid scales), whereas in (b) the simulated Ri_f is calculated using only the wavelengths $\lambda < 3D_{N^2}$ (and the subgrid scales). The dashed red curve is a parameterization based on the ABL measurements (Anderson 2009), which parameterizes the subgrid-scale Ri_f in the LES (see section 2). The colorbar indicates the time (day-hour).

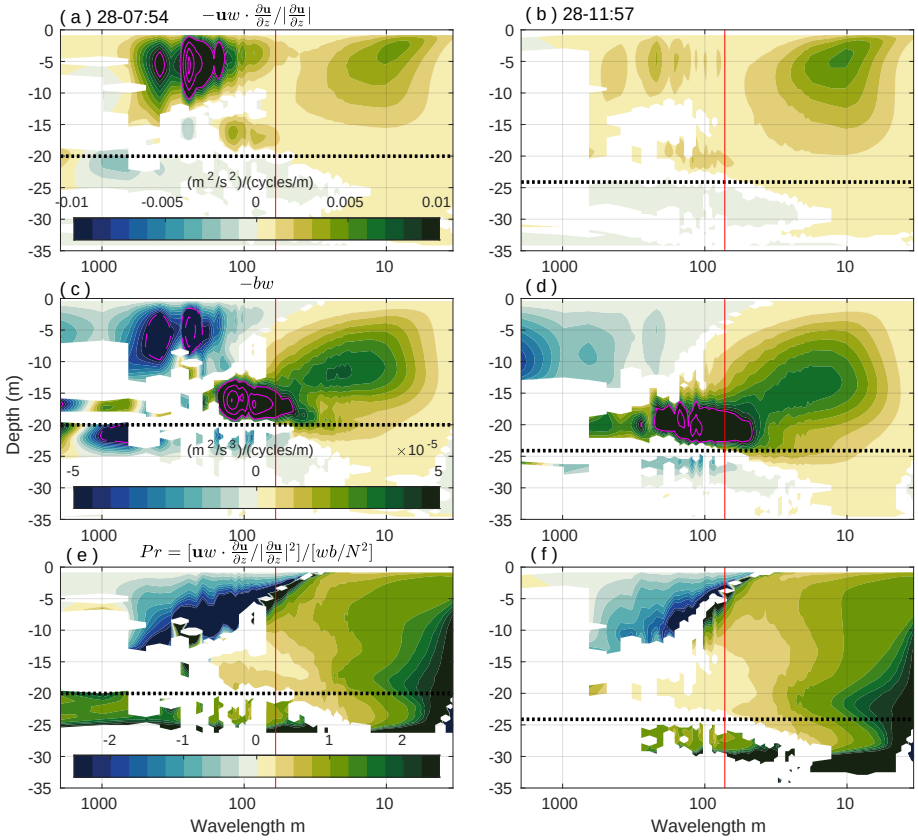

Figure 2.18: Momentum and buoyancy flux cospectra at each depth averaged over two-hour windows centered at the beginning (left) and end (right) of phase III (see Fig. 2.3). Magenta contours, which are given every 0.01 $m^2/s^2/(cycles/m)$ in (a) and 0.00005 $m^2/s^3/(cycles/m)$ in (c) and (d), respectively, highlight regions and wavelengths of particularly strong co-variance before and after eye passage. Areas where the covariance is not significantly different from zero are blanked. The dotted black horizontal lines indicate the depth D_{N^2} and the vertical red lines indicate the wavelength $3D_{N^2}$. The ratio of the relevant covariances, i.e. the flux Richardson number Ri_f, is decomposed by horizontal wavelength λ and written as a turbulent Prandtl number $Pr = Ri_g/Ri_f$ in (e) and (f), where $Ri_g = \langle N^2 \rangle_{x,y} / \langle S \rangle^2_{x,y}$ is the gradient Richardson number of the horizontally-averaged velocity and density profiles.

Chapter 3

Observing the response, across the MAB, using SLIM

3.1 Introduction

Wind-driven mixing of the ocean surface boundary layer often produces a mixed layer of nearly uniform density delineated above by the air-sea interface and below by the pycnocline, defined as a rapid increase in the buoyancy-gradient at the base of ocean surface boundary layer (Large et al. 1994a; Carvalho et al. 2017). The mixed layer is a transient feature of the upper ocean, dependent on entrainment mixing, seasonal variations in solar input, and regional current patterns, storage zone for heat that interacts and feedbacks on the atmosphere during storm events (e.g Elsberry et al. (1976); Jacob et al. (2000)) and through seasonal variations in weather patterns (e.g. Dong, Kelly (2004); Jansen et al. (2010)). The mixed layer depth (MLD) varies greatly across the world's ocean in both time and space (Woods 1980; Belcher et al. 2012; Kim et al. 2015; Toyoda et al. 2017), and has been observed to correlate with variations in biological productivity (Behrenfeld et al. 2006; Carvalho et al. 2017). An accurate characterization of the surface MLD plays a critical role in understanding the dynamics of the ocean as the interface of the ocean-atmosphere coupled system, such as (a) bulk convection and entrainment (e.g. Large et al. (1994b, 1997)), (b) serving as a climatological boundary for the atmosphere-ocean coupled system (e.g. Lorbacher et al. (2006); Seroka et al. (2018)), (c) interactions with density fronts (e.g Taylor, Ferrari (2010); Whitt et al. (2019)), and (d) sensitivity to storm track, intensity, and near-inertial excitation (e.g. Zhang et al. (2018a)). The MLD integrates

ocean-atmosphere interactions. On the global scale it reflects wind stress and wind variability, as well as the other energetic inputs into the upper ocean such as radiative forcing, buoyancy injection from fresh water, and three-dimensional ocean processes such as tides and currents (de Boyer Montégut et al. 2004). Thus, the uniform temperature, salinity, and density of the surface mixed layer effectively acts as a single layer communicating stress from surface winds into the ocean interior, which lead to variations in the depth of the mixed layer due to mixing and entrainment. These changes in depth influence the biological capacity of the water column by the buoyant trapping of phytoplankton at the base of the mixed layer as the depth and optical properties of the mixed-layer influence the availability of light and nutrients (Kraus, Turner 1967; Ambler et al. 2013; Chen et al. 2018). In this paper, we will develop an algorithm to observe changes in MLD and use this to gain a better understanding of the dynamics of the coastal ocean in the Mid-Atlantic Bight (MAB) over synoptic to seasonal time-scales.

The focus of this study is the MAB, a geographic region of the continental shelf between Cape Hatteras in the South and the Gulf of Maine or the Nantucket Shoals in the North (Houghton et al. 1982). For coastal oceans such as the Mid Atlantic Bight, the mixed layer behaves differently than in the open ocean because it can interact with the relatively shallow bottom boundary. Along the the very shallow inner continental shelf, the mixed layer can deepen to become a well-mixed, single layer in direct contact with the bottom. The coastal ocean can then reform a two-layer system through surface or horizontal fluxes, evolving on timescales ranging from synoptic to seasonal, rendering the observational techniques of the open ocean insufficient to describe the time-dependent behavior (Austin, Lentz 2002; Mountain 2003b). The spatio-temporal connection of the mixed layer in the MAB with the cooler waters under the seasonal thermocline, known colloquially as the cold pool (Houghton et al. 1982) controls the transfer of momentum into the coastal ocean. Thus mixing and transport of the mixed layer in the MAB mediates the interaction

between the ocean and atmosphere during coastal storms (Miles et al. 2013; Seroka et al. 2016). The MAB is representative of many mid-latitude shallow coastal seas with large stratification based on seasonal trends such as the Yellow Sea in Asia (e.g. Chu et al. (2005)), many of the interstitial European Seas (e.g. Charria et al. (2017)), and the Australian and Patagonian coasts in the Southern Hemisphere (e.g. Mahjabin et al. (2019); Matano, Palma (2018)) among others.

The ability to infer MLD across a region of broad spatial extent from remote sensing observations offers opportunities for examining the role of MLD variability in driving such processes as primary productivity (Carvalho et al. 2017), internal waves, the relationship of river plumes and coastal oceans (Flagg et al. 2006; Moum, Nash 2008; Chant 2012), and driving ahead-of-eye cooling in tropical cyclones (e.g., Seroka et al. (2016); Glenn et al. (2016)). The coastal MLD is not a direct proxy for the traditional definition of stratification in the MAB—the Cold Pool, which is defined as a bottom trapped, high salinity relative to the surface, and low temperature water mass originating in the Scotian Shelf that is then capped by seasonal warming and riverine fresh water inputs (Bigelow 1933; Houghton et al. 1982; Mountain 2003b; Lentz 2008; Zhang et al. 2014). A distinctive aspect of the MAB is the process by which the stratified two-layer coastal ocean of Summer into early Autumn undergoes the Fall transition from the two-layer Summer flows where the diurnal heating is enough to maintain a shallow, bottom-detached MLD to a single layer, cooler system in the Winter as winds increase and incoming solar radiation decreases (Houghton et al. 1982). Hence, even as the seasons progress and the bottom waters are warmer than canonical cold pool waters of $10°C$ (Mountain 2003b), the response to atmospheric forcing will still be as a two-layer system.

In situ temperature, salinity or density profiles are required to identify the MLD, which severely limits MLD estimates to available thermistor or CTD profiles globally. This is due to the fundamental definitions of the mixed-layer being developed from profile records, where a set change or rate of change in temperature, salinity, or

the combined effective buoyancy gradient can be determined (Kara et al. 2000). For coastal regions, where rapid transitions can occur in response to and at similar time-scales to atmospheric forcing, the ability to remotely sense MLD and its potential rapid evolution in space and time will enhance our ability (a) to understand the role of the coastal ocean in regulating the impact of tropical cyclones (Glenn et al. 2016) and (b) control the amount of solar energy available to the phytoplankton community by regulating the diffusion of light and concentration of nutrients at density interfaces (Zhang et al. 2018a; Carvalho et al. 2017). The single parameter of the mixed layer most correlated to the dynamical response of upper ocean currents to high-frequency wind forcing is the depth, with studies dating back to the relatively simple slab model of Pollard and Millard (Pollard 1970; Pollard, Millard 1970a). The slab model assumes a one-dimensional, two-layer ocean where the surface water is homogeneous and of a certain thickness to approximate the stratification of the ocean. The response to the momentum transfer is then modeled as a damped-harmonic oscillator to recreate the relationship between wind-forcing and the inertial currents produced in the mixed layer. The intuitive motivation for the slab model is developed from the Newtonian principle that for a given transfer of momentum, the inertial response correlates inversely to mass, and thus to the thickness of the mixed-layer slab, defined here as h_o similar to the notation used in D'Asaro (1989). The damping in the Pollard-Millard slab model is related to both shear-driven turbulent losses at the bottom of the slab, and the radiation of energy away from the mixed-layer in the form of internal waves, and as such the inertial energy in the mixed-layer erodes exponentially in time (Pollard et al. 1973; Large et al. 1994a).

Recently, other researchers have used a version of the slab model to estimate the MLD at a point using wind data and the surface velocity from HF radar (e.g. Shrira, Forget (2015); Zervakis et al. (2017)), illustrating the capacity of the slab model to recreate a time-series of ocean properties. In order to extend this work to be capable

of generating regional maps of the ocean mixed-layer, we further developed and optimized the inverse calculations while harnessing the expansive Mid-Atlantic Regional Association Coastal Ocean Observing System (MARACOOS) HF-radar network to develop the Slab Lagged Inertial Model (SLIM) to output MLD at high resolution in both time and space. The only other current methodology for remote sensing of MLD relies on satellite observations to either use the hydrodynamic variation of surface waves due to changing internal wave orbital velocity (Li et al. 2000), or use wave damping by surface films due to surface convergence and divergence in the internal wave field (Choi et al. 2019). Both require robust internal wave fields to be present and any current satellite-based methodology requires limited cloud cover so that the sea-state can be observed. The model presented in this paper has no such requirements and extends the spatial and temporal capacities by using HF-radar derived current maps. Importantly the method presented here permits data on cloud-covered days, which are critical during storms, thus allowing for a more thorough understanding of how the coastal mixed-layer evolves over synoptic to seasonal time-scales.

3.2 Data

In order to build SLIM, we combine reanalysis wind products, as well as data from an integrated ocean observatory including autonomous underwater gliders and HF Radar. For wind-stress, we used reanalysis wind products from the North American Mesoscale Forecast System (NAM) run by NOAA at 12km spatial resolution and 6-hour temporal resolution. NAM is designed to accurately capture the large-scale phenomena and temporal variability on the synoptic timescale (Rife, Davis 2005). Calibration of the model required the *in situ* measurements made possible by Teledyne-Webb Research Slocum glider profiles available from the International Ocean Observing System (IOOS) Glider Data Assembly Cyberinfrastructure (DAC) (Testor et al. 2019). Gliders are autonomous underwater vehicles (AUVs) that have

become useful platforms for monitoring the ocean's response to storms (Domingues et al. 2019). Gliders can profile the water column from the surface to depths of up to 1000m and continuously sample every two seconds to provide a high temporal resolution time series along profile trajectories.

Since 2007, Mid-Atlantic Regional Association Coastal Ocean Observing System (MARACOOS) has operated a regional high-frequency radar (HFR) network consisting of approximately 41 radars, operated and maintained by a regional collaboration of eight organizations as described by Roarty et al. (2020). From this HFR network, we utilize the 6km resolution data product of the surface currents within 250 km of the coast, which covers the region where the strong seasonal pycnocline develops. We use a 10-year MARACOOS HF-radar dataset with enhanced quality control (Roarty et al. 2020).

3.3 Methods

Classically, the Pollard-Millard slab model has been used to infer the amplitude response at the near-inertial frequencies of surface currents to surface wind forcing given an assumption of MLD. The accuracy and intuitive value of the slab model has been used and validated by several investigators with *in situ* measurements and simulations (e.g. D'Asaro (1989); Jeronimo, Gomez-Valdes (2010); Nam, Park (2013)). Here, we develop the Slab Lagged-Inertial Model (SLIM) by inverting this classical dynamical dependence and demonstrating that we can predict spatial and temporal trends in MLD by using a combination of hourly surface current observations from HFR and surface wind data from a numerical weather prediction model. With this system it is possible to predict MLD variability over large horizontal extents and through time—according to the resolution and scope of the HF-radar network. For our study, the water surface current velocity is filtered in time to the near-inertial band and the model allows for the possibility of time-lags between the modeled windfield and the

observed ocean-response to mitigate event timing errors in the atmospheric model.

Specifically, the mixed-layer depth can be calculated from the x and y components of the momentum equations,

$$\frac{\partial u_s}{\partial t} - f v_s = \frac{\tau_x}{\rho_w h_s} - r u_s \tag{3.1}$$

$$\frac{\partial v_s}{\partial t} + f u_s = \frac{\tau_y}{\rho_w h_s} - r v_s, \tag{3.2}$$

where ru_s and rv_s represent the linear damping of momentum with r^{-1} as the e-folding decay time, ρ_w is the density of the water in the slab, $\tau_{(x,y)}$ is the calculated wind stress in the x and y-directions respectively, and f is the local inertial frequency. As described in Pollard, Millard (1970a), the slab model stratification is a step-function such that there are no natural frequencies other than the inertial frequency and the modifications on the inertial frequency due to the local decay constants. Continuing to follow Pollard, Millard (1970a), we define the wind-driven body acceleration on the slab ocean as follows:

$$\tau_{(x,y)}(t) = \rho_a C_D U_w(t)^2 (\cos\theta(t), \sin\theta(t)), \tag{3.3}$$

where $(U_w \sin\theta, U_w \cos\theta)$ are wind vectors from NAM, C_D is the surface drag coefficient, and ρ_a and ρ_w are the density of air and water respectively. Pollard, Millard (1970a) noted that the damping term has the effect of shifting the dominant frequency response of the model to a frequency slightly less than f, which we captured in the HFR data with a bandpass filter for the near-inertial currents (NIC) with frequency cutoff as 0.9 and 1.1 times f. The bandpass was done using a Butterworth filter where f was calculated for each geographic location.

In order to capture the mixed-layer depth from the inertial velocity in the HFR signal, we developed an algorithm to compare bandpassed-NIC in the HFR data with those generated by an initial guess of slab depth ($h_o = 10$m). The decay constant equivalent to an e-folding time of 2 days ($r = 5.78e-6$) in concert with regional estimates from the MAB in Kelly (2019), as the decay constant for inertial motions

is known to vary both regionally and temporally (D'Asaro 1989; MacKinnon, Gregg 2005; Park et al. 2009; Zhang et al. 2014). By integrating equations 3.1 and 3.2 using the Fourth Order Runge-Kutta method and inputting equation 3.3 with time-series data wind speed and direction, $U_w(t)$ and $\theta(t)$ respectively, at each geographic location within NAM, we generate the predicted near-inertial response of the 10m slab as a time-series, $U_s(t)$. The initial conditions for $U_s(t)$ are $u_s = v_s = 0$ and a spin up time of five days to minimize the extended effects of wind history on inertial amplitude, such that the solution is insensitive to the initial conditions.

In order to evaluate the responses, we generated an error function, $\mathbf{J}$, comparing the inertial velocity sensed by HF radar and the predicted slab ocean responses:

$$\mathbf{J}(h_s, L, t_i) = \sum_{t \pm 1.5 \text{ days}} w(t_i, t) \left| U_{hfr}(t) - U_s(t - L)\frac{h_o}{h_s} \right|. \tag{3.4}$$

The terms of the equation are given by: $U_s(t)$ is the magnitude of the predicted slab inertial current, augmented by the weighting function, $w(d) = (1 - d^2)^2$ with $d = \frac{|t_i - t|}{t_{win}}$ where t_i is the current time and t_{win} sets the window size at ± 36 hours (Micchelli et al. 1976), and $U_{hfr}(t)$ is the magnitude of NIC observed in HF radar at time t. We vary a time-lag, L, on the wind forcing over the three day window to minimize any error from mistiming of the weather model to real wind forcing and the time-smoothing inherent in the CODAR processing algorithms (Roarty et al. 2010). By allowing L into the cost function, we alleviated the requirement of being exactly in-phase between the HF radar and wind-derived slab ocean responses by permitting a range of delay times between the cumulative wind forcing and apparent response. Once we solve for the expected inertial amplitude, U_s with h_o as 10m. The response of the slab with prescribed depth, then any slab response with a new depth, h_s, will have a response proportional to $\frac{h_o}{h_s}$. Initially, we also allowed the slab bottom interface friction decay constant, r, to vary as well, which altered both the phase and amplitude of U_s, but the effects and subsequent accuracy were negligible compared with any reasonable amount of time lag. The weighting function, $w(L)$, limits the

time-constraint for the cost function such that behavior near the time of concern holds more predictive import than times further removed where everything further than 36 hours from the analysis time thrown out. Thus by finding the minimum of the cost function, we estimate the most likely slab depth.

3.4 Calibration

In order to accurately predict the MLD with the SLIM algorithm, we use the observed glider profiles to develop a correction factor that yields the most predictive power. Using processed data from the IOOS Underwater Glider DAC from 2013 and 2014 where each profile is separately tagged with a geographic location and time, we calibrated and tested the model parameters from 123,000 separate profiles for fitting the mixed layer to the slab-model of the ocean in the near-inertial band. The training is sensitive to the choice of definition of MLD. We tested the biological mixed layer defined at the maximum buoyancy frequency, D_{N2}, used by Carvalho et al. (2017) to assess biological productivity, and a momentum transfer mixed layer defined by temperature difference from the mean temperature of the upper 10m of the water column, $D_{\Delta T}$ used by Evans et al. (2018) to observe turbulent cascades. In open-ocean studies (e.g. Kara et al. (2000)) the difference between D_{N2} and $D_{\Delta T}$ proved to be marginal, but attempting to predict the depth which feels the bulk of the momentum transfer correlates most with the homogeneous waters identified by $D_{\Delta T}$, which we find is often shallower than D_{N2} in the aftermath of storm events.

Following Dohan, Davis (2011) and chapter 2, we observe that often during certain storm events the strong seasonal pycnocline in the MAB broadens and the upper ocean becomes slightly stratified as the mixing mechanism is driven by shear across the pycnocline, rather than surface forcing. Following storms where this occurs, new ocean surface boundary layers can form from lighter winds and incoming solar, short-wave radiative forcing that are strong enough to meet our $D_{\Delta T}$ criterion, where

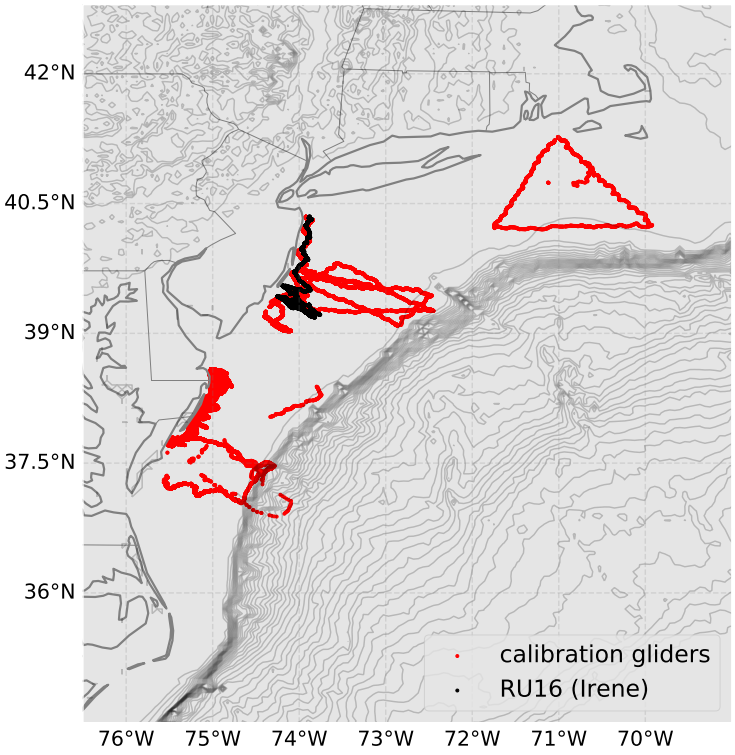

Figure 3.1: Autonomous underwater vehicle, glider, flight tracks used for calibration during the Summer and Autumn of 2013 and 2014 are shown in red along the Mid-Atlantic Bight. The flight track of RU16, to the east of New Jersey, is also shown in black

$\Delta T \geq 0.25$°C, even as the D_{N2} stays deep as shown in Fig. 3.2. Thus, the effective slab that feels the transfer of momentum from the atmosphere to ocean is chosen to be the shallow ocean surface boundary layer and a better measure of what the SLIM algorithm is attempting to find.

Then in order to calculate the full SLIM predicted MLD, we need to assess the correlation of the theoretical slab and observed NIC. Moreover, the HFR NIC data will have inherent differences from theoretical slab response due to spreading of frequencies in a real ocean, excitation of the bottom due to coastal interaction as described by Shearman (2005b), and data processing inherent in the spatial and time averaging of the HFR raw data (Roarty et al. 2010). To account for this we apply an effective

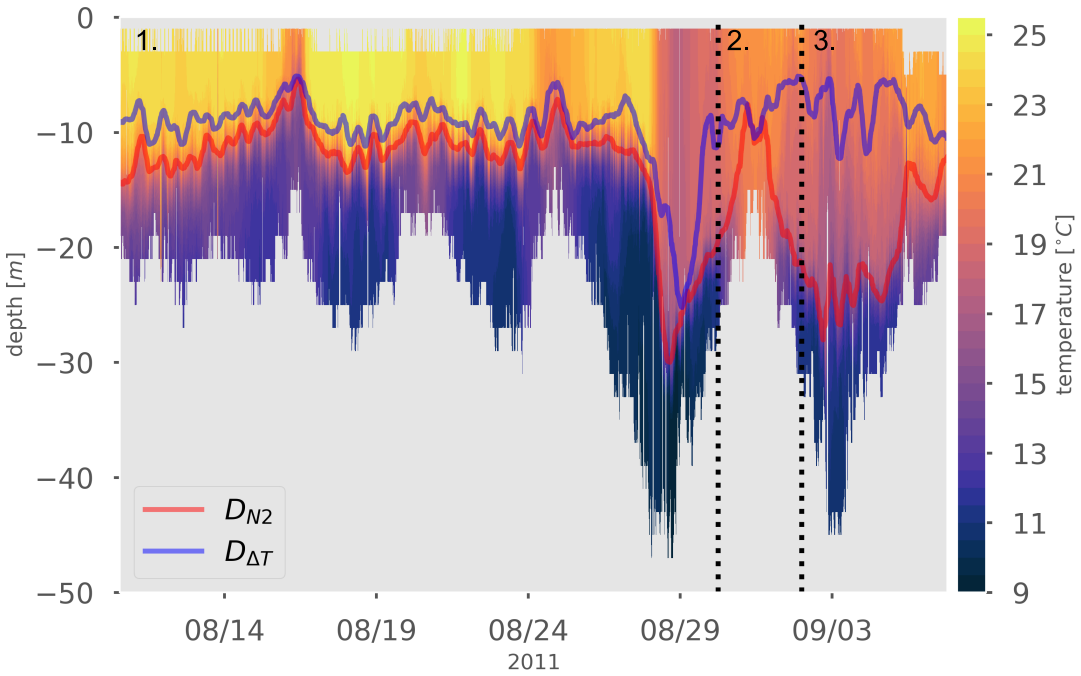

Figure 3.2: Defining the mixed layer depth from glider CTD profiles, using RU16 as the example. D_{N2} (red) is based on the maximum N^2, and $D_{\Delta T}$ (blue) is based on the temperature change. The glider transect is broken into three parts: 1) seasonally stratified waters, 2) single-layer ocean due to mixing and glider moving inshore, and 3) the formation of a new ocean surface boundary layer. During the strongly stratified period and during the rapid mixing of Hurricane Irene, up to 8/29, the two definitions are similar.

gain, c, on the U_{hfr} by

$$J_c(h_s, L, t_i) = \sum_{t\pm 1.5 \text{ days}} w(t_i, t) \left| cU_{\text{hfr}}(t) - \frac{U_s(t-L)h_o}{h_g} \right|, \tag{3.5}$$

where h_g is the observed MLD using *in situ* glider measurements. Then by the dividing the gain-adjusted cost function, J_c by c in equation 3.5, we arrive at a solution where the U_{hfr} is balanced by $\frac{U_s(t-L)h_o}{ch_s}$ in the gained cost function, implying a corresponding linear relationship between observed mixed layer depth and prediction, $ch_g = h_s$. Then using a least squares linear regression, we calculated the value of the gain coefficient, $c = 3.31$, by minimizing the error between $D_{\Delta T}$ and h_s as predicted by the non-gained cost function for the gliders in 2013 and 2014. From this, we can compare the predictions of SLIM with observed mixed layer depths during 2013 and 2014 as show in a two-dimensional histogram in Fig 3.3, where the black line shows

a perfect one-to-one correlation. In Fig 3.3 we can observe the skill of SLIM as well as the preponderance of shallow summer mixed layers observed by the gliders.

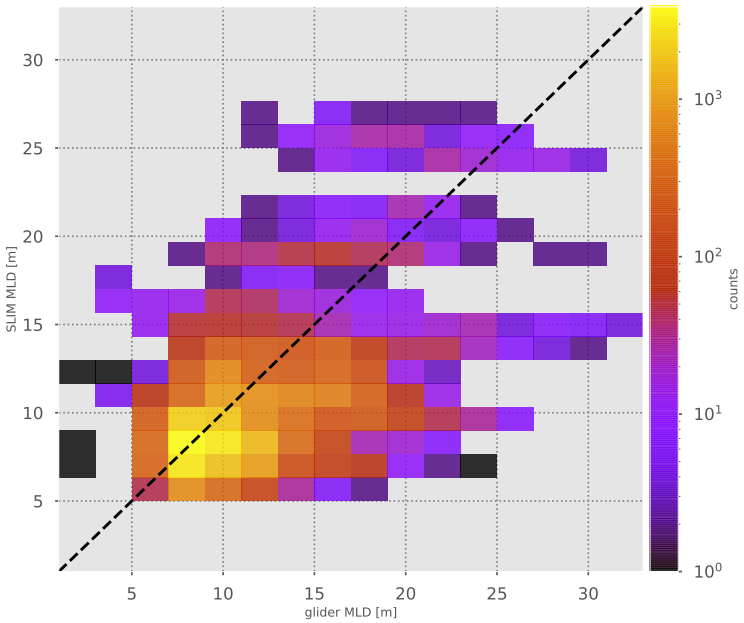

Figure 3.3: Two-dimensional histogram of the correlation between SLIM and glider mixed layer depths where the black dashed line shows the one-to-one line.

During calibration we observed that there was no correlation between lag time and SLIM accuracy, but there was a small onshore-offshore bias to the output that may be mitigated by a more complex algorithm. We ran SLIM with 5%, 10%, and 20% NIC filter widths and the 10% filter offered the minimum error compared to other NIC bandpass filters in the SLIM algorithm using the cost function (Eq. 3.4).

3.5 Case Study: Hurricane Irene (2011)

Strong tropical and subtropical storms, which directly impact the breakdown of the cold pool, induce shelf-scale pressure gradients that induce both mixing and advection of Cold Pool water (Austin, Lentz 2002; Glenn et al. 2013). As 2011 was not used in the calibration of the gain coefficient, we can verify the results using the transect from RU16, a glider deployed ahead of Hurricane Irene, which rapidly transited through the MAB and made landfall in New Jersey. We show in Fig. 3.4 that after withholding

the period of single-layer behavior immediately after the storm, we find a relatively tight fit between the observed MLD and the predicted.

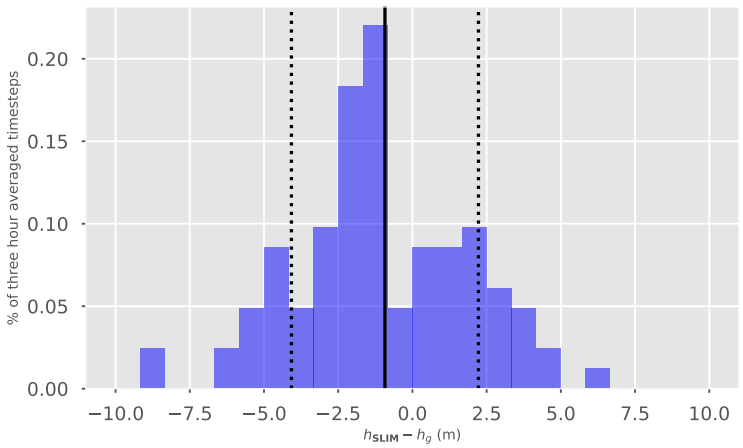

Figure 3.4: Histogram of the offset between h_g measured in sections 1 and 3 of the RU16 glider transect in 2011, and h_s derived from SLIM with the gain calibrated in 2013 and 2014. The mean error is 1.0m and the standard deviation is 3.8m. RU16 location in figure 1 (black line) is located 10-80 km east of New Jersey.

In Fig. 3.5, the SLIM algorithm shows the comparison between the predicted MLD from SLIM and with the autonomous underwater glider, RU16, during the mixing from Hurricane Irene. Accounting for the movement of the glider, we obtained the SLIM-predicted MLD by a spatial averaging of the nine model outputs nearest to the glider at each time point during eye-passage, accordingly the lightly shaded area around the white line in figure 3.5 is the standard deviation around that average for those nine points. Hurricane Irene produced downwelling-favorable ahead-of-eye winds over the MAB that initially had a shallow, $O(10m)$, MLD with a strong mid-water pycnocline, which rapidly mixed during the high winds of the storm. The mixing and cooling of the surface waters ahead-of-eye changed the physical dynamics at the atmospheric boundary layer, changing the sign of the heat transfer and resulting in the rapid weakening of Irene from a potential category 3 hurricane to make landfall as a tropical storm at landfall (Glenn et al. 2016). Now that we have verified the SLIM MLD with a single time series of *in situ* data, what is the spatial response to the hurricane across the MAB?

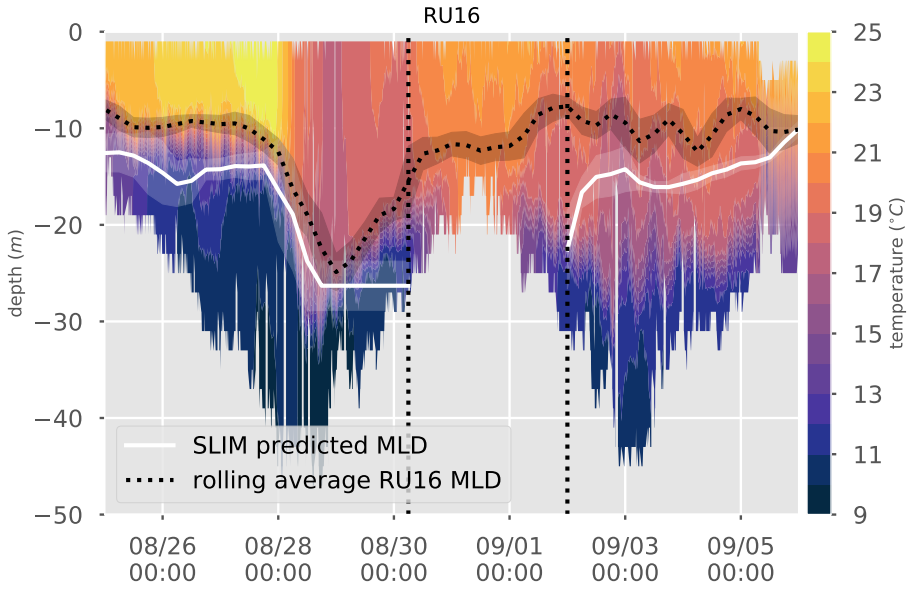

Figure 3.5: Comparing the rolling average of D_{N2} and the SLIM predicted mixed layer during the phases of the storm without bottom attachment in more than 3/9 of the spatially averaged SLIM outputs (sections 1 and 3 of the transect).

Observations of the pycnocline and mixed layer are sparse, thus a technique with the capacity of the SLIM to estimate changes in the ocean dynamics at synoptic timescales allow for a higher spatial and temporal resolution. Indeed, in accord with the vertical mixing seen shelf-wide ahead of the storm in Fig. **??**, National Data Buoy Center data recorded that by the time in the storm trajectory that Irene's peak wind speeds were observed, water temperatures had already dropped between approximately 4 and 6 degrees Celsius more than 150 km ahead of the eye of the hurricane (Seroka et al. 2016). Due to the nature of the two-layer system in the MAB, deepening of the thermocline is correlated with the mixing of the cooler waters from beneath the thermocline into the upper ocean boundary layer. Hence, the observed deepening in SLIM is in sync with the observations of sea surface temperature change in scenarios where the dominant process is mixing. Having the ability to remotely observe and parse the essential ocean variables involved in the mixing and entrainment of cooler water to the surface from the ahead-of-eye winds where the conditions of tropical cyclones inhibit more traditional forms of measurement, allows for nuanced

understanding of the role of the coastal ocean in controlling near-shore intensity.

Using the SLIM algorithm, we observe the entire life cycle of the mixed layer before, during, and recovering after Hurricane Irene (Fig. 3.6). A key point to note is that from stable MAB-wide stratification before the storm on 8/26 12:00PM to equivalently stable conditions post storm on 9/4 12:00PM requires only little more than a week despite the large wind and thermal forcing of Hurricane Irene. The re-emergence of the ocean surface boundary layer seen in the glider transect informs the spatial response as the amount of time for solar heating and light winds to generate a new surface mixed layer.

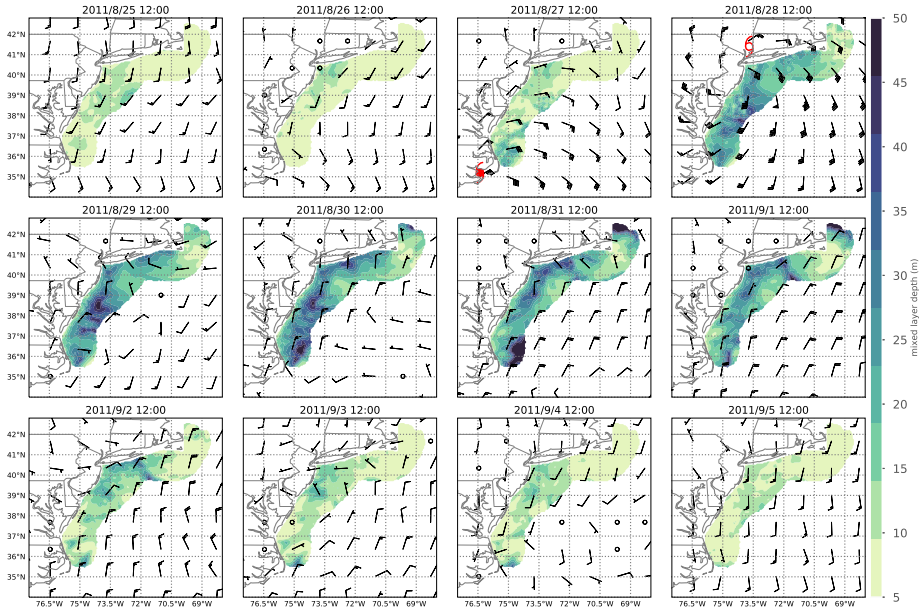

Figure 3.6: The full life cycle of a late-Summer/early-Fall mixed layer in response to tropical storm forcing reveals that the shallow stratification returns across the region within a week of the event, despite a much lower sea surface temperature.

3.6 Seasonal Dynamics

Wind stress, both seasonal and during storm events, plays an important role in the timing of biological events and cycles through the development of stratification and destratification via both turbulent mixing and shelf-wide circulation (Austin, Lentz

2002; Xu et al. 2013; Seroka et al. 2016; Miles et al. 2017). By remotely observing the MLD on shelf-wide scales at high temporal resolution, we can illuminate the dominant physical parameters and gain further understanding of the physical processes governing stratification in the MAB. In Fig. 3.7, we show how uniform summer stratification across the entire MAB driven by the seasonal cycle of incoming short-wave, solar radiation persists through the sparse summer storms. Large storms such as Hurricane Irene only disrupts the regional pattern of surface boundary layer depth for timescales on the order of a week. Following the summer into autumn, beginning with Hurricane Irene, we observe a succession of storms moving over the MAB with enough energy to alter the mixed-layer eventually leading to the stratification no longer being able to recover.

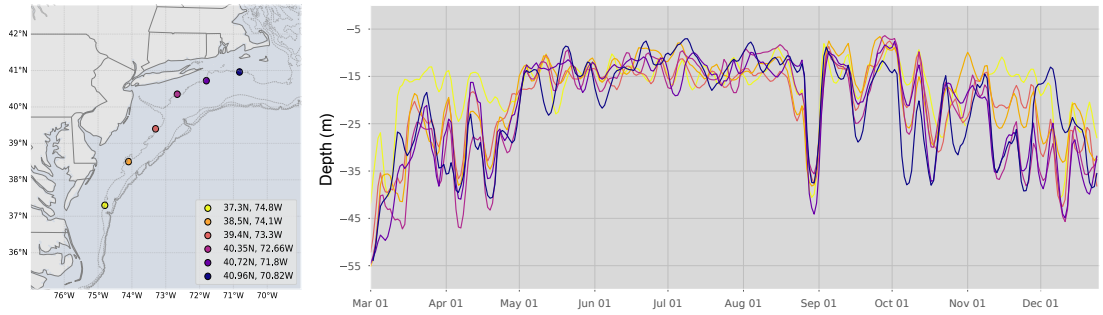

Figure 3.7: The spatial variability of the mixed layer over the 2011 seasonal cycle shows by six points along the 50m isobath. The feature of note is the strong Summer stratification leads to spatial coherence of the MAB from May to September. The recovery of the shallow mixed layer after Hurricane Irene, signifies a large amount of potential energy lost, and the subsequent storms erode the spatial coherence until the two-layer model loses predictive in mid-December.

In observing the seasonal transition from the strong stratification of Summer MAB to the more uniform winter conditions, SLIM shows that the standard deviation of the predicted MLD increases from June to October for each of the points in Fig. 3.7. Further study looking at the change in sea surface temperatures associated with the storm mixing and the maps of SLIM-predicted mixed layer depth is needed to understand the heat flux in the coastal ocean during the fall transition and the relative

importance of the synoptic-scale wind events as the MAB mixes and entrains cooler water to the surface.

3.7 Discussion

The requirement of in-situ density or temperature profiles to determine the MLD severely limits our mixed-layer estimates to available CTD profiles globally. Primary production in the MAB is sustained by nutrients which originate from the off-shelf waters that enter through the NE channel in the Gulf of Maine and between Brownes Bank and the eastern Scotian shelf dominated by two periods of high productivity in the Spring and Fall, concurrent with changes in the MLD (Bigelow 1933; Marra et al. 1990; Friedland et al. 2015). Thus the problem of predicting and understanding biological processes is exacerbated in coastal oceans where changes in the MLD occur rapidly (Walsh et al. 1988; Fernández, Pingree 1996; Shroyer et al. 2014). In addition to the biological component, the rapid changes in the MLD alter the air-sea interactions during tropical storms and effect near-shore intensity predictions (Glenn et al. 2016; Seroka et al. 2016; Potter et al. 2019).

We show that after Hurricane Irene, new mixed-layers are formed to a steady state of approximately 15m, which are as shown in the RU16 transect often weaker stratification than the deep pycnocline, and then subsequent storms can more easily mix those weaker ocean surface boundary layers down until they reach the depth of Irene's mixing. This process of stochastic, storm track dependent mixing agrees with fall transition dynamics proposed by Lentz (2008). However, the main difference with previous research is that each storm does not mix the mixed layer deeper for longer than a week early in the fall transition. Rather each storm leads to a deepening event dependent on storm track until the system can no longer return to equilibrium. Thus, the leading indicator of fall transition is the variance of the MLD. The variance of MLD in August and to a lesser extent September for all points along the MAB is

dominated by Hurricane Irene. But afterward, SLIM shows the variance increases with the fall storms in September and October, led by the Northern-most point, leading to a mean deepening in October to November.

3.8 Conclusion

In this paper, we show the capability and value of using HF-radar to remotely sense the oceanic mixed layer depth. The mixed layer represents the interface of the ocean with the atmosphere, the euphotic zone near the surface, and the deeper nutrient rich waters below (Taylor, Ferrari 2011). In 1970 Pollard and Millard proposed a simple two-layer slab model of for the inertial response of the mixed layer to wind forcing (Pollard, Millard 1970a; Pollard 1970). Using HF-radar to measure the near-inertial currents and North American Regional Reanalysis 10-meter winds, we developed the SLIM as an inverse problem to find the MLD, where the slab response most closely matched the observed ocean. Then using the abundance of autonomous underwater vehicles in the region, we tuned the model parameters to minimize the error between *in situ* and predicted MLDs. The goal of this research was to understand both the synoptic and the seasonal trends in MLD in the MAB. By remotely sensing the MLD with HF-radar, we were able to get near-continuous and spatially coherent data over the entire shelf. As a pertinent example, we show the rapid deepening of the MLD before eye-passage of Hurricane Irene, matching previous studies and illuminating the role of mixing in the rapid de-intensification of the tropical cyclone (Seroka et al. 2016). In addition to the observations already known from *in situ* AUVs, we illustrate how the changes in MLD progressed from South to North ahead of the storm, showing that Hurricane Irene traveled over an ocean that was already mixed by the leading edge of strong winds. The rapid recovery (week) of the shallow stratified surface layer and the seasonal time series show that dependence on synoptic events in mixing even as the incoming solar radiation is enough to keep the MAB stratified between

storm events. The rapid, shelf-wide behavior of the mixed layer reveals previously unseen elements of re-stratification and further how the MLD behaves over the entire region during the fall breakdown of the MAB cold pool.

Chapter 4

Intercomparison of Mid-Atlantic Response to Tropical Cyclones

4.1 Introduction

Tropical cyclones represent one of nature's greatest threats to life and property (Smith, Katz 2013) due to a combination of wind (Keim et al. 2007), heavy rains (Zhang et al. 2018b), and storm surge (Fritz et al. 2007). As hurricane track prediction skill has increased over the last decades, however intensity in the region near landfall remains an area of enhanced error (Cangialosi, Franklin 2012), thus the communication of risk to the public remains a discrete challenge in the field. Reducing loss of life and harm while maintaining public trust in the information when a hurricane threatens depends on people receiving hurricane risk information that they can interpret and use that doesn't lead to excessive over- or under-reaction (Demuth et al. 2012). Thus to understand and improve hurricane risk communication in the Mid Atlantic Region we ask the question: is there a framework for understanding the interaction of the shallow coastal ocean with tropical cyclones from which first-order predictions can be made?

The Mid Atlantic Bight (MAB) is a coastal ocean in the North Atlantic Ocean on the continental shelf from between Cape Hatteras in the South and the Gulf of Maine or the Nantucket Shoals in the North (Mountain 2003a). There is large seasonal variability on the MAB in regards to temperature, where "cold pool" is the name for the strong stable stratification of the thermocline and pycnocline (Houghton et al. 1982). The cold pool water column is a variable, bottom-trapped, cold water mass of

remnant local and remote winter water found during summer over the mid and outer continental shelf in the MAB. Simultaneously at the surface a warm, fresh mixed layer develops in the Spring and Summer as incoming solar radiation and seasonally light winds build strong stratification, $N^2 \sim \mathcal{O}(10^{-3})$ (Mountain 2003a). Once formed, this distinctive cold pool goes through a complex evolution during the rest of the spring/summer, such that during May-June, there is a continued westward inflow of some of the coldest water with Gulf of Maine (GoM) origins and the cold pool is warmed by turbulent heat flux from above (Chen et al. 2018). Additionally, the salinity of the cold pool is altered by salt fluxes through a series of more episodic exchanges through its lateral boundaries (Wallace et al. 2018). So while minimum MAB cold pool temperatures are observed well into July, the competing processes that cause a general warming are not enough to remove the near-surface reservoir of cold water during the North Atlantic hurricane season.

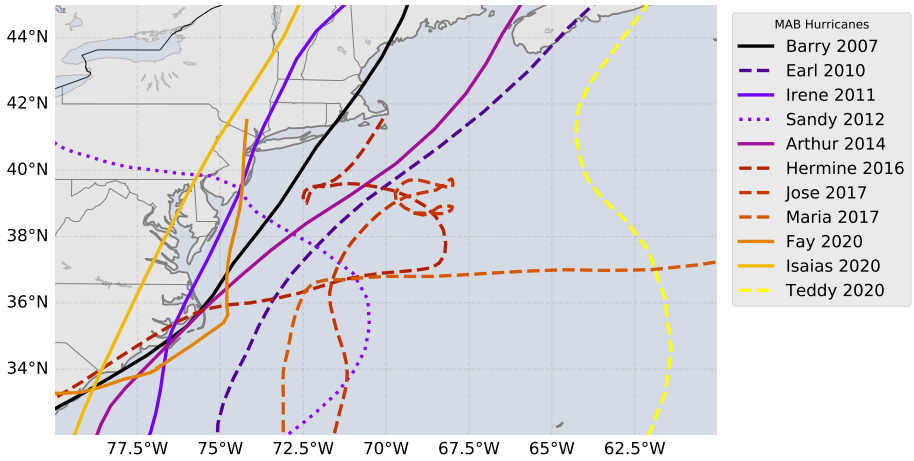

Figure 4.1: Hurricane tracks from NOAA International Best Track Archive for Climate Stewardship (IBTrACS) in the Mid Atlantic observed using RUCOOL resources. The tracks are delineated such that the dashed lines represent offshore, the solid lines represent coastal tracks, and the dotted line represents Hurricane Sandy, which displayed characteristics of both due to crossing the shelf approximately perpendicular to the coastline.

Thus during tropical cyclones, the rapid co-evolution of the ocean-atmosphere system in the shallow waters of the MAB can alter the intensity of the storm as the

surface fluxes respond to rapidly changing sea surface temperature (SST) (e.g. Glenn et al. (2016); Seroka et al. (2016)). Coupled atmosphere–ocean models demonstrate that small shifts in SST even on horizontal scales similar to MAB, can greatly alter storm intensity (Emanuel 2003; Schade, Emanuel 1999). The effects of mixing (e.g. Rudzin et al. (2017)) and mesoscale SST features (e.g. Shay et al. (2000); Jaimes, Shay (2009)) on hurricane intensity have been studied in the open ocean. Recent studies centered in the MAB have looked at coastal ocean response to tropical storms to include direct wind-driven mixing from Hurricane Irene (e.g. Seroka et al. (2016); Glenn et al. (2016)), baroclinic inertial shear (e.g. Zhang et al. (2018a)), and downwelling front driven by Ekman dynamics (e.g. Miles et al. (2017)).

In response for the need to understand the interplay of the coastal ocean with tropical cyclones, the Rutgers University Center for Ocean Observing Leadership (RUCOOL) in conjunction with Mid-Atlantic Regional Association Coastal Ocean Observing System (MARACOOS) have deployed autonomous underwater gliders during tropical systems since 2007. The tracks of the tropical cyclones observed using *in situ* measurements by RUCOOL are shown in Fig. 4.1, where a glider was deployed to observe the entire water column for all but Fay (2020). The ability for autonomous gliders to operate in these storm-tossed shallow water environments has opened up a window into the processes and dynamics of the atmosphere-ocean coupled system. By comparing the strength of the storms, the tracks of the storms, and the observed ocean response, we can delineate a matrix of possible storm types and from that develop a framework for predicting both the ocean and atmospheric response.

4.2 Data

Observation of the coastal ocean required the *in situ* measurements made possible by Teledyne-Webb Research Slocum glider profiles available from the MARACOOS

and the Integrated Ocean Observing System (IOOS) Glider Data Assembly Cyberinfrastructure. Gliders are autonomous underwater vehicles (AUVs) that have become useful platforms for monitoring the ocean's response to storms (Testor et al. 2019; Domingues et al. 2019). Gliders can profile the water column from the surface to depths of up to 1000m and continuously sample every two seconds to provide a high temporal resolution time series. For the storms in 2020, we also used the floating LIDAR buoy deployed by Atlantic Shores Offshore Wind (ASOW) (39.272° N, 73.889° W) to have co-spatial and contemporaneous current from an acoustic Doppler current profiler (ADCP) that measures speed and direction at meter intervals from 3-36m depth, seawater temperature at 1m depth, and wind speed and direction at 10-250m altitude. Meteorological observations were obtained from NOAA NDBC buoys 44009 (38.461° N, 74.703° W) and 44065 (40.369° N, 73.703° W) included wind speed and direction measured at a height of 5m, air temperature at a height of 4m and ocean temperatures at 0.6m depth. The Tuckerton WeatherFlow Inc. meteorological tower (39.52° N, and 74.32° W) measured wind speed and direction at 12m. Coastal ocean three-dimensional (3D) model simulations of the MAB under Isaias were made using the operational Regional Ocean Modeling System (ROMS) DOPPIO model (López et al. 2020).

In order to assess the spatial component of ocean-atmosphere interaction (Cornillon et al. 1987), we acquired National Oceanographic and Atmospheric Administration (NOAA) Advanced Very High-Resolution Radiometer (AVHRR) satellite data using the SeaSpace TeraScan L-Band satellite ground stations at Rutgers and the University of Delaware and publicly distributed through the Rutgers website. The multichannel SST algorithm converted the AVHRR data to usable SST (McClain et al. 1985). Raw AVHRR data is continuously processed via standard multi-channel algorithms with standard cloud flagging algorithms applied and posted online (https://marine.rutgers.ed
with details described on the website.

Another spatially relavent data set is the regional MARACOOS high-frequency

radar (HFR) network consisting of over 40 radars (Roarty et al. 2020). From this HFR network, we utilize the 6km resolution data product of the surface currents within 250 km of the coast, which covers the region where the strong seasonal pycnocline develops.

4.3 Basic Ocean Responses

Shelf-wide ocean responses to the strong forcing of a tropical cyclone come in four main essential ocean processes. The first is direct turbulent mixing during the periods of peak winds (e.g. chapter 2). Second is the shear across the pycnocline due to inertial energy deposited by the storm (e.g. Shearman (2005a); Zhang et al. (2018a), Chapter 3). Third and fourth are distinct, but connected via similar timescales and underlying Ekman dynamics that generate coastal downwelling explored in Miles et al. (2017) and upwelling frontal dynamics in this thesis.

Direct wind mixing has been extensively studied in the mixing of the pycnocline and deepening of the ocean surface boundary layer (OSBL) such that cooler, denser waters are entrained into the surface (Kraus, Turner 1967; Pollard et al. 1973; Trowbridge 1992; Dohan, Davis 2011). In addition multiple process studies have shown that many intermediary processes are important in the exact quantity of mixing, such as background internal waves (Price et al. 1986), the nonlocal response of the surface-forced boundary layer (Large et al. 1994a), shear throughout the OSBL (Mellor, Yamada 1982), large-aspect ratio coherent structures in the OSBL due to turbulent Ekman flow (Skyllingstad et al. 2017a), and coherent Langmuir structures related to surface wave dynamics (Belcher et al. 2012). These processes are important to a full physical understanding of the spatial and temporal extent of mixing, the first order extent of mixing is dependent on conventional friction velocity scaling of the turbulent kinetic energy and entrainment illustrated in Fig 2.16.

The Wind-driven near-inertial currents are a common feature of the mid-latitude,

Name (yr)	Ahead-of-eye change in temperature (degC) Glider, 44065, 44009	24hr after-eye change in temperature (degC) Glider, 44065, 44009	Pycnocline Strength (max N2)	Change in Pycnocline depth (m)	Pycnocline width ahead of eye (m)	Pycnocline width at eye-passage (m)	Pycnocline width 12hrs later (m)
Barry (2007)	-1.3, ND, -0.9	0.8, ND, 0.5	0.0015	-6.9	2.0	5.1	2.1
Irene (2011)	-4.4, -3.6, -3.5	-1.5, -0.3, -0.7	0.0034	-12.7	1.4	2.7	3.7
Arthur (2014)	0.3, ND, -0.2	-1.6, ND, -2.1	0.0033	-7.6	2.6	7.1	2.4
Fay (2020)	-3.4, -3.2, ND	0.9, -0.3, ND	n/a	-8.5	2.1	3.0	4.8
Isaias (2020)	-0.1, -7.8, ND	-0.5, -0.5, ND	0.0021	-5.0	3.4	3.9	6.2
Sandy (2012)	-2.1, -0.8, -0.5	-1.0, 0.2, -0.2	0.0012	∼-12 (fully mixed)	2.3	n/a (fully mixed)	n/a (fully mixed)

Table 4.1: The ocean responses to storms with distinct wind patterns to indicate the effects of eye-passage to include cooling of the surface ocean, deepening of the pycnocline, and width of the pycnocline.

upper-ocean due to the effects of seasonal stratification and Coriolis forces (Pollard 1970; Pollard, Millard 1970a). However as the inertial currents are formed and when they interact with the coastal wall, the properties of the current structure and shearing change (Shearman 2005a; Zhang et al. 2018a). In cases where the inertial currents are created near land, the inertial currents are reflected off the coast so as to energize the bottom layer and lead to a near-inertial response in the Cold Pool at an offset phase so as to lead to enhanced shear at the pycnocline. Shearing across a stratified pycnocline is a robust area of study (e.g. Kaminski, Smyth (2019)), and when it meets the criteria of shear to stability leading to overturning instabilities, turbulent mixing, and broadening of the pycnocline (Miles 1961; Smyth, Moum 2000; Smyth 2003; Smyth, Moum 2012).

Upwelling and downwelling fronts occur due to partitioning of the shelf into dynamically different regions with and without stratification. The steady far-field winds of a tropical storm can develop full Ekman transport in the region offshore of the upwelling or downwelling front because it can interact with the bottom boundary layer in the relatively shallow water (Austin, Lentz 2002). Onshore of the front, the coastal ocean is effectively a single layer with weak stratification and the surface and bottom Ekman layers typically interact. Austin, Lentz (2002) described this dynamic in a two dimensional idealized manner governed by the presence of a along-shore winds that drive Ekman flows that lead to development of the cross-shelf circulation, which redistributes the density field into a strong horizontal gradient at the surface/bottom

boundary for the upwelling/downwelling favorable winds respectively. Importantly, the location of the front is, as confirmed in Miles et al. (2017), predicted by the simple linear relation between wind stress, τ^s, and horizontal displacement, ΔX, of the front by the formula

$$\Delta X = \int_0^t dt \frac{\tau^s(t)}{\rho_o f D}, \tag{4.1}$$

where f is the Coriolis acceleration, ρ_o is the density of the OSBL, and D is the mixed layer depth.

4.4 Typology of Storms

The key to this study lies in the variability of the storm tracks shown in Fig. 4.1, as it represents a wide cross-section of possibilities ranging from inshore with Isaias (2020) to far offshore with Teddy (2020). We break these storms into three main types of tracks: 1) inshore storm, where the eye remains over land, 2) coastal storms, where the storms cross the MAB and generally travel in a Northward to Northwestern direction up the coast, and 3) the offshore storms, where the tropical cyclone generates the response due to far-field winds as the storms are off the shelf.

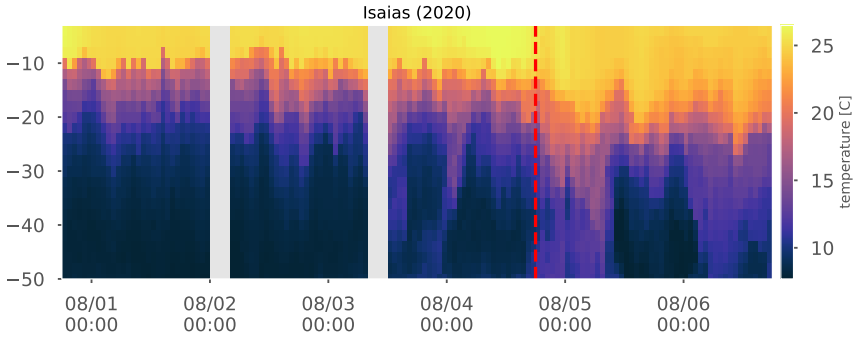

Figure 4.2: Glider observations of water temperature during Tropical Storm Isaias (2020), where the eye-passage is marked by the dashed red line.

In table 4.1, the ocean responses to eye passage are shown for the inshore storms, coastal storms, and Hurricane Sandy (2012). For offshore storms not included in table 4.1, the MAB response is not dictated by eye-passage. The change in wind direction

during the cross-shelf track of Sandy represents an oddity in this framework, as shown in Fig. 4.1, as it started offshore and developed the MAB coastal ocean in a way that mimics the offshore paradigm and then later crossed the shelf to make landfall. Therefore, Sandy is included in table 4.1 due to the distinct eye-passage that was sensed at the NDBC buoys.

4.4.1 Inshore Storms

Perhaps the most glaring discrepancy in table 4.1 is the amount of cooling ahead-of-eye observed in Tropical Storm Isaias (2020) by buoy 44065 compared with the glider observation, as shown in Fig 4.2. For the inshore Isaias and with the glider located in the mid-shelf, the depth of the pycnocline and temperature of the surface remain relatively constant. In comparison, the 44065 data buoy is located in the near-shore region close to New York Harbor and observes significant ahead-of-eye cooling of 7.8 °C.

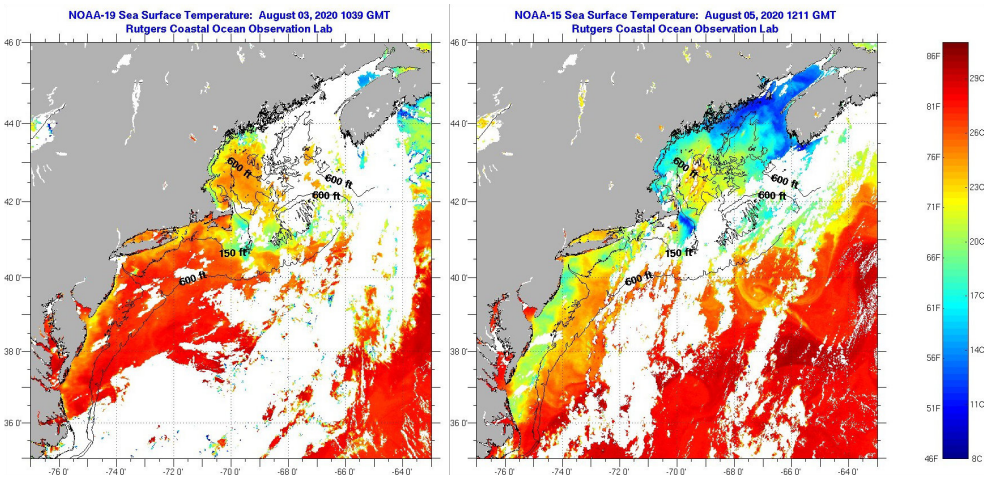

Figure 4.3: NOAA satellite SST from before and after the passage of Isaias, a preponderance of near-shore cooling consistent with a large upwelling event.

The spatial pattern of inshore cooling and offshore stasis is indicative of the Ekman-driven upwelling dynamics proposed in Austin, Lentz (2002). Then using NOAA satellite SST, as shown in Fig. 4.3, from before and after the full storm passage a clear upwelling front with some overall cooling across the MAB is observed.

In the idealized two dimensional case described in Austin, Lentz (2002), the location of the observed upwelling front can be predicted from Eqn. 4.1. By integrating the τ^s from ASOW buoy wind observations and using the pycnocline depth from the glider section, D, the approximate displacement should be $\mathcal{O}(50km)$, which matches the satellite observations and the cross shelf flows modeled by ROMS in Figs. 4.5 and 4.4. Additionally in Fig. 4.4.c, we show in the 3D model runs of DOPPIO that the cooling in the near shore is linked to the cross-shore velocities where the steady winds ahead of eye generate order 1 m/s offshore currents in the surface. Thus, in panels a-c of Fig. 4.4, the 22C isotherm is tracked, showing a 60km movement from the coast to the mid-shelf ahead of eye passage in the model. Further by comparing the SST with the glider temperature section, we observe the entrainment of cooler waters, deepening of the pycnocline, and surface cooling occur in the period after eye passage, indicating that the shelf-wide SST cooling observed in Fig. 4.3 outside of the upwelling front is likely the result of the after-eye processes. Additionally during the mixing and deepening phase after-eye, the pycnocline broadens, which indicates the presence of a baroclinic shear across the pycnocline leading to instability-driven entrainment. The exact nature and source of the shear is challenging to find, but does not match with the two dimensional upwelling front structure. Rather, a likely candidates for the shearing are the storm-generated near-inertial currents observed by the regional HFR network.

4.4.2 Coastal Storms

The bulk of the storms on table 4.1 represent the coastal track dynamics with Barry (2007), Irene (2011), Arthur (2014), and Fay (2020). As seen in the map in Fig. 4.1, the coastal track is varied, but is denoted by moving south to north over the shelf-seas of the MAB. Thus, the essential processes that govern the ocean response are reactions to similar atmospheric forcing where the MAB feels the distinct phases of ahead-of-eye winds, rapid rotation of winds during eye-passage, and the return of

steady winds after eye. In order to focus in on the key features of the co-evolution of the ocean-atmospheric system in the MAB, this study looks at the similarities and differences in the ocean response between Irene and Arthur. Where as the gliders underneath both storms were located within 30km of eye-passage, the temperature profiles observed in Fig. 4.6 illustrate how Irene, as the more intense storm with stronger winds, was able to mix the pycnocline and entrain dense, cold waters to the surface in comparison to the relatively steady pycnocline and minimal surface cooling in Arthur. In large eddy simulations of the ocean dynamics under Irene, chapter 2 demonstrated that wind forcing, through large aspect-ratio structures, generate enough entrainment to directly mix the pycnocline deeper and bring up cooler waters to the surface. In contrast, Zhang et al. (2018a) illustrated that the direct mixing phase of Arthur was minimal by using a regional ocean model, agreeing with the glider observations.

Starting with Irene, Fig. 4.6.a shows the rapid cooling where the direct mixing leads to turbulent entrainment of abundant cold bottom water. The resulting ocean cooling, as seen in Fig. 4.7, reduced surface heat flux to the atmosphere leading to the rapid weakening described in Seroka et al. (2016). The strong surface winds continued for hours after eye passage and the strong winds in the after-eye phase of the storm. However as shown in chapter 2, the transition due to the rapid rotation of winds during eye-passage led transition in the OSBL from shearing being spread evenly by the large aspect-ratio to the dominance of inertial energy leading to shear becoming concentrated at the pycnocline and subsequent broadening of the pycnocline as shown in Fig. 4.8.

Tropical Storm Arthur was weaker than Irene (Fig. 4.10) during the period of ahead-of-eye mixing, which led to the negligible mixing seen in the glider profile of temperature in Fig. 4.6.b. This led to minimal change in SST as shown across the MAB in Fig. 4.9. Arthur's track (Fig. 4.1 led it offshore rapidly after crossing the glider, which led to upwelling favorable far-field winds and slight near shore

cooling observed in Fig. 4.9. There was some cooling in the bulk MAB observed in the SST, but from the buoys and gliders we can assess that most of this cooling occurs after eye-passage and will have minimal effect on storm strength unlike the rapid cooling associated with Irene. Thus, the ability of a rapid co-evolution of the ocean-atmospheric system is dependent on the strength of the incoming storm and stratification of the MAB. Tropical Storm Fay (2020), much like Arthur occurred early in the season when the surface temperature is lower and net stratification is weaker than during the late Summer like Irene. However the shear profiles presented in Fig. 4.11 show the similar two-stage behavior as Irene, where eye-passage disrupts the tight-pycnocline, wind-induced shearing that transitions with eye passage to a mixed layer dominated by near-inertial energy indicated by observations of diffusion and widening of the pycnocline.

4.4.3 Offshore Storms

Offshore storms, unlike onshore and coastal storms, force the ocean mainly with far-field winds. Due to the geometry of the MAB coastline, the far-field winds funnel into an along-shore direction from North to South on the Western side of the storm. This leads to prolonged periods of downwelling favorable conditions, opposite in direction but similar in character to the onshore dynamics explored with Isaias. For the offshore storm, the downwelling favorable winds act to turn the steep vertical density gradient into a bottom-attached horizontal density gradient where the warmer nearshore waters are advected across the shelf slope. As such, the gliders in Fig. 4.13 show for each of the storms a warming of the bottom waters indicative of the frontal displacement. Hurricane Sandy (2012) and Tropical Storm Hermine (2016), both show that the deepening of the warm, surface layer as the colder waters are pushed offshore occurs well before the nearest eye-passage. For Tropical Storm Teddy (2020), Fig. 4.13.c, the far-field winds are less obviously tied to eye-location as Teddy remained much further offshore as shown in Fig. 4.1, which leads to other physical processes

such as the influence of the extra-tropical transition that extends the wind field in the mid-latitudes.

As the downwelling favorable winds in offshore storms generate flow akin to the idealized model of Austin, Lentz (2002), the change in surface temperature and corresponding co-evolution on tropical cyclone intensity is marginal. Using Hermine as an example, shown with satellite SSTs in Fig. 4.12, the change in surface temperatures within the MAB are minimal despite the long period of cloud cover due to Hermine's slow translation speed and storm track. Indeed in the coupled ocean-atmospheric models run for Sandy, he sensitivity of tropical cyclone intensity to using before sst, after sst or evolving sst is small, but the the impact of the sst may still be important to include (Miles et al. 2017).

4.5 Discussion

The observed and modeled coastal ocean couples with the atmosphere and co-evolves during tropical cyclones in multiple and complex ways from coherent structures (e.g. Sundermeyer et al. (2014); Skyllingstad et al. (2017b)), to wave-current interactions generating Langmuir circulations (e.g. Langmuir (1938); Maffioli et al. (2016); Gargett, Savidge (2020)), to inertial excitation of baroclinic shearing (e.g. Shearman (2005a); Zhang et al. (2018a)), to Ekman dynamics generating upwelling or downwelling fronts from along-shore winds (e.g. Austin, Lentz (2002); Miles et al. (2017). However, the observed response of the tropical cyclones to these various ocean processes that occur at timescales similar to the evolution of the storm breaks down into relatively simple categories. By breaking down the storms into three track-based categories of onshore, coastal, and offshore storms, a relatively simple heuristic framework of ocean responses can be generated.

Onshore storms and offshore storms, then become two sides of the same coin. As the ocean response is governed by far-field winds, which align along the shore to drive

	Onshore	**Coastal**	**Offshore**
Example storms	Isaias (2020)	Strong: Irene (2011) Weak: Fay (2020)	Hermine (2016)
Track location	Inland	MAB Continental Shelf	Deepwater offshore
Windfield	Steady alongshore upwelling favorable	Cross-shore, with rapid directional change with eye passage	Steady alongshore downwelling favorable
Subsurface ocean response	Upwelling front moves offshore forming a cold surface layer	Two layer cross shelf flow mixing across thermocline cooler & deeper surface layer	Downwelling front moves bottom layer offshore and surface remains warm
SST response	Rapid ahead of eye cooling nearshore	Strong: Rapid ahead of eye cooling across shelf Weak: Marginal after eye cooling	Remains steady
Change in Heat flux	Into ocean	Strong: Into ocean Weak: None	None
Impact on intensity	May weaken storm*	Strong: weakens storm Weak: None	None

Table 4.2: A breakdown of storm types into ocean and atmospheric responses.

two-dimensional Ekman transport of the near shore waters. In the offshore case, this leads to the advection of the Cold Pool bottom waters offshore as observed in the glider transects of temperature in Fig. 4.13. The bottom-attached downwelling front horizontal position separates the inshore single-layer warm ocean from the highly stratified two-layer ocean in the offshore. Thus the surface temperatures may cool as the surface waters are advected toward shore due to other atmospheric interaction or spatial variability, but the rapid cooling associated with bringing the dense, cold waters of the Cold Pool to the surface is not expected. The sea surface temperature at the air-sea interface then remains relatively warm, which allows for storm to maintain strength limited by the atmospheric circulation and the ahead-of-eye observations of SST.

Sandy represents a special case of the offshore storm as it occurred late in the season when the stratification had already started to break down and had an atypical cross-shelf track compared to the usual tracks that travel along the shore toward the northeast (Hall, Yonekura 2013). However due to the slow moving nature and large wind radius of Sandy, the along-shore winds had time to set up and develop the downwelling front that moved 70km offshore (Miles et al. 2017), which matched the linear model in Austin, Lentz (2002).

Inshore storms similarly generate along shore winds, but in the direction from South to North along the coast, which leads to upwelling favorable Ekman dynamics in the near-shore. The upwelling of Cold Pool waters into the near shore Tropical Storm Isaias (2020) showed upwards of 8 °C as shown in the NOAA satellite SST (Fig. 4.3) over an extensive region of the coastal ocean. Whereas the response of the SST for the downwelling in offshore storms is minimal, the strong SST change in upwelling storms occurring ahead-of-eye passage (shown in table 4.1) may lead to an alteration of storm intensity.

In coastal storms, unlike the other two track types, we do not observe the setup of Ekman frontal dynamics due to the ahead-of-eye winds being perpendicular to the coast. Rather in the period ahead of eye passage, we observe direct wind-forced mixing. As wind-induced shear controls the mixing, the shear profile (as modeled in chapter 2) acts to maintain a narrow pycnocline while it deepens by doing the work of thoroughly mixing the waters from the top of the pycnocline to the surface. In the case of strong storms (e.g. Irene (2011)) can lead to rapid deepening and entrainment of Cold Pool waters to the surface, which Seroka et al. (2016) showed led to the rapid weakening of the storm as it passed above the already cooled surface waters. For weaker tropical cyclones (e.g. Arthur (2014) and Fay (2020)), the same surface forcing is present, but due to the stability of the MAB water column is unable to bring large amounts of Cold Pool waters to the surface. However, both Arthur and Fay were Tropical Storms (wind speeds between (34-63 kt) while Irene was a Category 1 Hurricane (64-82 kt). This indicates that during periods of peak stratification in the MAB the cutoff may be Hurricane strength winds, but the factors of storm translation speed and size of wind-field may also play a role.

The after-eye period for coastal storms also has an essential ocean process that controls the dynamics. Modeled in Arthur by Zhang et al. (2018a) and observed in the ASOW ADCP during Fay, near-inertial currents are generated and interact with

the coast and create a shear across the pycnocline. This transition from direct wind-mixing to stratified shear as the eye passes leads to a broadening of the pycnocline, as shown in both Irene and Fay in Fig. 4.8 and Fig. 4.11 respectively. As this ocean process responds to eye passage, the cooling associated as the shear instabilities across the pycnocline yields minimal surface temperature change and is thus unlikely to affect the strength of the tropical cyclone. However as demonstrated in chapter 3, the development of a new mixed layer and recovery of the two-layer system is aided by this process.

4.6 Conclusions

In this study we use 13 years of an integrated ocean observing system that consists of Teledyne Webb Slocum gliders, a regional-scale HF Radar network, NOAA and industry buoys, and NOAA satellites to investigate the evolution of the Mid-Atlantic Bight under the influence of 11 tropical cyclones. Studies have detailed the co-evolution of tropical cyclones and the upper ocean as storms transit over the deep sea (Shay et al. 2000; Jaimes, Shay 2010; Sanford 2013; Rudzin et al. 2018). The MAB responds to tropical storm forcing with ocean processes both similar to the open ocean with wind shear-driven vertical mixing (Jaimes, Shay 2009) and shear due to near-inertial currents (Shearman 2005a), but also with three-dimensional upwelling and downwelling currents due to the interaction of the coast with Ekman dynamics (Austin, Lentz 2002). However, the response of the coastal ocean can be much greater than the typically observed response of the deep ocean and the rapid response of the coastal ocean can amplify the ahead of eye response that feedback on storm intensity. In this study, we show that the processes that control the ocean response can be predicted from the storm track. By separating the tracks into onshore, coastal, and offshore, we show that ahead-of-eye cooling is linked with the advection of Cold Pool waters to the surface via upwelling for onshore storms and wind-induced, shear-driven

vertical mixing for coastal storms. The results of this study highlight the need for continued combined ocean observing systems and further work on understanding the ocean-atmosphere coupled system for near-coast regions potential impact on storm intensity.

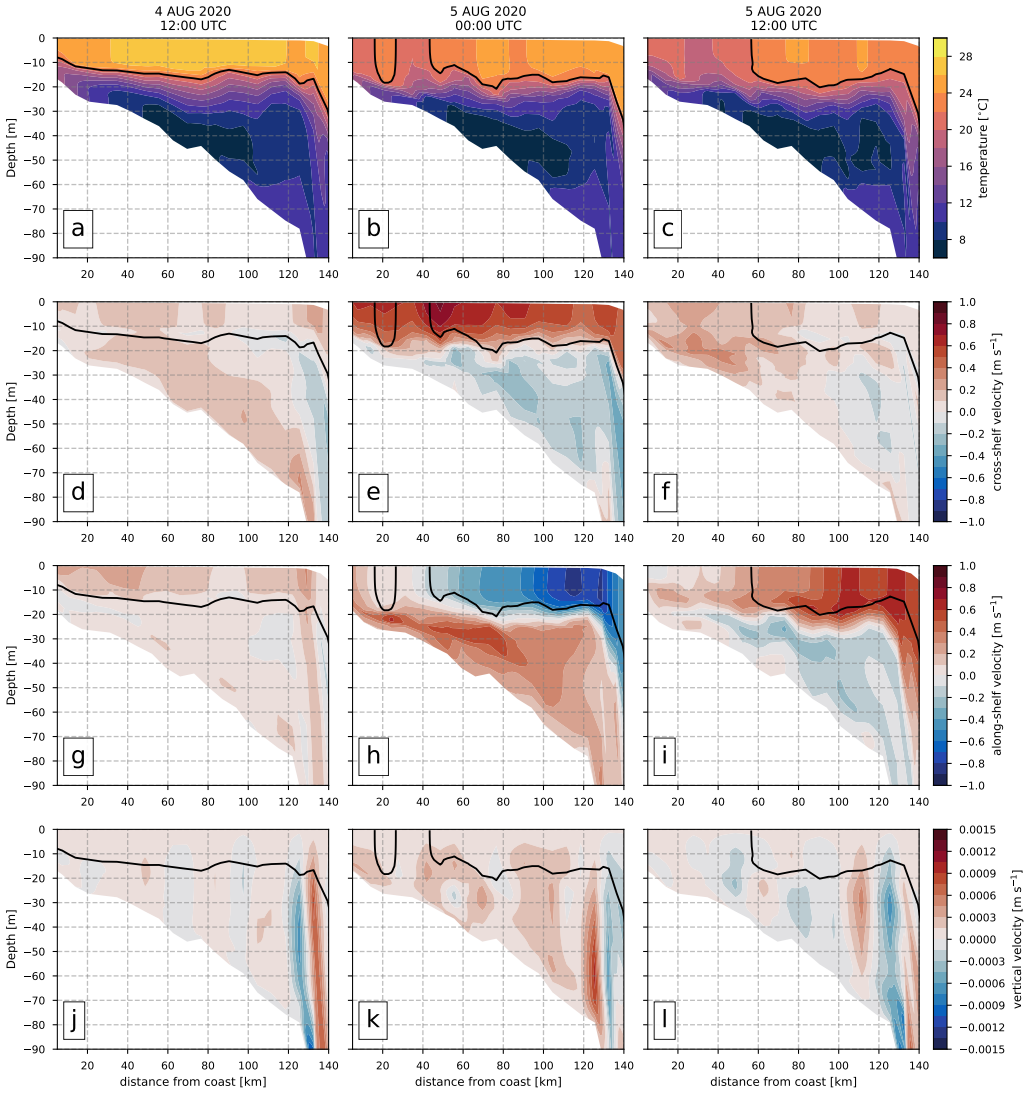

Figure 4.4: Cross-shelf slices of modeled temperature before, during, and after Isaias (2020) from ROMS DOPPIO where the distance from shore on the x-axis is positive in the offshore direction. Plots a-c are the temperature sections, d-f are cross shelf velocities, g-i are along shelf velocities, and j-l are vertical velocities. Additionally, we highlight the 22C isotherm to track the upwelling front in each plot with the solid black line.

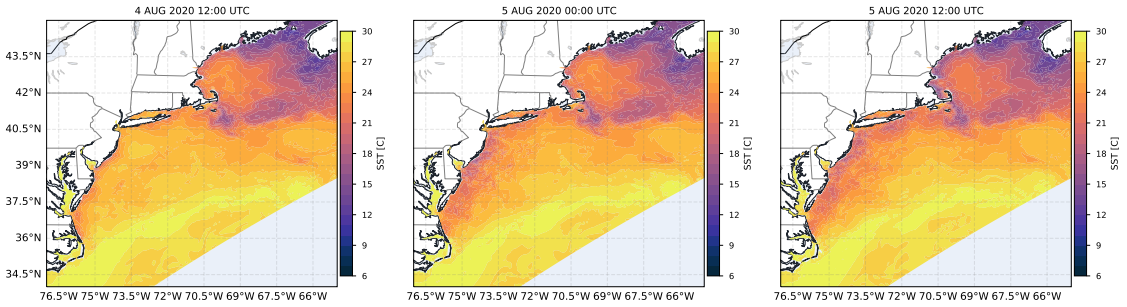

Figure 4.5: ROMS DOPPIO SSTs from before, during, and after the passage of Isaias, successfully reproduced the near-shore cooling and frontal displacement seen in Fig 4.3

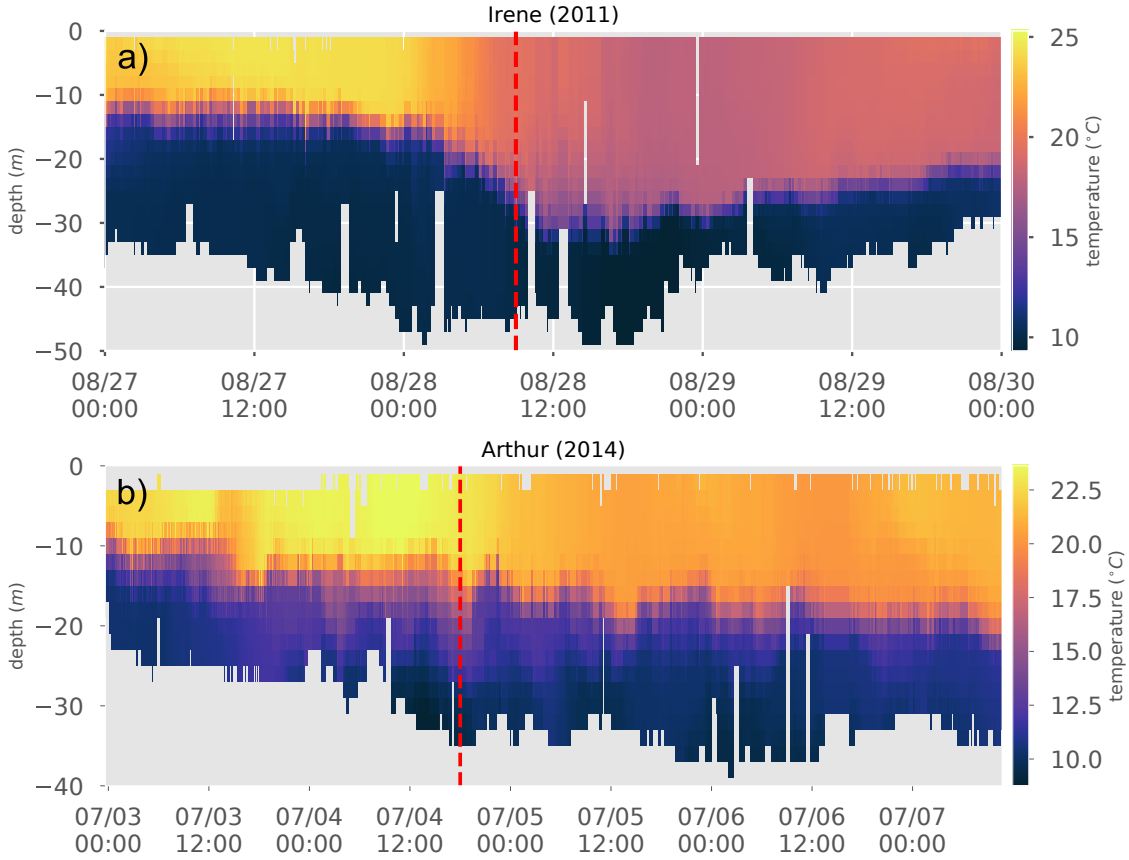

Figure 4.6: Glider observations of water temperature during a) Tropical Storm Arthur and b) Hurricane Irene, where the eye-passage is marked by the dashed red line. The response of the ocean to Arthur and Irene diverges greatly, with rapid mixing and cooling of the surface ahead of eye observed in Irene, but not in Arthur.

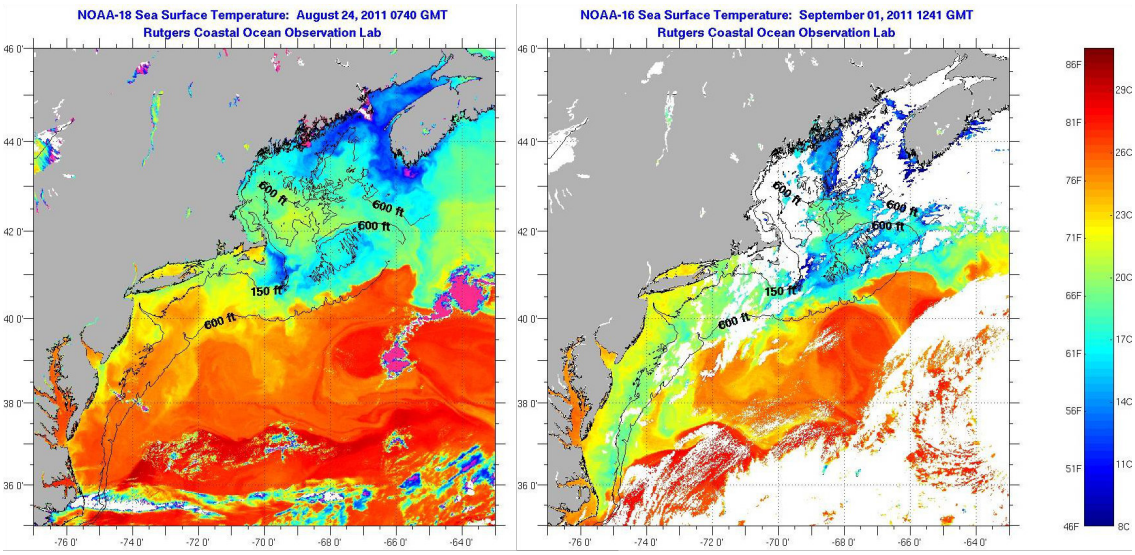

Figure 4.7: NOAA satellite SST from before and after the passage of Hurricane Irene displaying a shelf wide cooling with up to 6 °C, which directly led to the rapid de-intensification of Irene as shown in Seroka et al. (2016).

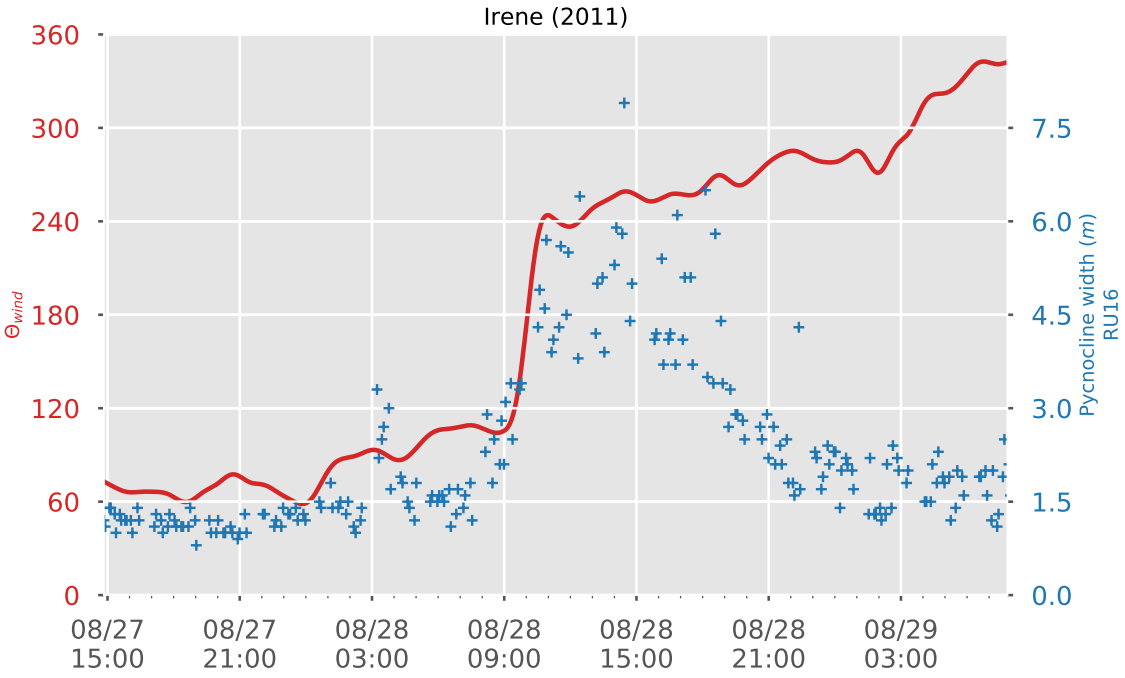

Figure 4.8: Comparison of wind direction data from Tuckerton along with the pycnocline width as calculated from the glider RU16 during Hurricane Irene (2011). The period of rapid wind direction change associated with the eye passage at Tuckerton, in a geographically similar region to RU16, is correlated with a broadening of the pycnocline.

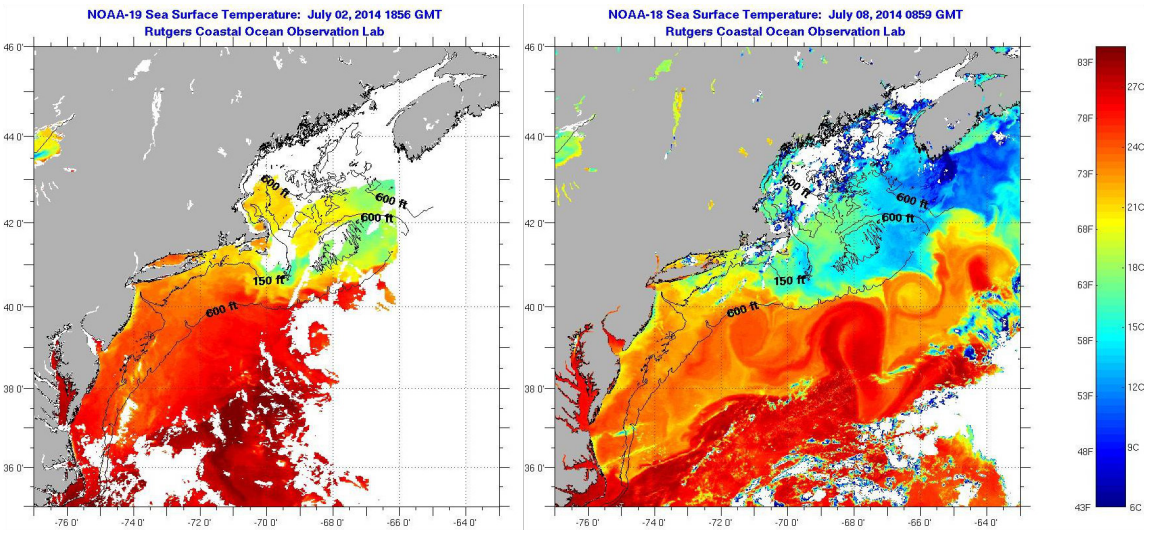

Figure 4.9: NOAA satellite SST from before and after the passage of Hurricane Arthur.

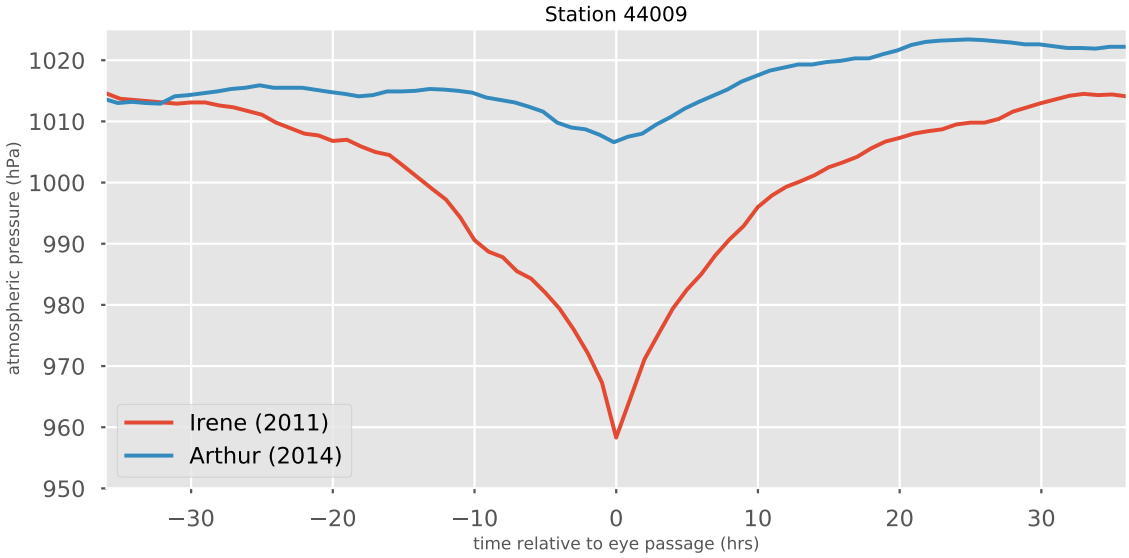

Figure 4.10: Comparison of Atmospheric Pressure in Irene (2011) and Arthur (2014), where the difference in strength of storms is readily apparent.

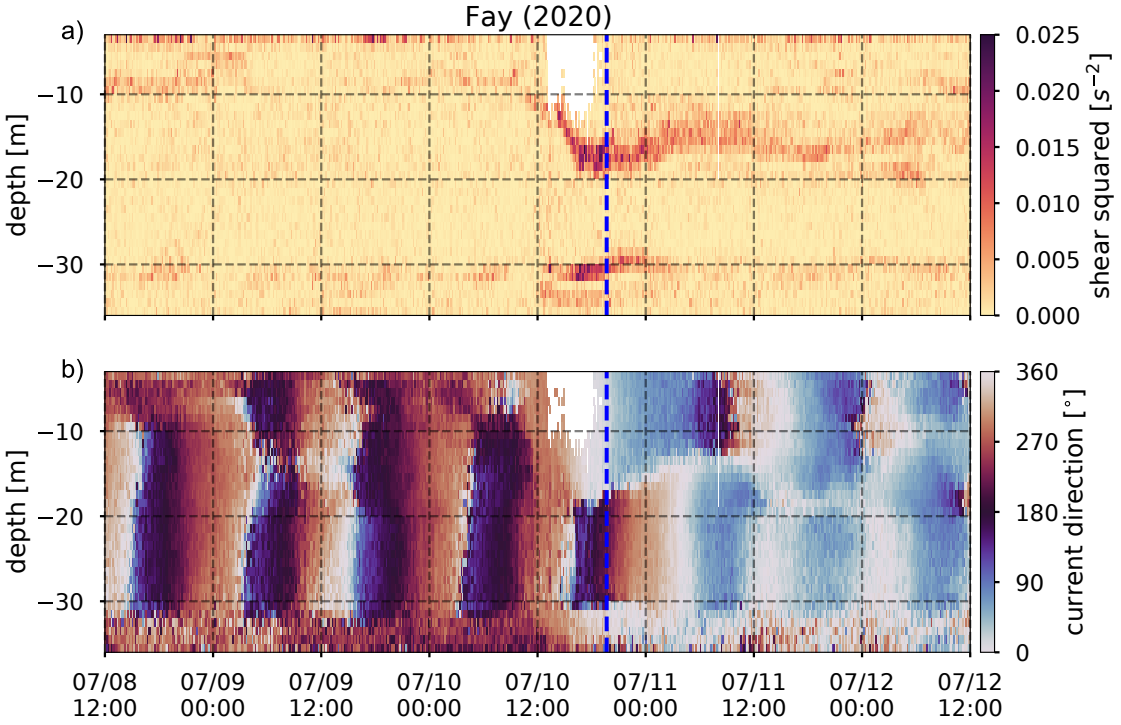

Figure 4.11: a) shear squared and b) current angle observed in Tropical Storm Fay (2020) by the ASOW buoy ADCP, where the current speed is too large the ADCP reported NaN values.

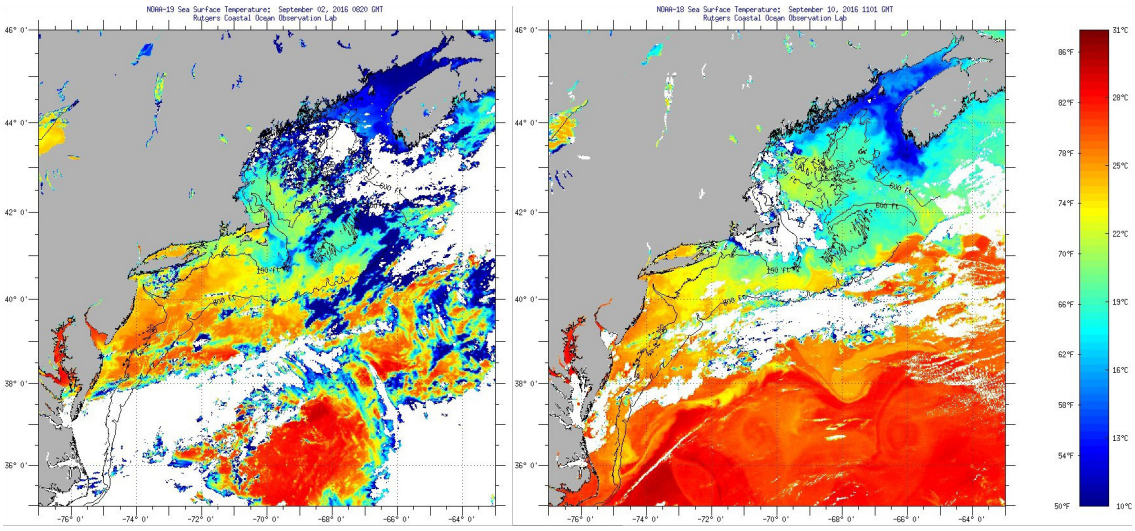

Figure 4.12: NOAA satellite SST from before and after the passage of Tropical Storm Hermine through the MAB.

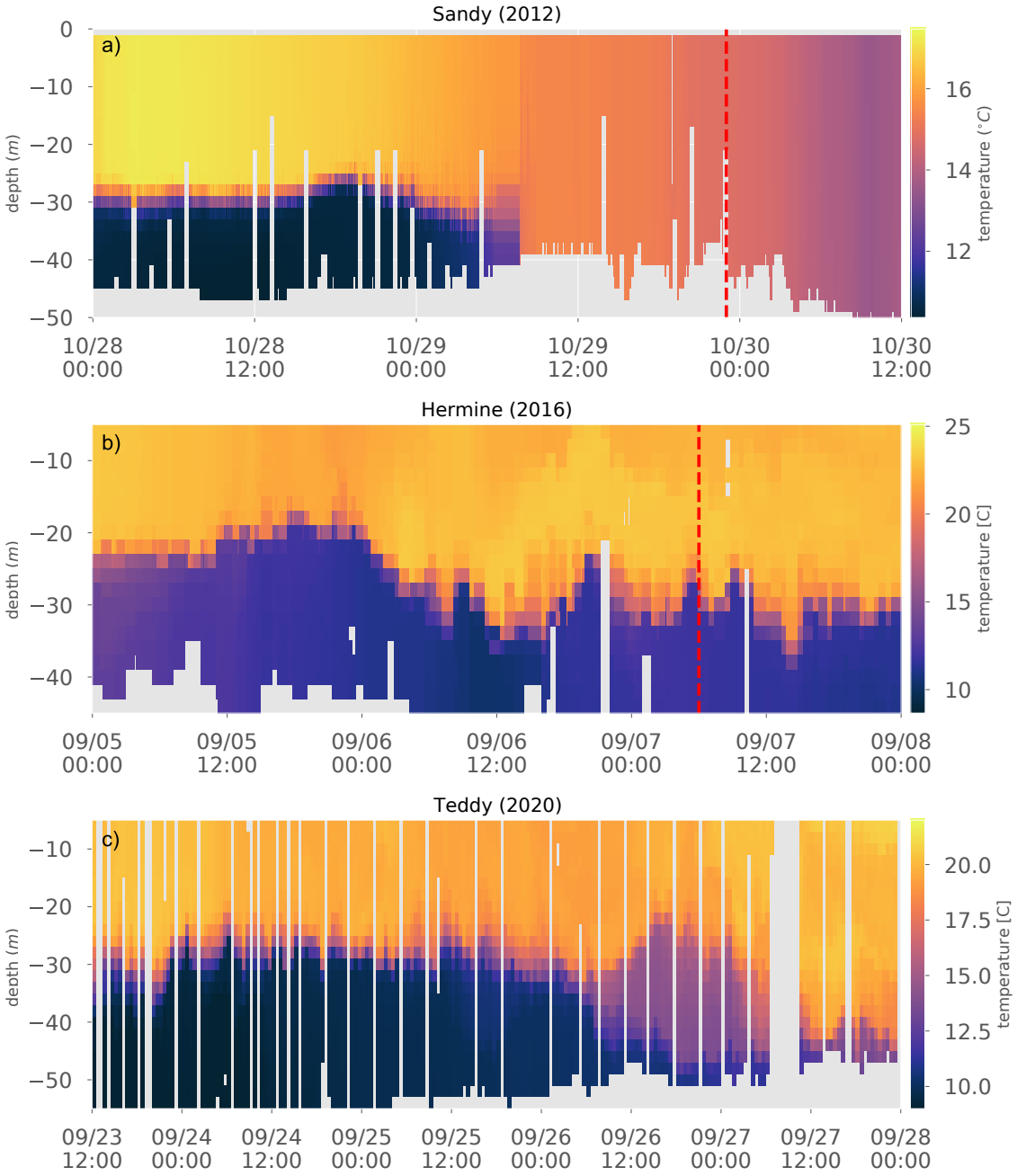

Figure 4.13: Glider observations of water temperature during a) Hurricane Sandy, b) Tropical Storm Hermine, and c) Tropical Storm Teddy, where time at which the eye was closest to the glider is marked by the dashed red line for Sandy and Hermine, where as for Teddy the eye was far away the entire time.

Chapter 5
Conclusions

This dissertation uses a combination of modeling (LES) with observations (autonomous gliders, HF radar, buoys, satellites, weather radar) and new analysis techniques (SLIM) to better understand how the ocean surface boundary layer and stratified coastal ocean interact with the winds at the scale of individual tropical cyclones to seasonal forcing. Chapter 2 used a horizontally expansive model to demonstrate the role of large aspect-ratio coherent structures in the behavior of the ocean surface boundary layer under idealized Hurricane forcing. From the LES, we observed that $\mathcal{O}(10\%)$ of the ahead-of-eye entrainment of colder waters to the surface was linked to the coherent rolls. Additionally by using the rotating wind forcing of a tropical cyclone, the results also demonstrate that there are systematic relationships between mean flow properties that were altered during the rapid change in wind forcing direction during eye-passage, e.g. the flux Richardson number and the turbulent Prandtl number. Chapter 3 used HF radar derived currents and NAM reanalysis winds to generate a predictive algorithm for the mixed layer, SLIM. We showed that SLIM was capable of capturing the time dependent behavior of the mixed layer over spatial domain of the MAB, illustrating the shelf-wide, ahead-of-eye deepening before Irene and the seasonal cycle of Fall breakdown of the Cold Pool that includes a series of storm events interspersed with restratification events until the stratification is fully eroded to well mixed winter conditions. Chapter 4 used a collection of *in situ* data collected in the MAB since 2007 to evaluate the ocean responses to tropical cyclones, particularly looking at the mixed layer. We show that the storms can be broken into three main track types based on location relative to the continental shelf, each with

corresponding essential ocean processes.

As the methods are diverse for investigating the mixed layer within this dissertation, the future work intimated by each chapter is slightly different. For the LES, there are a number of questions that are hard to answer without another computationally expensive model run. What is the effect of a surface wave field on the Ekman-roll like coherent structures that develop within our model? The role of coherent structures seems to be to keep the mixed layer in a marginal stability and adding stokes drift and wave-current interactions into the relatively steady ahead-of-eye wind forcing would lead to insights about the competing processes and wavelengths of instability. And importantly for a region like the MAB with high spatial variability where frontal structures from upwelling and downwelling occur, are the dynamics described in an ocean without horizontal density gradients applicable across a front? Work in Whitt, Taylor (2017) showed that horizontal density gradients act to limit mixing, does this process mitigate some of the ahead-of-eye cooling?

Additionally, we attempted to simplify the ocean response to tropical storm forcing down to the dominant essential ocean process for each type. How much does the upwelling of Cold Pool waters in the near shore ocean change the intensity of onshore track tropical storms? What is the lower bound on storm intensity to generate mixing and enough cooling to affect atmospheric conditions? And related to chapter 2, is this dependent on how mixing is parameterized? Running coupled models of onshore and coastal type storms with varying strengths could generate a predictive heuristic that could be simple enough to share at the public level.

Bibliography

Ambler Julie W, Kumar Ajoy, Moisan Tiffany A, Aulenbach Donielle L, Day Melissa C, Dix Stephanie A, Winsor Michele A. Seasonal and spatial patterns of Penilia avirostris and three tunicate species in the southern Mid-Atlantic Bight // Continental Shelf Research. 2013. 69. 141–154.

Anderson Philip S. Measurement of Prandtl number as a function of Richardson number avoiding self-correlation // Boundary-layer meteorology. 2009. 131, 3. 345–362.

Anis A, Moum JN. Surface wave–turbulence interactions. scaling ε (z) near the sea surface // Journal of Physical Oceanography. 1995. 25, 9. 2025–2045.

Asai Tomio, Nakasuji Isao. On the stability of Ekman boundary layer flow with thermally unstable stratification // Journal of the Meteorological Society of Japan. Ser. II. 1973. 5, 1. 29—-42.

Austin Jay A, Lentz Steven J. The inner shelf response to wind-driven upwelling and downwelling // Journal of Physical Oceanography. 2002. 32, 7. 2171–2193.

Behrenfeld Michael J, O'Malley Robert T, Siegel David A, McClain Charles R, Sarmiento Jorge L, Feldman Gene C, Milligan Allen J, Falkowski Paul G, Letelier Ricardo M, Boss Emmanuel S. Climate-driven trends in contemporary ocean productivity // Nature. 2006. 444, 7120. 752.

Belcher Stephen E, Grant Alan LM, Hanley Kirsty E, Fox-Kemper Baylor, Van Roekel Luke, Sullivan Peter P, Large William G, Brown Andy, Hines Adrian, Calvert

Daley, others . A global perspective on Langmuir turbulence in the ocean surface boundary layer // Geophysical Research Letters. 2012. 39, 18.

Bigelow Henry Bryant. Studies of the waters on the continental shelf, Cape Cod to Chesapeake Bay. I. The cycle of temperature. 1933.

Brown Robert A. On the inflection point instability of a stratified Ekman boundary layer // Journal of the Atmospheric Sciences. 1972. 29, 5. 850–859.

Businger Joost A, Wyngaard John C, Izumi Y, Bradley Edward F. Flux-profile relationships in the atmospheric surface layer // Journal of the atmospheric Sciences. 1971. 28, 2. 181–189.

Callies Jörn, Ferrari Raffaele. Interpreting energy and tracer spectra of upper-ocean turbulence in the submesoscale range (1–200 km) // Journal of Physical Oceanography. 2013. 43, 11. 2456–2474.

Callies Jörn, Ferrari Raffaele. Baroclinic instability in the presence of convection // Journal of Physical Oceanography. 2018. 48, 1. 45–60.

Cangialosi John P, Franklin James L. 2011 National Hurricane Center forecast verification report // National Hurricane Center. 2012.

Carvalho Filipa, Kohut Josh, Oliver Matthew J., Schofield Oscar. Defining the ecologically relevant mixed-layer depth for Antarctica's coastal seas // Geophysical Research Letters. 2017. 44, 1. 338–345.

Chang Ming-Huei, Jheng Sin-Ya, Lien Ren-Chieh. Trains of large Kelvin-Helmholtz billows observed in the Kuroshio above a seamount // Geophysical Research Letters. 2016. 43, 16. 8654–8661.

Chant R. J. Interactions between Estuaries and Coasts: River Plumes - Their Formation, Transport, and Dispersal // Treatise on Estuarine and Coastal Science. 2012. 2. 213–235.

Charria Guillaume, Theetten Sébastien, Vandermeirsch Frédéric, Yelekçi Özge, Audiffren Nicole. Interannual evolution of (sub) mesoscale dynamics in the Bay of Biscay // Ocean Science. 2017. 13, 5. 777.

Chawla Arun, Spindler Deanna M, Tolman Hendrik L. Validation of a thirty year wave hindcast using the Climate Forecast System Reanalysis winds // Ocean Modelling. 2013. 70. 189–206.

Chen Zhuomin, Curchitser Enrique, Chant Robert, Kang Dujuan. Seasonal Variability of the Cold Pool Over the Mid-Atlantic Bight Continental Shelf // Journal of Geophysical Research: Oceans. 2018.

Choi J, Park Y-G, Kim W, Kim YH. Characterization of submesoscale turbulence in the east/japan sea using geostationary ocean color satellite images // Geophysical Research Letters. 2019. 46, 14. 8214–8223.

Chu Peter, Yuchun Chen, Kuninaka Akira. Seasonal variability of the Yellow Sea/East China Sea surface fluxes and thermohaline structure // Advances in Atmospheric Sciences. 2005. 22, 1. 1–20.

Cornillon Peter, Stramma Lothar, Price James F. Satellite measurements of sea surface cooling during hurricane Gloria // Nature. 1987. 326, 6111. 373–375.

Czeschel Lars, Eden Carsten. Internal wave radiation through surface mixed layer turbulence // Journal of Physical Oceanography. 2019. 49, 7. 1827–1844.

D'Asaro E. A. The decay of wind-forced mixed layer inertial oscillations due to the β effect. // J. Geophys. Res. 1989. 94, C2. 2045–2056.

D'Asaro Eric a. The decay of wind-forced mixed layer inertial oscillations due to the β effect // Journal of Geophysical Research. 1989. 94. 2045.

Demuth Julie L, Morss Rebecca E, Morrow Betty Hearn, Lazo Jeffrey K. Creation and communication of hurricane risk information // Bulletin of the American Meteorological Society. 2012. 93, 8. 1133–1145.

Deusebio Enrico, Brethouwer G., Schlatter P., Lindborg E. A numerical study of the unstratified and stratified Ekman layer // Journal of Fluid Mechanics. 2014. 755. 672–704.

Dohan Kathleen, Davis Russ E. Mixing in the transition layer during two storm events // Journal of Physical Oceanography. 2011. 41, 1. 42–66.

Domingues Ricardo, Kuwano-Yoshida Akira, Chardon-Maldonado Patricia, Todd Robert E., Halliwell George, Kim Hyun-Sook, Lin I.-I., Sato Katsufumi, Narazaki Tomoko, Shay Lynn K., Miles Travis, Glenn Scott, Zhang Jun A., Jayne Steven R., Centurioni Luca, Le Hénaff Matthieu, Foltz Gregory R., Bringas Francis, Ali M. M., DiMarco Steven F., Hosoda Shigeki, Fukuoka Takuya, LaCour Benjamin, Mehra Avichal, Sanabia Elizabeth R., Gyakum John R., Dong Jili, Knaff John A., Goni Gustavo. Ocean Observations in Support of Studies and Forecasts of Tropical and Extratropical Cyclones // Frontiers in Marine Science. 2019. 6. 446.

Dong Shenfu, Kelly Kathryn A. Heat budget in the Gulf Stream region: The importance of heat storage and advection // Journal of physical oceanography. 2004. 34, 5. 1214–1231.

Duncombe Jenessa R. Linear Theory of Roll Instabilities in the Ocean Surface Layer. 2017.

D'Asaro Eric A, Shcherbina Andrey Y, Klymak Jody M, Molemaker Jeroen, Novelli Guillaume, Guigand Cédric M, Haza Angelique C, Haus Brian K, Ryan Edward H, Jacobs Gregg A, others . Ocean convergence and the dispersion of flotsam // Proceedings of the National Academy of Sciences. 2018. 115, 6. 1162–1167.

Ekman V. W. On the influence of the earth's rotation on ocean currents. // Ark. Mat. Astr. Fys. 1905. 2. 1–52.

Elachi Charles, Apel John R. Internal wave observations made with an airborne synthetic aperture imaging radar // Geophysical Research Letters. 1976. 3, 11. 647–650.

Elsberry Russell L, Fraim Thomas S, Trapnell Jr Robert N. A mixed layer model of the oceanic thermal response to hurricanes // Journal of Geophysical Research. 1976. 81, 6. 1153–1162.

Emanuel Kerry. Tropical cyclones // Annual review of earth and planetary sciences. 2003. 31.

Etling Do, Brown RA. Roll vortices in the planetary boundary layer: A review // Boundary-Layer Meteorology. 1993. 65, 3. 215–248.

Evans Dafydd Gwyn, Lucas Natasha Sarah, Hemsley Victoria, Frajka-Williams Eleanor, Naveira Garabato Alberto C, Martin Adrian, Painter Stuart C, Inall Mark E, Palmer Matthew R. Annual cycle of turbulent dissipation estimated from Seagliders // Geophysical Research Letters. 2018. 45, 19. 10–560.

Fairall Chris W, Bradley Edward F, Hare JE, Grachev Andrey A, Edson James B. Bulk parameterization of air–sea fluxes: Updates and verification for the COARE algorithm // Journal of climate. 2003. 16, 4. 571–591.

Fang Jiannong, Porté-Agel Fernando. Large-eddy simulation of very-large-scale motions in the neutrally stratified atmospheric boundary layer // Boundary-Layer Meteorology. 2015. 155, 3. 397–416.

Fernández Emilio, Pingree Robin D. Coupling between physical and biological fields in the North Atlantic subtropical front southeast of the Azores // Deep Sea Research Part I: Oceanographic Research Papers. 1996. 43, 9. 1369–1393.

Flagg Charles N, Dunn Maureen, Wang Dong-ping, Rossby H Thomas, Benway Robert L. A study of the currents of the outer shelf and upper slope from a decade of shipboard ADCP observations in the Middle Atlantic Bight // Journal of Geophysical Research. 2006. 111. 1–20.

Friedland Kevin D, Leaf Robert T, Kane Joe, Tommasi Desiree, Asch Rebecca G, Rebuck Nathan, Ji Rubao, Large Scott I, Stock Charles, Saba Vincent S. Spring bloom dynamics and zooplankton biomass response on the US Northeast Continental Shelf // Continental Shelf Research. 2015. 102. 47–61.

Fritz Hermann M, Blount Chris, Sokoloski Robert, Singleton Justin, Fuggle Andrew, McAdoo Brian G, Moore Andrew, Grass Chad, Tate Banks. Hurricane Katrina storm surge distribution and field observations on the Mississippi Barrier Islands // Estuarine, Coastal and Shelf Science. 2007. 74, 1-2. 12–20.

Gargett A, Wells J, Tejada-Martinez AE, Grosch CE. Langmuir supercells: A mechanism for sediment resuspension and transport in shallow seas // Science. 2004. 306, 5703. 1925–1928.

Gargett Ann E, Savidge Dana K. Winds, Waves, and Turbulence on a Shallow Continental Shelf during Passage of a Tropical Storm // Journal of Physical Oceanography. 2020. 50, 5. 1341–1364.

Gargett Ann E, Wells Judith R. Langmuir turbulence in shallow water. Part 1. Observations // Journal of Fluid Mechanics. 2007. 576. 27–61.

Glenn SM, Miles TN, Seroka GN, Xu Y, Forney RK, Yu F, Roarty H, Schofield Oscar, Kohut Joshua. Stratified coastal ocean interactions with tropical cyclones // Nature communications. 2016. 7, 1. 1–10.

Glenn Scott, Aragon Dave, Bowers Louis, Crowley Michael, Dunk Rich, Evans Colin, Haldeman Chip, Handel Ethan, Haskins Tina, Kerfoot John, others . Process-driven improvements to hurricane intensity and storm surge forecasts in the mid-atlantic bight: Lessons learned from hurricanes irene and sandy // 2013 MTS/IEEE OCEANS-Bergen. 2013. 1–9.

Grant William D, Madsen Ole S. The continental-shelf bottom boundary layer // Annual Review of Fluid Mechanics. 1986. 18, 1. 265–305.

Grant William D, Madsen Ole Secher. Combined wave and current interaction with a rough bottom // Journal of Geophysical Research: Oceans. 1979. 84, C4. 1797–1808.

Hall Timothy, Yonekura Emmi. North American tropical cyclone landfall and SST: A statistical model study // Journal of climate. 2013. 26, 21. 8422–8439.

Hamlington P. E., VanRoekel L. P., Fox-Kemper B., Julien K., Chini G. Langmuir-Submesoscale Interactions: Descriptive Analysis of Multiscale Frontal Spindown Simulations. // J. Phys. Oceanogr. 2014. 44. 2249–2272.

Hazel Philip. Numerical studies of the stability of inviscid stratified shear flows // Journal of Fluid Mechanics. 1972. 51, 1. 39–61.

Holt Steven E, Koseff Jeffrey R, Ferziger Joel H. A numerical study of the evolution and structure of homogeneous stably stratified sheared turbulence // Journal of Fluid Mechanics. 1992. 237. 499–539.

Houghton Robert W, Schlitz Ronald, Beardsley Robert C, Butman Bradford, Chamberlin J Lockwood. The Middle Atlantic Bight cold pool: Evolution of the temperature structure during summer 1979 // Journal of Physical Oceanography. 1982. 12, 10. 1019–1029.

Howard Louis N. Note on a paper of John W. Miles // Journal of Fluid Mechanics. 1961. 10, 4. 509–512.

Hutchins Nicholas, Chauhan Kapil, Marusic Ivan, Monty Jason, Klewicki Joseph. Towards reconciling the large-scale structure of turbulent boundary layers in the atmosphere and laboratory // Boundary-layer meteorology. 2012. 145, 2. 273–306.

Jacob S Daniel, Shay Lynn K, Mariano Arthur J, Black Peter G. The 3D oceanic mixed layer response to Hurricane Gilbert // Journal of Physical Oceanography. 2000. 30, 6. 1407–1429.

Jaimes Benjamin, Shay Lynn K. Mixed layer cooling in mesoscale oceanic eddies during Hurricanes Katrina and Rita // Monthly Weather Review. 2009. 137, 12. 4188–4207.

Jaimes Benjamin, Shay Lynn K. Near-inertial wave wake of hurricanes Katrina and Rita over mesoscale oceanic eddies // J. Phys. Oceanogr. 2010. 40. 1320–1337.

Jansen Malte F, Ferrari Raffaele, Mooring Todd A. Seasonal versus permanent thermocline warming by tropical cyclones // Geophysical Research Letters. 2010. 37, 3.

Jeronimo Gilberto, Gomez-Valdes Jose. Mixed layer depth variability in the tropical boundary of the California Current, 1997-2007 // Journal of Geophysical Research: Oceans. 2010. 115, 5.

Kaltenbach H-J, Gerz Thomas, Schumann Ulrich. Large-eddy simulation of homogeneous turbulence and diffusion in stably stratified shear flow // J. Fluid Mech. 1994. 280. 1–40.

Kaminski AK, Smyth WD. Stratified shear instability in a field of pre-existing turbulence // Journal of Fluid Mechanics. 2019. 862. 639–658.

Kara A. Birol, Rochford Peter A., Hurlburt Harley E. An optimal definition for ocean mixed layer depth // Journal of Geophysical Research: Oceans. 2000. 105, C7. 16803–16821.

Kaylor Robert, Faller Alan J. Instability of the stratified Ekman boundary layer and the generation of internal waves // Journal of the Atmospheric Sciences. 1972. 29, 3. 497–509.

Keim Barry D, Muller Robert A, Stone Gregory W. Spatiotemporal patterns and return periods of tropical storm and hurricane strikes from Texas to Maine // Journal of climate. 2007. 20, 14. 3498–3509.

Kelly Samuel M. Coastally generated near-inertial waves // Journal of Physical Oceanography. 2019. 49, 11. 2979–2995.

Khanna Samir, Brasseur James G. Three-dimensional buoyancy-and shear-induced local structure of the atmospheric boundary layer // Journal of the atmospheric sciences. 1998. 55, 5. 710–743.

Kim Sung Yong, Kurapov Alexander L., Kosro P. Michael. Influence of varying upper ocean stratification on coastal near-inertial currents // Journal of Geophysical Research: Oceans. 2015. 120, 12. 8504–8527.

Kraus E. B., Turner J. S. A one-dimensional model of the seasonal thermocline II. The general theory and its consequences // Tellus. 1967. 19, 1. 98–106.

Kukulka Tobias, Plueddemann Albert J, Trowbridge John H, Sullivan Peter P. Significance of Langmuir circulation in upper ocean mixing: Comparison of observations and simulations // Geophysical Research Letters. 2009. 36, 10.

Kundu Pijush K, Chao Shenn-Yu, McCREARY JULIAN P. Transient coastal currents and inertio-gravity waves // Deep Sea Research Part A. Oceanographic Research Papers. 1983. 30, 10. 1059–1082.

Langmuir Irving. Surface motion of water induced by wind // Science. 1938. 87, 2250. 119–123.

Large W G, Mcwilliams J C, Doney S C. Oceanic Vertical Mixing - a Review and a Model with a Nonlocal Boundary-Layer Parameterization // Reviews of Geophysics. 1994a. 32, 94. 363–403.

Large William G, Danabasoglu Gokhan, Doney Scott C, McWilliams James C. Sensitivity to surface forcing and boundary layer mixing in a global ocean model: Annual-mean climatology // Journal of Physical Oceanography. 1997. 27, 11. 2418–2447.

Large William G, McWilliams James C, Doney Scott C. Oceanic vertical mixing: A review and a model with a nonlocal boundary layer parameterization // Reviews of Geophysics. 1994b. 32, 4. 363–403.

Large William G, Patton Edward G, Sullivan Peter P. Nonlocal Transport and Implied Viscosity and Diffusivity throughout the Boundary Layer in LES of the Southern Ocean with Surface Waves // Journal of Physical Oceanography. 2019. 49, 10. 2631–2652.

Leibovich Sidney. The form and dynamics of Langmuir circulations // Annual Review of Fluid Mechanics. 1983. 15, 1. 391–427.

Lemone Margaret A. Modulation of turbulence energy by longitudinal rolls in an unstable planetary boundary layer // Journal of the Atmospheric Sciences. 1976. 33, 7. 1308–1320.

Lemone Margaret Anne. The structure and dynamics of horizontal roll vortices in the planetary boundary layer // Journal of the Atmospheric Sciences. 1973. 30, 6. 1077–1091.

Lentz Steven J. Observations and a Model of the Mean Circulation over the Middle Atlantic Bight Continental Shelf // Journal of Physical Oceanography. 2008. 38, June. 1203–1221.

Li Ming, Garrett Chris, Skyllingstad Eric. A regime diagram for classifying turbulent large eddies in the upper ocean // Deep Sea Research Part I: Oceanographic Research Papers. 2005. 52, 2. 259–278.

Li Xiaofeng, Clemente-Colón Pablo, Friedman Karen S. Estimating oceanic mixed-layer depth from internal wave evolution observed from Radarsat-1 SAR // Johns Hopkins APL Technical Digest (Applied Physics Laboratory). 2000. 21, 1. 130–135.

Lombardo CP, Gregg MC. Similarity scaling of viscous and thermal dissipation in a convecting surface boundary layer // Journal of Geophysical Research: Oceans. 1989. 94, C5. 6273–6284.

López Alexander G, Wilkin John L, Levin Julia C. Doppio–a ROMS (v3. 6)-based circulation model for the Mid-Atlantic Bight and Gulf of Maine: configuration and comparison to integrated coastal observing network observations // Geoscientific Model Development. 2020. 13, 8. 3709–3729.

Lorbacher Katja, Dommenget Dietmar, Niiler PP, Köhl A. Ocean mixed layer depth: A subsurface proxy of ocean-atmosphere variability // Journal of Geophysical Research: Oceans. 2006. 111, C7.

MacKinnon J. A, Gregg M. C. Near-Inertial Waves on the New England Shelf : The Role of Evolving Stratification , Turbulent Dissipation , and Bottom Drag // Journal of Physical Oceanography. 2005. 25. 2408–2424.

Maffioli Andrea, Brethouwer Geert, Lindborg Erik. Mixing efficiency in stratified turbulence // Journal of Fluid Mechanics. 2016. 794.

Mahjabin Tanziha, Pattiaratchi Charitha, Hetzel Yasha. Wind effects on dense shelf water cascades in south-west Australia // Continental Shelf Research. 2019. 189. 103975.

Marmorino GO, Smith GB, Lindemann GJ. Infrared imagery of large-aspect-ratio Langmuir circulation // Continental Shelf Research. 2005. 25, 1. 1–6.

Marmorino George, Chen Wei. Use of WorldView-2 Along-Track Stereo Imagery to Probe a Baltic Sea Algal Spiral // Remote Sensing. 2019. 11, 7. 865.

Marra John, Houghton RW, Garside Christopher. Phytoplankton growth at the shelf-break front in the Middle Atlantic Bight // Journal of Marine Research. 1990. 48, 4. 851–868.

Marusic Ivan, McKeon Beverley J, Monkewitz Peter A, Nagib Hassan M, Smits Alexander J, Sreenivasan Katepalli R. Wall-bounded turbulent flows at high Reynolds numbers: recent advances and key issues // Physics of Fluids. 2010. 22, 6. 065103.

Matano Ricardo P, Palma Elbio D. Seasonal variability of the oceanic circulation in the Gulf of San Jorge, Argentina // Oceanography. 2018. 31, 4. 16–24.

McClain E Paul, Pichel William G, Walton Charles C. Comparative performance of AVHRR-based multichannel sea surface temperatures // Journal of Geophysical Research: Oceans. 1985. 90, C6. 11587–11601.

McWilliams J. Submesoscale currents in the ocean. // Proc. R. Soc. A. 2016. 472. 20160117.

McWilliams James C, Sullivan Peter P, Moeng Chin-Hoh. Langmuir turbulence in the ocean // Journal of Fluid Mechanics. 1997. 334. 1–30.

Mellor George L, Yamada Tetsuji. Development of a turbulence closure model for geophysical fluid problems // Reviews of Geophysics. 1982. 20, 4. 851–875.

Merckelbach Lucas, Berger Anja, Krahmann Gerd, Dengler Marcus, Carpenter Jeffrey R. A dynamic flight model for Slocum gliders and implications for turbulence microstructure measurements // Journal of Atmospheric and Oceanic Technology. 2019. 36, 2. 281–296.

Micchelli Charles A, Rivlin Th J, Winograd Shmuel. The optimal recovery of smooth functions // Numerische Mathematik. 1976. 26, 2. 191–200.

Miles John W. On the stability of heterogeneous shear flows // Journal of Fluid Mechanics. 1961. 10, 4. 496–508.

Miles Travis, Glenn Scott M, Schofield Oscar. Temporal and spatial variability in fall storm induced sediment resuspension on the Mid-Atlantic Bight // Continental Shelf Research. 2013. 63. S36–S49.

Miles Travis, Seroka Greg, Glenn Scott. Coastal ocean circulation during Hurricane Sandy // Journal of Geophysical Research: Oceans. 2017. 122, 9. 7095–7114.

Moeng Chin-Hoh, Sullivan Peter P. A comparison of shear-and buoyancy-driven planetary boundary layer flows // Journal of the Atmospheric Sciences. 1994. 51, 7. 999–1022.

Monin A S, Obukhov A M. Basic laws of turbulent mixing in the surface layer of the atmosphere // Contrib. Geophys. Inst. Acad. Sci. USSR. 1954. 151, 163. e187.

Moum J. N., Nash J. D. Seafloor pressure measurements of nonlinear internal waves // Journal of Physical Oceanography. 2008. 38, 2. 481–491.

Mountain David G. Variability in the properties of Shelf Water in the Middle Atlantic Bight, 1977–1999 // Journal of Geophysical Research: Oceans. 2003a. 108, C1.

Mountain David G. Variability in the properties of Shelf Water in the Middle Atlantic Bight, 1977–1999 // Journal of Geophysical Research. 2003b. 108, C1. 3014.

Munk W., Armi L., Fischer K., Zachariasen F. Spirals on the sea. // Proc. R. Soc. Lond. A. 2000. 456. 1217–1280.

Nam Sunghyun, Park Young Gyu. Simulation of wind-induced near-inertial oscillations in a mixed layer near the east coast of Korea in the East/Japan Sea // Acta Oceanologica Sinica. 2013. 32, 9. 11–20.

Osborn T. Estimates of the local rate of vertical diffusion from dissipation measurements. // J. Phys. Oceanogr. 1980. 10. 83–89.

Park Jong Jin, Kim Kuh, Schmitt Raymond W. Global distribution of the decay timescale of mixed layer inertial motions observed by satellite-tracked drifters // Journal of Geophysical Research: Oceans. 2009. 114, 11.

Paulson Clayton A, Simpson James J. Irradiance measurements in the upper ocean // Journal of Physical Oceanography. 1977. 7, 6. 952–956.

Pollard R. T. On the generation by winds of inertial waves in the ocean // Deep-Sea Research and Oceanographic Abstracts. 1970. 17, 4. 795–812.

Pollard R. T., Millard R. C. Comparison between observed and simulated wind-generated inertial oscillations // Deep-Sea Research and Oceanographic Abstracts. 1970a. 17, 4.

Pollard R. T., Millard R. C. Comparison between observed and simulated wind-generated inertial oscillations // Deep Sea Res. 1970b. 17. 813–821.

Pollard R. T., Rhines P. B., Thompson R. The deepening of the wind-mixed layer. // Geophys. Fluid Dyn. 1972. 4, 1. 381–404.

Pollard Raymond T, Rhines Peter B, Thompson Rory ORY. The deepening of the wind-mixed layer // Geophysical Fluid Dynamics. 1973. 4, 4. 381–404.

Polton Jeff A, Smith Jerome A, MacKinnon Jennifer A, Tejada-Martínez Andrés E. Rapid generation of high-frequency internal waves beneath a wind and wave forced oceanic surface mixed layer // Geophysical Research Letters. 2008. 35, 13.

Potter Henry, DiMarco Steven F, Knap Anthony H. Tropical cyclone heat potential and the rapid intensification of Hurricane Harvey in the Texas Bight // Journal of Geophysical Research: Oceans. 2019. 124, 4. 2440–2451.

Price James F, Weller Robert A, Pinkel Robert. Diurnal cycling: Observations and models of the upper ocean response to diurnal heating, cooling, and wind mixing // Journal of Geophysical Research: Oceans. 1986. 91, C7. 8411–8427.

Qiao Fangli, Dai Dejun, Simpson John, Svendsen Harald. Banded structure of drifting macroalgae // Marine pollution bulletin. 2009. 58, 12. 1792–1795.

Rife Daran L., Davis Christopher A. Verification of Temporal Variations in Mesoscale Numerical Wind Forecasts // Monthly Weather Review. 2005. 133, 11. 3368–3381.

Roarty Hugh, Glenn Scott, Brodie Joseph, Nazzaro Laura, Smith Michael, Handel Ethan, Kohut Josh, Updyke Teresa, Atkinson Larry, Boicourt William, others . Annual and Seasonal Surface Circulation over the Mid Atlantic Bight Continental Shelf Derived from a Decade of High Frequency Radar Observations // Journal of Geophysical Research: Oceans. 2020. e2020JC016368.

Roarty Hugh, Glenn Scott, Kohut Josh, Gong Donglai, Handel Ethan, Rivera Erick, Garner Teresa, Atkinson Larry, Brown Wendell, Jakubiak Chris, Muglia Mike, Haines Sara, Seim Harvey. c // Marine Technology Society Journal. 2010. 44, 6.

Rohr JJ, Itsweire EC, Helland KN, Van Atta CW. Growth and decay of turbulence in a stably stratified shear flow // Journal of Fluid Mechanics. 1988. 195. 77–111.

Rudzin JE, Shay Lynn K, Jaimes B, Brewster JK. Upper ocean observations in eastern C aribbean S ea reveal barrier layer within a warm core eddy // Journal of Geophysical Research: Oceans. 2017. 122, 2. 1057–1071.

Rudzin Johna E, Shay Lynn K, Johns William E. The influence of the barrier layer on SST response during tropical cyclone wind forcing using idealized experiments // Journal of Physical Oceanography. 2018. 48, 7. 1471–1478.

Sanford T. Spatial structure of thermocline and abyssal internal waves in the Sargasso Sea // Deep Sea Res. II. 2013. 85. 195–209.

Savelyev I, Thomas LN, Smith GB, Wang Q, Shearman RK, Haack T, Christman AJ, Blomquist B, Sletten M, Miller WD, others . Aerial observations of symmetric instability at the north wall of the Gulf Stream // Geophysical Research Letters. 2018a. 45, 1. 236–244.

Savelyev Ivan, Miller William David, Sletten Mark, Smith Geoffrey B, Savidge Dana K, Frick Glendon, Menk Steven, Moore Trent, De Paolo Tony, Terrill Eric J, others . Airborne remote sensing of the upper ocean turbulence during CASPER-East // Remote Sensing. 2018b. 10, 8. 1224.

Schade Lars R, Emanuel Kerry A. The ocean's effect on the intensity of tropical cyclones: Results from a simple coupled atmosphere–ocean model // Journal of the Atmospheric Sciences. 1999. 56, 4. 642–651.

Seim Harvey E, Gregg Michael C. Detailed observations of a naturally occurring shear instability // Journal of Geophysical Research: Oceans. 1994. 99, C5. 10049–10073.

Seroka Greg, Fredj Erick, Kohut Josh, Dunk Rich, Miles Travis, Glenn Scott. Sea breeze sensitivity to coastal upwelling and synoptic flow using Lagrangian methods // Journal of Geophysical Research: Atmospheres. 2018. 123, 17. 9443–9461.

Seroka Greg, Miles Travis, Xu Yi, Kohut Josh, Schofield Oscar, Glenn Scott. Hurricane Irene Sensitivity to Stratified Coastal Ocean Cooling // Monthly Weather Review. 2016. 144, 9. 3507–3530.

Shaun-Johnston T M, Rudnick Daniel L. Observations of the transition layer // J. Phys. Oceanogr. 2009. 39, 3. 780–797.

Shay Lynn K, Goni Gustavo J, Black Peter G. Effects of a warm oceanic feature on Hurricane Opal // Monthly Weather Review. 2000. 128, 5. 1366–1383.

Shearman R Kipp. Observations of near-inertial current variability on the New England shelf // Journal of Geophysical Research: Oceans. 2005a. 110, C2.

Shearman R. Kipp. Observations of near-inertial current variability on the New England shelf // Journal of Geophysical Research C: Oceans. 2005b. 110, 2. 1–16.

Shrira Victor I., Forget Philippe. On the Nature of Near-Inertial Oscillations in the Uppermost Part of the Ocean and a Possible Route toward HF Radar Probing of Stratification // Journal of Physical Oceanography. 2015. 45, 10. 2660–2678.

Shroyer EL, Benoit-Bird KJ, Nash JD, Moum JN. Stratification and mixing regimes in biological thin layers over the Mid-Atlantic Bight // Limnology and Oceanography. 2014. 59, 4. 1349–1363.

Skyllingstad E., Samelson R. Baroclinic frontal instabilities and turbulent mixing in the surface boundary layer. Part I: unforced simulations. // J. Phys. Oceanogr. 2012. 42. 1701–1715.

Skyllingstad Eric D., Duncombe Jenessa, Samelson Roger M. Baroclinic Frontal Instabilities and Turbulent Mixing in the Surface Boundary Layer. Part II: Forced Simulations // Journal of Physical Oceanography. 2017a. 47, 10. 2429–2454.

Skyllingstad Eric D, Duncombe Jenessa, Samelson Roger M. Baroclinic frontal instabilities and turbulent mixing in the surface boundary layer. Part II: Forced simulations // Journal of Physical Oceanography. 2017b. 47, 10. 2429–2454.

Smith Adam B, Katz Richard W. US billion-dollar weather and climate disasters: data sources, trends, accuracy and biases // Natural hazards. 2013. 67, 2. 387–410.

Smith Jerome A. Observed growth of Langmuir circulation // Journal of Geophysical Research: Oceans. 1992. 97, C4. 5651–5664.

Smith K. M., Hamlington P. E., Fox-Kemper B. Effects of submesoscale turbulence on ocean tracers // J. Geophys. Res. 2016. 121. 908–933.

Smits Alexander J, McKeon Beverley J, Marusic Ivan. High–Reynolds number wall turbulence // Annual Review of Fluid Mechanics. 2011. 43.

Smyth WD, Nash JD, Moum JN. Self-organized criticality in geophysical turbulence // Scientific reports. 2019. 9, 1. 1–8.

Smyth William D. Secondary Kelvin–Helmholtz instability in weakly stratified shear flow // Journal of Fluid Mechanics. 2003. 497. 67–98.

Smyth William D, Moum James N. Length scales of turbulence in stably stratified mixing layers // Physics of Fluids. 2000. 12, 6. 1327–1342.

Smyth William D, Moum James N. Ocean mixing by Kelvin-Helmholtz instability // Oceanography. 2012. 25, 2. 140–149.

Sous Damien, Sommeria Joël, Boyer D. Friction law and turbulent properties in a laboratory Ekman boundary layer // Physics of Fluids. 2013. 25, 4. 046602.

Stevenson James W, Niiler Pearn P. Upper ocean heat budget during the Hawaii-to-Tahiti shuttle experiment // Journal of physical oceanography. 1983. 13, 10. 1894–1907.

Sullivan Peter P, McWilliams James C. Dynamics of winds and currents coupled to surface waves // Annual Review of Fluid Mechanics. 2010. 42.

Sullivan Peter P, McWilliams James C. Frontogenesis and frontal arrest of a dense filament in the oceanic surface boundary layer // Journal of Fluid Mechanics. 2018. 837. 341–380.

Sullivan Peter P, McWilliams James C. Langmuir turbulence and filament frontogenesis in the oceanic surface boundary layer // Journal of Fluid Mechanics. 2019. 879. 512–553.

Sullivan Peter P, Romero Leonel, McWilliams James C, Melville W Kendall. Transient evolution of Langmuir turbulence in ocean boundary layers driven by hurricane winds and waves // Journal of physical oceanography. 2012. 42, 11. 1959–1980.

Sundermeyer Miles A, Skyllingstad Eric, Ledwell James R, Concannon Brian, Terray Eugene A, Birch Daniel, Pierce Stephen D, Cervantes Brandy. Observations and numerical simulations of large-eddy circulation in the ocean surface mixed layer // Geophysical Research Letters. 2014. 41, 21. 7584–7590.

Tatro Peter R, Mollo-Christensen EL. Experiments on Ekman layer instability // Journal of Fluid Mechanics. 1967. 28, 3. 531–543.

Taylor JR. Turbulent mixing, restratification, and phytoplankton growth at a submesoscale eddy // Geophys. Res. Lett. 2016.

Taylor John R. Numerical simulations of the stratified oceanic bottom boundary layer. 2008.

Taylor John R., Ferrari Raffaele. Buoyancy and Wind-Driven Convection at Mixed Layer Density Fronts // Journal of Physical Oceanography. 2010. 40, 6. 1222–1242.

Taylor John R, Ferrari Raffaele. Ocean fronts trigger high latitude phytoplankton blooms // Geophysical Research Letters. 2011. 38, 23.

Tejada-Martinez AE, Grosch CE. Langmuir turbulence in shallow water. Part 2. Large-eddy simulation // Journal of Fluid Mechanics. 2007. 576. 63–108.

Testor Pierre, Young Brad de, Rudnick Daniel L., Glenn Scott, Hayes Daniel, Lee Craig M., Pattiaratchi Charitha, Hill Katherine, Heslop Emma, Turpin Victor, Alenius Pekka, Barrera Carlos, Barth John A., Beaird Nicholas, Bécu Guislain, Bosse Anthony, Bourrin François, Brearley J. Alexander, Chao Yi, Chen Sue, Chiggiato Jacopo, Coppola Laurent, Crout Richard, Cummings James, Curry Beth, Curry Ruth, Davis Richard, Desai Kruti, DiMarco Steve, Edwards Catherine, Fielding Sophie, Fer Ilker, Frajka-Williams Eleanor, Gildor Hezi, Goni Gustavo, Gutierrez Dimitri, Haugan Peter, Hebert David, Heiderich Joleen, Henson Stephanie, Heywood Karen, Hogan Patrick, Houpert Loïc, Huh Sik, E. Inall Mark, Ishii Masso, Ito Shin-ichi, Itoh Sachihiko, Jan Sen, Kaiser Jan, Karstensen Johannes, Kirkpatrick Barbara, Klymak Jody, Kohut Josh, Krahmann Gerd, Krug Marjolaine, McClatchie Sam, Marin Frédéric, Mauri Elena, Mehra Avichal, P. Meredith Michael, Meunier Thomas, Miles Travis, Morell Julio M., Mortier Laurent, Nicholson Sarah, O'Callaghan Joanne, O'Conchubhair Diarmuid, Oke Peter, Pallàs-Sanz Enric, Palmer Matthew, Park JongJin, Perivoliotis Leonidas, Poulain Pierre-Marie, Perry Ruth, Queste Bastien, Rainville Luc, Rehm Eric, Roughan Moninya, Rome Nicholas, Ross Tetjana, Ruiz Simon, Saba Grace, Schaeffer Amandine, Schönau Martha, Schroeder Katrin, Shimizu Yugo, Sloyan Bernadette M., Smeed David, Snowden Derrick, Song Yumi, Swart Sebastian, Tenreiro Miguel, Thompson Andrew, Tintore Joaquin, Todd Robert E., Toro Cesar, Venables Hugh, Wagawa Taku, Waterman Stephanie, Watlington Roy A., Wilson Doug. Ocean-Gliders: A Component of the Integrated GOOS // Frontiers in Marine Science. 2019. 6. 422.

Thorpe SA. The axial coherence of Kelvin–Helmholtz billows // Quarterly Journal of the Royal Meteorological Society: A journal of the atmospheric sciences, applied

meteorology and physical oceanography. 2002. 128, 583. 1529–1542.

Thorpe SA. Langmuir circulation // Annu. Rev. Fluid Mech. 2004. 36. 55–79.

Thorpe SA, Liu Zhiyu. Marginal instability? // Journal of physical oceanography. 2009. 39, 9. 2373–2381.

Toyoda Takahiro, Fujii Yosuke, Kuragano Tsurane, Kosugi Naohiro, Sasano Daisuke, Kamachi Masafumi, Ishikawa Yoichi, Masuda Shuhei, Sato Kanako, Awaji Toshiyuki, others . Interannual-decadal variability of wintertime mixed layer depths in the North Pacific detected by an ensemble of ocean syntheses // Climate Dynamics. 2017. 49, 3. 891–907.

Trowbridge J. H. A simple description of the deepening and structure of a stably stratified flow driven by a surface stress // Journal of Geophysical Research. 1992. 97, C10. 15529—-15543.

Turner John Stewart. Buoyancy effects in fluids. 1979.

Van Roekel LP, Fox-Kemper B, Sullivan PP, Hamlington PE, Haney SR. The form and orientation of Langmuir cells for misaligned winds and waves // Journal of Geophysical Research: Oceans. 2012. 117, C5.

Venayagamoorthy Subhas K, Koseff Jeffrey R. On the flux Richardson number in stably stratified turbulence // Journal of Fluid Mechanics. 2016. 798.

Wallace Elizabeth J, Looney Lev B, Gong Donglai. Multi-decadal trends and variability in temperature and salinity in the Mid-Atlantic Bight, Georges Bank, and Gulf of Maine // Journal of Marine Research. 2018. 76, 5. 163–215.

Walsh John J, Dieterle Dwight A, Meyers Mark B. A simulation analysis of the fate of phytoplankton within the Mid-Atlantic Bight // Continental Shelf Research. 1988. 8, 5-7. 757–787.

Watkins C., Whitt D. data for Large-aspect-ratio structures in simulated ocean surface boundary layer turbulence under a hurricane. 2020a. accessed June 16, 2020.

Watkins Clifford, Whitt Daniel B. Large-Aspect-Ratio Structures in Simulated Ocean Surface Boundary Layer Turbulence under a Hurricane // Journal of Physical Oceanography. 2020b. 50, 12. 3561 – 3584.

Whitt Daniel B, Lévy Marina, Taylor John Ryan. Submesoscales Enhance Storm-Driven Vertical Mixing of Nutrients: Insights From a Biogeochemical Large Eddy Simulation // Journal of Geophysical Research: Oceans. 2019. 124, 11. 8140–8165.

Whitt Daniel B, Taylor John R. Energetic Submesoscales Maintain Strong Mixed Layer Stratification during an Autumn Storm // Journal of Physical Oceanography. 2017. 47, 10. 2419–2427.

Wijesekera Hemantha W, Dillon Thomas M. Internal waves and mixing in the upper equatorial Pacific Ocean // Journal of Geophysical Research: Oceans. 1991. 96, C4. 7115–7125.

Woods JD. Diurnal and seasonal variation of convection in the wind-mixed layer of the ocean // Quarterly Journal of the Royal Meteorological Society. 1980. 106, 449. 379–394.

Xu Y, Cahill B, Wilkin J, Schofield O. Role of wind in regulating phytoplankton blooms on the Mid-Atlantic Bight // Continental Shelf Research. 2013. 63. S26–S35.

Young George S, Kristovich David AR, Hjelmfelt Mark R, Foster Ralph C. Rolls, streets, waves, and more: A review of quasi-two-dimensional structures in the atmospheric boundary layer // Bulletin of the American Meteorological Society. 2002. 83, 7. 997–1002.

Zervakis Vassilis, Kokkini Zoi, Potiris Emmanuel. Estimating mixed layer depth with the use of a coastal high-frequency radar // Continental Shelf Research. 2017. 149, August. 4–16.

Zhang Fan, Li Ming, Miles Travis. Generation of Near-Inertial Currents on the Mid-Atlantic Bight by Hurricane Arthur (2014) // Journal of Geophysical Research: Oceans. 2018a. 2014. 3100–3116.

Zhang ShuWen W., Xie LingLing L., Zhao Hui, Hou YiJun J. Tropical storm-forced near-inertial energy dissipation in the southeast continental shelf region of Hainan Island // Science China Earth Sciences. 2014. 57, 8. 1879–1884.

Zhang Wei, Villarini Gabriele, Vecchi Gabriel A, Smith James A. Urbanization exacerbated the rainfall and flooding caused by hurricane Harvey in Houston // Nature. 2018b. 563, 7731. 384–388.

de Boyer Montégut Clément, Madec Gurvan, Fischer Albert S., Lazar Alban, Iudicone Daniele. Mixed layer depth over the global ocean: An examination of profile data and a profile-based climatology // Journal of Geophysical Research C: Oceans. 2004. 109, 12. 1–20.